Title

Endoplasmic reticulum remodeling during budding yeast meiosis

Permalink

https://escholarship.org/uc/item/6cz1152t

Author

Otto, George

Publication Date

2020

Endoplasmic reticulum remodeling during budding yeast meiosis

By

George M Otto

A dissertation submitted in partial satisfaction of the

requirements for the degree of

Doctor of Philosophy

in

Molecular and Cell Biology

in the

Graduate Division

of the

University of California, Berkeley

Committee in charge:

Professor Gloria Brar, Chair
Professor Andrew Dillin
Professor Roberto Zoncu
Professor James Olzmann

Fall 2020

Abstract

Endoplasmic reticulum remodeling during budding yeast meiosis

by

George Maxwell Otto

Doctor of Philosophy in Molecular and Cell Biology

University of California, Berkeley

Professor Gloria Brar, Chair

The endoplasmic reticulum (ER) is a membrane-bound organelle that carries out a range of essential cellular functions, from protein trafficking to lipid homeostasis to inter-organelle signaling. These functions rely on the maintenance of an intricate membrane architecture that is rapidly remodeled in response to changes in cellular demand, such as the presence of external stressors or the onset of cell differentiation. Work in the last fifteen years has greatly expanded our knowledge of how ER membranes are shaped in unperturbed cells, but mechanisms controlling dynamic ER remodeling under changing conditions, especially during cell differentiation, are not well understood. Here, we use budding yeast meiosis as a model system to study gene regulation and ER remodeling in a developmental context.

In chapter 2, we identify a series of developmentally regulated changes in ER morphology and composition that simultaneously control organelle inheritance and degradation. During meiosis, the cortical ER undergoes reticulon-dependent fragmentation before dramatically collapsing away from the plasma membrane (PM). While the vast majority of ER collapses during this process, a subset of ER fragments is retained at the cell cortex via ER-PM tethering proteins and thereby excluded from gametes. Cortically retained ER is degraded late in spore packaging, while collapsed ER is subject to selective autophagy, indicating that multiple parallel pathways exist to eliminate unwanted ER during meiosis. These findings raise new questions about the role of ER remodeling events in developmental quality control, which we discuss in chapter 3.

In chapter 4, we leverage a genomics approach to address a fundamental question in gene regulation: why does mRNA expression often fail to predict protein abundance? Using global parallel measurements of mRNA abundance, translation, and protein levels over the course of meiosis, we identify genes with poor mRNA:protein correlation over time. We show that hundreds of these genes are regulated by transcript isoform toggling, in which a poorly translated extended transcript isoform prevents expression of an efficiently translated canonical isoform. Thus, apparent transcriptional upregulation can lead to protein downregulation in an isoform-dependent manner, with important implications for the interpretation of genomics datasets.

For Dad
(returning the favor)
LYS.

Table of Contents

Acknowledgements

It is impossible to adequately thank all of the people who have helped me grow as a scientist and as a human in the last seven years. This is an attempt.

Thank you to Gloria for your incredibly generous and supportive mentorship. From our first meeting you have always put me at ease and provided insightful and genuine advice on life and science alike.

Thank you to everyone in the Brar and Ünal labs, past and present, for making lab life fun and welcoming. A massive thank you to Amy, my lab sibling, for your friendship over the years. I could not have picked a better person to spend my PhD bumming around the Bay Area, exploring nature and occasionally doing science with. Thank you to Tina for your warm, steadfast, and generous friendship. You are the only person I can turn to for a deep conversation that covers the latest soccer drama and existential life advice in a matter of minutes. Thank you to EPow for countless trips to Cheeseboard and Loose Juice (or whatever it's called) to unwind. You were with me through by far the most difficult stretch of lab work in my PhD and I couldn't have gotten through it without you. Thank you to Vicki for being an amazing lab buddy, a spark of spontaneity and humor, and for expanding my mind with crosswords and philosophical discussions. Thank you to Tia for your positivity and enthusiasm, and generally being a joy to work with. Thank you to Grant and Ina for being two of the funniest people I know – it has unexpectedly brightened my day on countless occasions. Thanks to Jay for stanning Wisconsin beers and always being down for a casual science chat. Thank you to Jing for always being enthusiastic, supportive and engaged in my science even when I wasn't. Thank you to Christiane for being such a warm presence in lab and for being an incredibly reliable and organized lab manager. I owe huge thanks to Elçin for being an insightful, caring, and enthusiastic mentor. Thanks to Chris and Leon for serving as kid-adult intermediaries and for generally being tons of fun to be around. Thank you to Alex (and the rest of the staff that keeps our building running) for showing up at the wee hours to chat about soccer and remind me to go home.

Thank you to my thesis committee, James, Roberto and Andy, for your helpful advice and stimulating discussion at every step of my PhD.

Thank you to my MCB 2014 classmates, who have provided so much joy and support from day one. Thank you to Rob and Fernando for being the realest. Thank you to Dom and Caitlin for heart-to-hearts, Feefs, and for making the best comfort food. Thank you to Lydia for teaching me everything I know about backpacking. Thanks to Franzi for being my first and only broton (sistron?), for taking me in in my time of need, and for your friendship. Thanks to Dan for low-quality song parodies and solid fashion advice. Thank you to Tim for your masterful preparation of all types of poultry. Thanks to Eva for your positivity. Thank you to Janice and Rusty for all your stories and for generally being tons of fun. Thank you to Rose and Rory for your shenanigans and for knowing the best brunch places to go when your house has been condemned.

I am incredibly grateful to have been a part of the MCB graduate community. Thank you to all of the unique and brilliant people I have crossed paths with as a result, of whom there are too many to name. I want to say thanks to Davis for being an incredibly funny kind, and insightful friend. You have helped me understand myself, the world, and mid-tier fast food cuisine. Thanks also to Brian for being a uniquely funny and irreverent, yet caring, passionate and inclusive human. Thank you to all of my MCBallers and Soctopus teammates – soccer has been fundamental to finding balance in my life and it would not be possible without you.

Thank you to Cody and Laura for being among the best people I know and an essential lifeline to the world outside of science.

Thank you to Samba and Phoebe for being so giving and accepting of affection, and for reminding me that it is possible to go through life completely oblivious to the success or failure of a given experiment and still be perfectly happy.

Thank you to Shally for your unwavering love and support through the best and worst of life. I am so incredibly grateful for your companionship, and for the big and little things you do that fill the lives of those around you with spontaneity, humor, warmth and joy.

Thank you to my family for providing love, support and perspective throughout this process. Thank you to my mom for always being there for me, for being able to simplify difficult situations to help me see what really matters, for teaching me to be a critical thinker, and for showing me the value of infectious, hysterical (unhinged?) laughter.

Thank you to Liz for being inventive, curious, and uniquely yourself no matter what. Thank you to Henry for your perseverance in difficult situations and for seeing the best in people you love.

Thank you to Braedy for being such a steady, caring, insightful, and fun presence in my life. Thank you for being a loving and selfless partner to my dad, and for bringing him so much happiness.

Thank you most of all to my dad. Thank you for teaching me to find and cherish the idiosyncrasies in people around me. Thank you for teaching me to value the good things in my life, regardless of the path that lead there. Thank you for shaping my sense of humor, and for teaching me to be overly self-congratulatory when I think I’m being funny. Thank you for fostering my love of nature and encouraging me to explore the world. Thank you for taking my random ideas and goals and wanting them so badly for me that I feel obligated to make them happen. Thank you for being my biggest cheerleader, for celebrating my successes more than I do, and for lifting me up when I feel uninspired. Thank you for taking so much pride in being my dad. I could not have asked for a better one.

Chapter 1: Structure and function of the endoplasmic reticulum

The endoplasmic reticulum (ER) is a membrane-bound organelle that serves as a cellular hub for various essential processes, including protein synthesis, folding and trafficking, lipid biogenesis, and inter-organelle communication. ER membrane shape is intimately linked to organelle function, and cells maintain morphologically specialized subdomains to support specific processes. Accordingly, cells remodel their ER in response to environmental changes, including external stress and cell differentiation. Here, I discuss essential features of ER biology, the relationship between ER structure and function, and how the ER is remodeled to support changing cellular needs.

1.1 Protein synthesis at the endoplasmic reticulum

The compartmentalization of cellular functions into organelles with distinct chemical environments allows cells to perform a diverse range of biochemical processes that could not coexist efficiently in a single cellular milieu. Compartmentalization also comes with unique challenges, namely the translocation of proteins across a hydrophobic membrane and the precise targeting of proteins to their site of function. The ER plays a central role in these processes, as proteins destined for the ER itself, as well as the plasma membrane, lipid droplets, peroxisomes, inner nuclear membrane, endomembrane system, and secreted proteins are all synthesized at the ER. In total, the ER is the site of synthesis for an estimated one-third of all eukaryotic proteins (Aviram and Schuldiner, 2017).

The most well-studied ER targeting mechanism involves the signal recognition particle (SRP), a large ribonucleoprotein complex that binds to ribosomes and recognizes hydrophobic targeting motifs on nascent secretory proteins. SRP then targets the translating ribosome to the ER through its interaction with the ER-localized SRP receptor (SR) (Keenan et al., 1998). The SR in turn associates with the Sec61 translocon, a heterotrimeric complex comprised of Sec61, Sbh1 and Sss1 (Sec61β/γ in mammals) (Gilmore et al., 1982b, 1982a). The translocon is a transmembrane channel that allows passage of the nascent peptide through the ER membrane. Hydrophilic protein segments pass freely through the aqueous pore of the translocon, whereas hydrophobic transmembrane segments diffuse into the membrane through a lateral gate (Gogala et al., 2014; Rapoport, 2007).

The SRP-dependent pathway efficiently targets proteins with a hydrophobic targeting sequence at or near the N-terminus. A second mechanism is responsible for targeting tail-anchored proteins, which have a single transmembrane domain at their C-terminus. This mechanism is termed the GET pathway, for guided entry of tail-anchored (TA) proteins (Mateja and Keenan, 2018; Schuldiner et al., 2008). In this pathway, Get3 binds to the hydrophobic stretch of amino acids that will form the transmembrane domain of the TA protein (Mateja et al., 2015) and delivers it to the ER, where Get1/2 heterotetramers mediate protein insertion into the membrane (McDowell et al., 2020; Schuldiner et al., 2008).

More recently, a third parallel ER-targeting mechanism called the SRP-independent (SND) pathway has been identified. The SND pathway has broad substrate specificity in that it shares targets with – and can buffer against defects in – both the SRP-dependent and GET pathways (Aviram et al., 2016). A set of conserved cytosolic and ER-localized proteins have been identified as essential components of the SND pathway, but the molecular mechanisms driving this targeting process are yet to be defined. Together, the existence and evolutionary conservation of these parallel pathways for ER protein targeting underscores the central role of this process in eukaryotic cell biology.

1.2 Endoplasmic reticulum morphology

The endoplasmic reticulum is a single, continuous membrane system that stretches from the nuclear envelope to the cell periphery and adopts a striking diversity of morphologies within a single cell. One such structure is ER sheets, which form large expanses of flat membrane that stack on top of one another in a manner that has been likened to the tiers of a parking garage (Shibata et al., 2006). Alternatively, the ER membrane can take on tubular structures, which have high membrane curvature and join together with other tubules to form a web-like network (reviewed in Westrate et al., 2015). ER tubules are highly dynamic, constantly growing, fusing with one another, and forming contacts with other cellular structures. The conserved and intricate nature of ER structure is suggestive of functional importance. Early electron micrographs showing ER sheets covered with ribosomes suggested that these structures are specialized for protein synthesis, perhaps because ribosomes could associate more stably with expansive sheet structures than narrower tubules. More recently, advances in microscopy techniques and the discovery of proteins responsible for generating ER shape has enabled researchers to directly interrogate the relationship between ER structure and function.

The first set of proteins identified to shape ER membranes, the reticulons, were discovered biochemically as the covalent target of drugs that inhibit *in vitro* tubular ER network formation (Voeltz et al., 2006). These proteins contain an atypical hairpin-shaped membrane domain (reticulon homology domain; RHD) that does not fully traverse the ER membrane and therefore takes up more space in the cytosolic leaflet, leading to positive membrane curvature and tubule formation (Sparkes et al., 2010; Tolley et al., 2010; Voeltz et al., 2006). Budding yeast encode two reticulon proteins, Rtn1 and Rtn2, and a related protein Yop1, that together are required for tubular network formation *in vivo* (Voeltz et al., 2006). Purified reticulons and Yop1 form tubular membrane structures when incorporated into proteoliposomes, indicating that any of these proteins alone is sufficient to generate the stable membrane curvature required to form the tubular ER network (Shibata et al., 2008).

Climp63 is a morphological determinant of ER sheets that was initially identified by virtue of its elevated expression in cell types with high secretory load, which have abundant ER sheets (Shibata et al., 2010). Overexpression of Climp63 increases ER sheet abundance, whereas depletion decreases the luminal width of ER sheets without eliminating them completely, indicating that Climp63 acts as a luminal membrane spacer within ER sheets. Enrichment of Climp63 in ER sheets relies on its luminal coiled coil domain, but its mechanism of action is otherwise mysterious (Klopfenstein et al., 2001). Budding yeast do not have a Climp63 homologue, and no functional equivalent has been identified, raising the question of how sheet structures are maintained in this and other organisms lacking Climp63. There is some evidence that the presence of polysomes engaged in translation on ER membranes contributes to sheet morphogenesis in mammalian cells, and perhaps this is sufficient to maintain these structures in yeast (Shibata et al., 2010). In budding yeast, expanding ER membrane surface area through the upregulation of phospholipid synthesis enzymes results in an apparent increase in the abundance of sheets relative to tubules, suggesting that sheets may be a default morphology in this context (Schuck et al., 2009; Shibata et al., 2010). Balance is restored by overexpression of reticulons, highlighting the dichotomy between sheets and tubules and the role of reticulon levels in determining tubular ER structure.

Maintaining the ER network requires the ability not only to form tubules, but to join them together to form three-way junctions. The process of tubule fusion is carried out by the dynamin-like GTPases atlastin (in metazoans) and Sey1 (in yeast). These proteins are not closely related by sequence homology but have the same general domain structure and function. The role of Atlastin/Sey1 in structuring the ER was first described in mammalian cells after it was identified as a reticulon-interacting protein that localizes to the tubular ER (Hu et al., 2009b). Simultaneously, other researchers reasoned that GTP – and presumably an ER-localized GTPase – is required for *in vitro* ER reconstitution, leading them to identify atlastin as a regulator of ER morphogenesis in Drosophila (Orso et al., 2009). Atlastin knockdown or expression of a dominant negative GTPase null atlastin mutant results in long, unbranched ER tubules or fragmented tubular ER, depending on the context and atlastin isoform (Espadas et al., 2019; Hu et al., 2009b; Orso et al., 2009; Wang et al., 2016). The reasons for the context- and isoform-specificity that give rise to different ER morphology outcomes are unclear, but both outcomes are consistent with the role of atlastins in promoting membrane fusion.

Both atlastin and Sey1 promote the fusion of proteoliposomes in a GTPase-dependent manner *in vitro* (Anwar et al., 2012; Orso et al., 2009). Indeed, incorporation of Sey1 and Yop1 together into proteoliposomes in the presence of GTP is sufficient to generate an *in vitro* tubular ER network (Powers et al., 2017). Sey1-dependent ER fusion was also elegantly demonstrated *in vivo*, as yeast lacking Sey1 show a severe delay in ER fusion between parent cells following mating (Anwar et al., 2012). Subsequent structural work has shed light on the molecular rearrangements that drive atlastin/Sey1-mediated ER membrane fusion. GDP-bound atlastin molecules homodimerize in trans via a cytosolic “middle” domain. GTP binding and hydrolysis then drive conformational changes that bring the two membranes into close apposition, thus promoting fusion (Bian et al., 2011; Byrnes and Sondermann, 2011; Byrnes et al., 2013; Moss et al., 2011; Pendin et al., 2011). Addition of a long linker sequence between the dimerization and membrane domains does not affect protein conformational changes but prevents fusion, further suggesting that the role of these molecular rearrangements is to bring membranes into close proximity (Pendin et al., 2011).

In order to maintain ER network structure, membrane fusion must be counterbalanced by fission. While a range of essential membrane fission processes have been mechanistically characterized in other contexts, including cytokinesis, endocytosis, and mitochondrial fission, the regulation of ER tubule fission is not well understood. A growing body of evidence supports a role for reticulons in this process. Reticulon overexpression causes membrane fragmentation in mammalian cell culture and fruit fly models (Espadas et al., 2019; Tolley et al., 2008; Wang et al., 2016). ER networks reconstituted from purified components or Xenopus egg extract undergo fragmentation upon inhibition of Sey1/Atlastin, suggesting that reticulon-containing tubules have an intrinsic propensity to fragment that is counteracted by membrane fusion (Powers et al., 2017; Wang et al., 2016). Consistent with this model, atlastin depletion causes ER fragmentation that is rescued by co-depletion of reticulon in Drosophila (Espadas et al., 2019). Similarly, fragmented ER resulting from reticulon overexpression is rescued by co-overexpression of atlastin in mammalian cells (Wang et al., 2016).

It is still unclear whether reticulons play an active mechanistic role in tubule scission, or if high membrane curvature simply increases the likelihood of scission without the need for any additional determinative action. *In vitro* experiments using reticulon-containing nanotubules suggest that tubule scission is a stochastic event, with reticulon concentration and the presence of pulling forces both contributing to the likelihood of a scission event (Espadas et al., 2019). The role of reticulon concentration in membrane fission is well supported across multiple *in vivo* models, though these studies all used artificially high global reticulon expression to observe membrane fragmentation.

Reticulon-dependent membrane fragmentation has been observed at physiological expression levels in the context of ER autophagy (ERphagy). Several ERphagy receptors (proteins that recruit autophagosomes to the ER) contain reticulon homology domains and, upon induction of autophagy, assemble into domains of high local reticulon concentration favorable for membrane fragmentation. These domains are topologically separated from the rest of the ER and free to be engulfed by the autophagosome (Grumati et al., 2017; Jiang et al., 2020; Mochida et al., 2020). In the case of budding yeast ERphagy receptor Atg40, local concentration is achieved through multivalent interactions with itself and Atg8, which is abundant on autophagosome membranes (Mochida et al., 2020). The reticulon homology domain is not required for assembly but is essential for membrane fragmentation and autophagy, underscoring the importance of membrane curvature in promoting scission events. Similarly, mammalian ERphagy receptor Rtn3 oligomerizes during starvation to promote membrane fragmentation (Grumati et al., 2017). Artificial oligomerization in the absence of autophagy cues is sufficient to promote fragmentation, indicating that local reticulon concentration alone drives this process. In the case of another mammalian ERphagy receptor, FAM134B, phosphorylation within the RHD of FAM134B enhances oligomerization and subsequent fragmentation, demonstrating the potential for external regulatory cues to drive context-specific membrane scission (Bhaskara et al., 2019; Jiang et al., 2020).

Lunapark (Lnp) proteins represent another conserved protein family involved in regulating ER network formation. This family was initially identified in a visual screen for yeast mutants with abnormal cortical ER morphology (Chen et al., 2012). Yeast and human Lnp proteins localize to three-way tubular junctions, and newly formed junctions are short-lived when Lnp1 is not present (Chen et al., 2012, 2015). In Xenopus egg extract, inhibiting Lnp function using blocking antibodies or treating with a dominant negative Lnp fragment dramatically reduces the abundance of three-way ER junctions (Wang et al., 2016). Together, these data suggest a role for Lnp1 in stabilizing tubule junctions. In budding yeast, Lnp1 demonstrates functional antagonism with Sey1-mediated membrane fusion. ER morphology defects of *lnp1Δ* cells are reversed in a *sey1Δ lnp1Δ* double mutant. Likewise, growth defects in cells lacking both Lnp1 and Rtn1 are rescued by the additional deletion of the gene encoding Sey1. In mammalian cells, Lnp overexpression leads to an increase in apparent sheet-like structures, though it is possible that these are actually densely reticulated structures that cannot be resolved by diffraction-limited microscopy (Nixon-Abell et al., 2016; Wang et al., 2016). Additional overexpression of atlastin restores normal ER morphology, consistent with functional antagonism between these proteins in this context. It is difficult to reconcile the apparently opposing functions of Lnp and Sey1/atlastin with the clear importance of Lnp in maintaining three-way tubule junctions, which are generated by Sey1/atlastin-mediated fusion. Further characterization of Lnp proteins, especially their structure and mechanism of action with respect to Sey1/atlastin, will be important for our understanding of how this family contributes to ER morphology.

1.3 The relationship between ER structure and function

Cells invest considerable energy in maintaining ER intricate structures. The basic units of ER structure, namely sheets and tubules, are present across all eukaryotes, as are the proteins that generate these structures (with the noted exception of Climp63). At the same time, ER structure varies dramatically between different cell types. All of this together suggests that ER structure and function are intimately linked, and that it is imperative for cells to mold and adapt ER morphology to suit their specific needs.

ER functions take place in structurally specialized subdomains. Protein synthesis, folding and trafficking occur on membrane sheets, whereas functions like lipid synthesis, calcium transfer, and inter-organelle signaling are enriched on tubules (Shibata et al., 2006; Westrate et al., 2015). The precise reasons for this are difficult to demonstrate experimentally, but one logical explanation is that sheets, by virtue of their lower surface area-to-luminal volume ratio, are well equipped to accommodate luminal processes. Conversely, tubules have a high surface area-to-volume and are therefore suited to membrane-dependent processes. For example, protein folding requires many luminal chaperones and glycosylation enzymes, so sheet structures can accommodate this process most efficiently. On the other hand, substrates and enzymes for lipid metabolism occur in the membrane and therefore functionally concentrate in ER tubules. The geometry of the tubular network is also an efficient means for the ER to reach every corner of the cell while taking up minimal physical space so as not to crowd out other cellular structures. It therefore makes sense that the extensive inter-organelle contacts formed by the ER would happen predominantly through ER tubules.

Consistent with the close relationship between ER structure and function, specialized cell types display dramatically different ER structures depending on cellular need. Cells tasked with a high volume of protein secretion, such as those located in the pancreas or salivary glands, have massively expanded, ribosome-studded ER sheets to facilitate protein synthesis (Jamieson and Palade, 1967b, 1967a; Schwarz and Blower, 2016; Terasaki et al., 2013). Muscle cells form incredibly intricate ER structures with extensive plasma membrane contacts to support the extensive calcium signaling required for muscle contraction (Davidowitz et al., 1975; Ogata and Yamasaki, 1997; Shibata et al., 2006). Cell-specific ER morphology is perhaps most dramatic in neurons, where individual ER tubules have been observed to traverse entire axons to interface with synapses (Maco et al., 2013).

Perhaps because of the need to organize such intricate structures over long distances, neurons are particularly susceptible to defects in ER morphogenesis. Mutations in ER-shaping genes are associated with a range of neuropathies (Renvoisé and Blackstone, 2010). Notably, patients with hereditary spastic paraplegia, a disease affecting motor neurons in the lower extremities, have mutations that disrupt atlastin-mediated membrane fusion (Bian et al., 2011; Byrnes and Sondermann, 2011). A mutation in FAM134B that causes constitutive oligomerization and membrane fragmentation is associated with a type of hereditary sensory and autonomic neuropathy (Jiang et al., 2020). In mice, Rtn3 overexpression leads to the development of dystrophic neurons with pathology reminiscent of Alzheimer's disease (Hu et al., 2007; Shi et al., 2017). In general, the cellular processes linking disrupted ER structure and neuropathology require further mechanistic exploration, but these examples highlight the importance of ER morphogenesis in specialized cell types.

The existence of specialized ER morphologies in differentiated cells implies that the ER is dynamically remodeled as a part of cell differentiation. However, few model systems exist for studying developmental ER remodeling in real time. ER stress has proven a more tractable model for observing dynamic changes in ER morphology. For example, protein folding stress in yeast causes a massive expansion of ER membranes driven by the transcriptional upregulation of lipid synthesis enzymes (Bircham et al., 2020; Schuck et al., 2009). In many model organisms, stress-induced ER expansion is accompanied by selective autophagic degradation of ER fragments (Fumagalli et al., 2016; Loi et al., 2019; Schuck et al., 2014; Zhang et al., 2020). In general, whether these pathways also mediate developmental ER remodeling are not well established. One exception is in B cell differentiation into plasma cells, which secrete massive amounts of immunoglobulin and, accordingly, display massively expanded ER sheets (Wiest et al., 1990). This differentiation process also activates the IRE1/XBP1 branch of the unfolded protein response (UPR; see "ER quality control" below). It was originally thought that the high burden of protein secretion caused intrinsically high levels of misfolded proteins and consequently high basal UPR activation. However, proteomics analysis over a timecourse of differentiation suggested that UPR transcriptional targets like ER chaperones were highly expressed even before cells started secreting immunoglobulin, suggesting that developmental UPR activation increases protein folding capacity in anticipation of specialized cell function (Van Anken et al., 2003). Moreover, differentiating cells that don't produce secreted immunoglobulin still expressed XBP1, indicating that UPR activation depends on developmental progression but not on protein secretion burden (Hu et al., 2009a). Preemptive UPR activation to maintain the cell's secretion capacity seems a more tenable solution than relying on constitutive protein folding stress to achieve this outcome. This exemplifies the ways in which developmental and stress-induced activation of the same pathway may differ, and highlights the importance of identifying and characterizing the contexts in which stress-induced pathways naturally occur.

The ER network is also remodeled during cell division. In Xenopus egg extracts and C. elegans embryos, the largely tubular interphase ER converts to sheets and/or clustered tubules during mitosis (Audhya et al., 2007; Wang et al., 2013). Inhibition of Lnp in interphase extracts causes a mitosis-like expansion of ER sheets. Lnp is phosphorylated specifically in mitosis, leading to a model in which inhibitory phosphorylation of Lnp regulates this cell cycle-dependent switch in ER morphology (Wang et al., 2016). During meiosis in budding yeast, the cortical ER appears to detach from the plasma membrane and takes on a “collapsed” morphology, though the mechanisms underlying this process have not been identified (Suda et al., 2007). In each of these cases, the role of morphological ER remodeling in organelle function and organismal health require further investigation.

1.4 Tethering and communication between the ER and mitochondria

Membrane lipid composition is crucial for defining the structure and function of organelles and the plasma membrane, but most membranes do not contain the full set of lipid synthesis machinery necessary to establish and maintain membrane identity. In many cases, specific lipids are synthesized in the ER and directly transferred to other membranes. A crucial feature of the ER is its ability to interface with diverse cellular structures at membrane contact sites (MCSs) for the purpose of lipid exchange, ion transfer and organelle fission (Wu et. al. 2018). Early electron tomography and biochemical fractionation experiments suggested the existence of ER MCSs, and recent advances in live cell imaging techniques have greatly enhanced our ability to identify and characterize the diverse array of organelle contacts within cells (Copeland and Dalton, 1959; Friedman et al., 2011; Guo et al., 2018; Vance, 1990).

The ER forms extensive contacts with mitochondria. In budding yeast, ER-mitochondria interaction is mediated in part by the ER-mitochondria encounter structure (ERMES) complex, which contains mitochondrial proteins Mdm10 and Mdm34, the ER protein Mmm1, the cytosolic protein Mdm12, and the regulatory subunit Gem1 (Kornmann et al., 2009, 2011). Phospholipid homeostasis is disrupted in ERMES mutants, and three ERMES subunits contain a synaptotagmin-like mitochondrial lipid-binding protein (SMP) domain that binds to phosphatidylcholine, leading some to suggest a potential direct role for ERMES in phospholipid transfer between the ER and mitochondria (AhYoung et al., 2015; Jeong et al., 2017; Kornmann et al., 2009). The growth defects of ERMES mutants are partially rescued by expression of an enzymatically inert artificial tether, indicating that its role as a tether is important irrespective of any other function, and that important processes occurring at ER-mitochonria contact sites depend on proteins that themselves are insufficient to generate membrane tethering (Kornmann et al., 2009).

Another surprising function for ER-mitochondria contact sites in yeast and human cells is in defining sites of mitochondrial division (Friedman et al., 2011). ER tubules wrapping around mitochondria are associated with mitochondrial constriction and subsequent recruitment of mitochondrial fission machinery. ERMES complexes disproportionately colocalize with ER-marked sites of mitochondrial fission (Murley et al., 2013). Remarkably, these contact sites are required for mitochondrial DNA (mtDNA) replication and separation, which is proposed to ensure proper distribution of mtDNA prior to mitochondrial division (Lewis et al., 2016; Murley et al., 2013). Mitochondrial network fragmentation is associated with the pathology of Alzheimer's disease, potentially explaining the link between aberrant ER tubule structures and the Alzheimer's-like pathology caused by Rtn3 overexpression (Hu et al., 2007; Shi et al., 2017).

1.5 Tethering and communication between the ER and plasma membrane

The ER-plasma membrane (PM) contact sites are important for lipid homeostasis, calcium transfer, and maintenance of ER structure. In budding yeast, at least six proteins mediate the tethering of the ER to the plasma membrane, without which the ER takes on a collapsed morphology (Manford et al., 2012). These six tethers include the tricalbins (Tcb1, Tcb2, and Tcb3), Ist2, and the vesicle-associated membrane protein-associated protein (VAP) proteins Scs2 and Scs22. Cells lacking these tethers (Δtether) have disrupted phospholipid homeostasis and are sensitive to ER stress. The extent to which each of these phenotypes is due to the decrease in ER-PM contact sites *per se*, or if they largely result from the lack tether-specific functions is open for investigation. Notably, there is still a small amount residual cortical ER in Δtether cells, suggesting additional tethering factors beyond the six that have already been identified (Manford et al., 2012). Other proteins functioning at ER-PM contact sites, including the non-fusogenic snare protein Sec22 and ergosterol transporters of the Lam family, have been proposed as additional tethers and merit further investigation in this context (Petkovic et al., 2014; Topolska et al., 2020).

Yeast tricalbins are homologs of the mammalian extended synaptotagmins, which transfer phospholipids between the ER and plasma membrane (Saheki et al., 2016; Schauder et al., 2014; Yu et al., 2016). Tricalbins remodel the ER at contact sites with the plasma membrane to generate peaks of high curvature reaching toward the plasma membrane (Collado et al., 2019; Hoffmann et al., 2019). These peaks become more abundant at high temperatures, and *tcb1Δ tcb2Δ tcb3Δ* cells have defects in plasma membrane integrity during heat shock, suggesting a role for tricalbin-mediated contact sites in adjusting PM lipid composition in response to cellular stress. Tricalbins colocalize with other ER-PM tethers at some contact sites, but there are also contact sites that contain only one type of tether, suggesting an as-yet-unidentified functional specialization. Yeast ER-PM tethers localize differently based on local membrane curvature, with tricalbins enriched on highly curved membranes and Scs2 enriched on flat membranes (Hoffmann et al., 2019). These tethers also seem to have differing roles in cortical ER inheritance during budding yeast mitosis. Scs2 is actively delivered into the developing bud and is involved in nucleating new cortical ER, whereas Ist2 and the tricalbins are actively excluded from the bud via a septin-dependent ER diffusion barrier (see next section; Loewen et al., 2007; Sugiyama and Tanaka, 2019).

1.6 ER inheritance during budding yeast mitosis

Cell division requires the partitioning of cellular components between two cells. In budding yeast, ER tubules are delivered to the daughter bud along actin filaments by the motor protein Myo4 and an adaptor protein She3 (Du et al., 2001; Estrada et al., 2003; Fehrenbacher et al., 2002; West et al., 2011). Pioneering ER tubules are anchored to the bud tip by the VAP ortholog and ER-PM tethering protein Scs2, which interacts with a bud tip-localized protein complex called the polarisome (Chao et al., 2014; Loewen et al., 2007; Neller et al., 2015). Bud tip-localized ER then spreads to establish cortical ER within the rest of the bud in a manner that depends on the protein phosphatase Ptc1 and is inhibited by the MAP kinase Slt2 (Li et al., 2010, 2013).

A key feature of ER inheritance in yeast is the establishment of a lateral diffusion barrier in the ER membrane, which serves to strictly separate mother and daughter cell ER contents even when their membranes are still continuous (Luedeke et al., 2005). Creation of this diffusion barrier requires interactions between Scs2, the polarisome, and septins at the bud neck (Chao et al., 2014; Luedeke et al., 2005). Disruption of sphingolipid biosynthesis abolishes the diffusion barrier, indicating that lipid composition in the ER membrane composition is important for maintaining the functional distinction between mother and daughter cell ER (Clay et al., 2014).

Why do dividing cells go to the effort of creating a strictly defined boundary between mother and daughter cells? In budding yeast, damaged cellular materials accumulate with age and are retained in mother cells during cell division in order to give rise to healthy, rejuvenated daughters (Aguilaniu et al., 2003; Baldi et al., 2017; Shcheprova et al., 2008; Ünal et al., 2011). Similarly, the ER diffusion barrier prevents protein aggregates in the ER lumen from entering daughter cells, promoting daughter rejuvenation at the expense of mother cell aging (Clay et al., 2014). Mother cell ER aggregate retention also relies on Slt2, which prevents ER inheritance during ER stress (Babour et al., 2010; Piña and Niwa, 2015). While luminal protein aggregates are confined by the ER diffusion barrier, generic luminal proteins are capable of diffusing freely between mother and daughter cells (Clay et al., 2014). Whether this is simply a size-dependent phenomenon or if there are other specificity factors in the ER membrane that recognize and confine these aggregates is an interesting open question.

In addition to protein aggregates, a subset of ER-PM tethers (Ist2 and the tricalbins) is asymmetrically retained in mother cells in a septin-dependent but sphingolipid-independent manner (Okada et al., 2017; Sugiyama and Tanaka, 2019; Takizawa et al., 2000). mRNA encoding at least one of these tethers, Ist2, is actively trafficked into the bud, suggesting a concerted effort to synthesize new Ist2 in daughter cells while preventing the inheritance of old Ist2 (Takizawa et al., 2000). The relationship between aggregate and ER-PM tether retention by mother cells and whether tether retention contributes to daughter cell rejuvenation has not been addressed.

1.7 ER quality control

In addition to preventing the inheritance of toxic ER materials during ER stress, several parallel cellular quality control pathways cooperate to eliminate aberrant ER proteins, increase folding capacity and restore lipid homeostasis. One such quality control pathway is the unfolded protein response (UPR), which senses disrupted protein folding capacity in the ER lumen and transduces a stress signal to the rest of the cell. In metazoans, three separate branches are defined by the sensors ATF6, PERK and IRE1, respectively. The most well-defined of these branches, and the only one conserved in budding yeast, is the IRE1-dependent pathway. IRE1 is an ER transmembrane kinase/endoribonuclease that carries out an unconventional cytosolic splicing reaction to activate the translation of the UPR transcription factor Hac1/XBP1 (Cox and Walter, 1996; Walter and Ron, 2011).

IRE1 senses misfolded proteins via a luminal domain that can bind to ER chaperones as well as misfolded proteins themselves, though the precise interplay of these interactions and how they each contribute to IRE1 activation has not been fully defined (Walter and Ron, 2011). Upon activation, IRE1 oligomerizes and autophosphorylates via its luminal kinase domain (Ali et al., 2011; Aragón et al., 2009; Korennykh et al., 2009; Lee et al., 2008). Phosphorylation and IRE1 clustering promote interaction with *HAC1* RNA (van Anken et al., 2014; Aragón et al., 2009). IRE1-mediated splicing of *HAC1* allows it to be productively translated. Hac1 protein transcriptionally activates a range of targets, including chaperones and lipid synthesis enzymes, which together work to alleviate protein folding stress (Van Dalfsen et al., 2018; Travers et al., 2000). More recently, it was discovered that ER lipid bilayer stress activates IRE1-mediated *HAC1* splicing independent of its luminal domain (Halbleib et al., 2017; Ho et al., 2020). Interestingly, lipid bilayer stress and protein folding stress trigger distinct transcriptional responses despite acting through Ire1/Hac1, suggesting additional unidentified mechanisms controlling UPR target specificity (Ho et al., 2020).

A second overlapping pathway for cells to cope with misfolded ER proteins is ER-associated degradation (ERAD) (Wu and Rapoport, 2018). Misfolded proteins in the ER lumen are recognized by Yos9 (which binds to sugar moieties associated with protein misfolding) and the transmembrane protein Hrd3 (Denic et al., 2006; Gauss et al., 2006). ERAD substrates are then transferred to Hrd1, which forms a membrane channel that allows substrate retrotranslocation into the cytosol, harnessing energy from Cdc48-mediated ATP hydrolysis (Bodnar and Rapoport, 2017; Schoebel et al., 2017). Hrd1 polyubiquitinates retrotranslocated substrates on the cytosolic side of the membrane, targeting them to the proteasome for degradation. Misfolded transmembrane proteins similarly undergo Hrd1-dependent retrotranslocation, though this relies on separate designated targeting factors (Neal et al., 2018). ERAD of misfolded proteins on the cytosolic face of the ER membrane takes place through Doa10-mediated translocation and ubiquitination in place of Hrd1 (Schmidt et al., 2020).

Finally, cells experiencing ER stress or starvation can trigger autophagy as a means of degrading large segments of ER. Macroautophagy (referred to here as "autophagy") is a process by which toxic or extraneous cellular material is engulfed by a double membrane organelle called the autophagosome and delivered to the vacuole (lysosome in metazoans) for degradation (Morishita and Mizushima, 2019). The kinase Atg1/ULK1 is a conserved master regulator of autophagy that, upon activation, triggers autophagosome nucleation and expansion. Autophagy can occur either non-selectively, in which cargo is consumed by the autophagosome at random, or selectively through the action of autophagy receptors that define specific cargo. Autophagy receptors can serve at least two separate but related functions. First, at least some cargo-bound receptors interact with Atg1 via a protein scaffold to promote Atg1 autophosphorylation and activation, ensuring local, cargo-proximal autophagosome expansion (Kamber et al., 2015). Second, they bind simultaneously to their designated target and Atg8/LC3 family proteins on growing autophagosomes, thereby physically linking cargo to the degradation machinery.

The repertoire of known ERphagy receptors has expanded greatly in the last five years. Two budding yeast ERphagy receptors with distinct domain specificity have been identified. Atg39 degrades the perinuclear ER and some nuclear components, whereas Atg40 targets the cortical tubular ER (Mochida et al., 2015). Both autophagy receptors are transcriptionally upregulated and active in response to starvation, though only Atg39 is required for cell survival in this context (Cui et al., 2019; Mizuno et al., 2020; Mochida et al., 2015). The COPII cargo adaptor complex Lst1-Sec23 is required for Atg40-mediated autophagy and is recruited to sites of ERphagy in an Atg40- and Lnp1-dependent manner, suggesting a role for both Lnp1 and COPII in remodeling the ER membrane for delivery into autophagosomes (Cui et al., 2019). Atg40 self-association and reticulon-like membrane bending are also required for starvation-induced ERphagy via a proposed curvature-dependent membrane fragmentation mechanism (see ER morphology section above). While most ERphagy receptors identified to date are transmembrane proteins, a cytosolic receptor responsible for degrading the ER in response to ER stress was recently discovered in fission yeast (Zhao et al., 2020). The receptor, Epr1, is upregulated upon UPR activation and binds to VAP proteins on the ER membrane and interfaces with Atg8 to mediate ERphagy. The reasons for using a cytosolic ERphagy receptor over a membrane-embedded one are unclear, but one possibility is that the modularity of Epr1 allows it to target autophagic cargo more precisely.

A slew of mammalian ERphagy receptors have been identified, including FAM134B, Rtn3, Atl3, TEX264, Sec62 and Ccpg1 (Chino and Mizushima, 2020). Of this group, FAM134B was the first identified and best characterized in the context of autophagy (Khaminets et al., 2015). Mutation of FAM134B causes sensory neuropathy in mice and humans, highlighting the crucial physiological role of ERphagy. Like Atg40, FAM134B, Rtn3 and Atl3 all contain reticulon homology domains that are important for their function in autophagy (Bhaskara et al., 2019; Chen et al., 2019; Grumati et al., 2017; Jiang et al., 2020).

Considering ERphagy degrades large fragments of ER at a time, an important and largely unanswered question is whether and how specificity is achieved in selecting cargo for ERphagy. A global proteomics analysis suggested that around one-third of the ER proteome is subject to TEX264-mediated autophagy (An et al., 2019). TEX264 is enriched in three-way ER junctions, so this bias may simply reflect the fact that other proteins also localize disproportionately to this ER subdomain (Chino et al., 2019). In a separate analysis, Rtn3 was the only known ERphagy receptor to appreciably affect the degradation of proinsulin aggregates, though the basis by which Rtn3 senses these aggregates and how cargo interaction affects receptor activity are unknown (Cunningham et al., 2019). Perhaps the most well characterized case of ERphagy substrate specificity is in the regulation of procollagen aggregation. Misfolded procollagen in the ER lumen is recognized by the chaperone protein Calnexin, which binds to FAM134B to promote ERphagy and prevent collagen aggregate accumulation (Forrester et al., 2019). While the vast number and diversity of mammalian ERphagy receptors suggests functional specialization, we are only beginning to understand the basis for their unique regulation and cargo specificity.

ERphagy, ERAD and the unfolded protein response are overlapping, not mutually exclusive mechanisms that cooperate to ensure cell health and survival in response to disrupted ER homeostasis. ERAD components are transcriptionally upregulated by Hac1 during ER stress, and simultaneous disruption of ERAD and UPR signaling is lethal in yeast cells (Van Dalfsen et al., 2018; Travers et al., 2000). Similarly, Rtn3-mediated ERphagy cooperates with ERAD to prevent proinsulin aggregation (Cunningham et al., 2019), and overwhelming the ERAD machinery by overexpressing an aggregate prone ER protein results in the induction of ERphagy in yeast (Cui et al., 2019). These results and others indicate that there is considerable crosstalk and compensation between various avenues of ER quality control.

1.8 Meiosis as a model system for gene regulation and cell remodeling during development

Meiosis is a conserved cell differentiation process that enables sexual reproduction in eukaryotes through the production of specialized gamete cells. Two key features of gametogenesis are conserved from yeast to humans. First, the chromosome remodeling that regulates sister chromatid recombination and reductional chromosome segregation is essential for producing genetically diverse haploid cells from a diploid precursor (Marston and Amon, 2004). Second, age-associated damage that accumulates in all cellular compartments in somatic cells must be eliminated from the germline in order to ensure the production of healthy, youthful offspring (Goodman et al., 2020). Thus, the production of functional gametes necessitates extensive monitoring and quality control of cellular contents prior to their inheritance.

Virtually every aspect of cell physiology is remodeled during meiosis. This remodeling happens in several stages that must be coordinated to ensure the proper distribution of cellular material. Budding yeast can be induced to undergo meiosis synchronously, making it a tractable system for genome-wide analysis of the gene regulatory events that coordinate each stage of meiotic differentiation (Brar et al., 2012; Otto and Brar, 2018). These analyses have revealed unanticipated gene regulatory mechanisms, including extensive translational regulation (Berchowitz et al., 2013, 2015; Brar et al., 2012; Carlile and Amon, 2008) and protein downregulation through the expression of a repressive extended transcript isoform (Chen et al., 2017; Cheng et al., 2018; Chia et al., 2017). These unexpected yet elegant mechanisms highlight the value of budding yeast meiosis as a system for studying developmental gene regulation. In chapter 4, I present work defining the widespread use of transcript isoform toggling to dynamically control protein production in meiosis.

Budding yeast meiosis is a rich model system for studying cell biology during developmental transitions. Meiotic cells synthesize four new gamete plasma membranes and define which cellular contents go in and which are excluded (Moreno-Borchart and Knop, 2003; Neiman, 2011). Organelles are packaged into gametes but nuclear pores and protein aggregates are omitted (King et al., 2019). The vacuole swells dramatically and explodes with precise timing (Eastwood et al., 2012). The intricately organized mitochondrial network dramatically collapses as the proteins tethering it to the plasma membrane undergo developmentally regulated degradation (Sawyer et al., 2019; Suda et al., 2007). At the end of this process, gametes emerge rejuvenated, free from any scars of aging borne by their precursor cell (Ünal et al., 2011). Each new inquiry into the cell biological phenomena mediating gametogenesis reveals novel insight into the evolutionary imperatives this process entails and the surprising mechanisms developed to address them.

The ER network is dramatically remodeled in budding yeast meiosis. The cortical ER detaches from the plasma membrane via an unknown mechanism and appears to take on a "collapsed" morphology by late meiosis (Suda et al., 2007). In chapter 2, I present work exploring key events in meiotic ER remodeling. We define a developmental transition from continuous to fragmented ER, which is important for both ER inheritance and selective elimination. We identify two parallel mechanisms by which ER is degraded in meiosis. Together this work serves as an atlas of ER remodeling in meiosis and provides a framework for further investigation of ER quality control in meiosis.

Chapter 2: Programmed ER remodeling drives selective inheritance and degradation in budding yeast meiosis

2.1 Abstract

The endoplasmic reticulum (ER) is a membrane-bound organelle with diverse functions that rely on the maintenance of membrane shape and distribution within cells. Accordingly, ER structure and function are remodeled in response to changes in cellular demand, such as the presence of external stressors or the onset of cell differentiation. Mechanisms controlling ER remodeling during cell differentiation are not well understood. Here, we describe a series of developmentally regulated changes in ER morphology and composition during budding yeast meiosis, a conserved cell differentiation program that gives rise to specialized gamete cells. During meiosis, the cortical ER undergoes apparent fragmentation before collapsing away from the plasma membrane. This programmed collapse depends on the ER membrane structuring proteins Lnp1 and reticulons, as well as the actin cytoskeleton. A subset of ER is retained at the mother cell plasma membrane, and thereby excluded from inheritance by gametes, via the action of ER-plasma membrane tethering proteins. Meiotic ER remodeling is coupled to ER degradation by selective autophagy, which is triggered by the developmentally regulated expression of the ER-specific autophagy receptor Atg40. ER autophagy relies on ER collapse, as artificially targeting ER proteins to the cortically retained ER pool prevents their degradation. Thus, developmentally programmed changes in ER morphology determines selective exclusion, degradation and inheritance of ER subdomains by gamete cells, highlighting a novel axis of ER quality control during cell differentiation.

2.2 Introduction

The endoplasmic reticulum (ER) is a membrane-bound organelle that carries out a range of essential and conserved cellular functions, including protein synthesis and trafficking, lipid metabolism, and inter-organelle communication. These functions rely on the maintenance of ER structure and subcellular distribution, which are achieved through membrane-shaping proteins, fusion and fission of ER tubules, and tethering between the ER and other cellular structures, including organelles and the plasma membrane (reviewed in Westrate et., al. 2015; Schwarz and Blower, 2016). ER structure is highly dynamic even in unperturbed cells, and is dramatically remodeled in response to changes in cellular demand, such as protein folding stress or cell differentiation. Mutations that disrupt ER morphology are linked to a range of neurodegenerative diseases, including Alzheimer’s disease, amyotrophic lateral sclerosis, and hereditary spastic paraplegia (Öztürk et al., 2020; Renvoisé and Blackstone, 2010), highlighting the intimate connection between ER structure and function, and the importance of ER quality control during cell differentiation.

The ER emanates from the nuclear envelope to surround the nucleus (perinuclear ER) and spreads to the cell periphery (cortical ER) where it forms extensive contacts with the plasma membrane. In budding yeast, ER-plasma membrane (ER-PM) contacts are maintained by at least six tethering proteins, including Ist2, the tricalbins Tcb1, Tcb2 and Tcb3, and the vesicle-associated membrane protein-associated protein (VAP) orthologs Scs2 and Scs22 (Manford et. al., 2012). All six tethers are integral ER membrane proteins that interact with phospholipids or proteins on the plasma membrane. Cells lacking these tethers have dramatically reduced cortical ER, disrupted lipid homeostasis, and acute sensitivity to ER stress, underscoring the importance of membrane tethering in maintaining ER structure and function. A second class of proteins involved in structuring the cortical ER is the reticulons, which form wedge-like structures in the cytosolic leaflet of the ER membrane to promote membrane curvature and drive the formation of ER tubules (Hu et al., 2008; Voeltz et al., 2006). ER tubules are highly dynamic, constantly growing, retracting, and fusing with one another to generate three-way tubule junctions. Fusion is mediated by the dynamin-like GTPases Sey1 (in budding yeast) or Atlastin (in metazoans) (Anwar et al., 2012; Hu et al., 2009b; Orso et al., 2009). Lunapark (Lnp) family proteins are involved in the maintenance of three-way junctions and display functional antagonism with Sey1/Atlastin though its precise mechanistic role in this process remains unclear (Casey et al., 2015; Chen et al., 2012; Wang et al., 2016). While factors that define ER structure are conserved across eukaryotes, we are only beginning to understand the diverse ways in which ER morphology and dynamics promote ER function.

Despite the fundamental relationship between ER structure and function, our knowledge of how the ER is remodeled as cells adapt to changing cellular conditions is limited. In budding yeast and cultured mammalian cells, exposure to chemical reducing agents causes ER protein folding stress and activation of the ER unfolded protein response (UPR), resulting in an expansion of ER sheets and increased ER volume (Walter and Ron, 2011; Schuck et. al., 2009; Fumagalli et. al., 2016). Both ER stress and nutrient starvation drive selective degradation of the ER by autophagy (ERphagy), a response which is essential for cell adaptation and survival in these conditions (Mochida et. al., 2015; Khaminets et. al., 2015; Fumagalli et. al. 2016; Zhang et. al. 2020). While these studies provide crucial insight into ER quality control pathways that respond to cellular stress, the relationship between harsh drug treatment or prolonged starvation and the physiological conditions under which ER remodeling occurs is unclear. Natural processes which produce diverse and intricate ER structures, such as neuronal and muscle cell differentiation, are generally not amenable to live cell imaging, limiting our ability to study the dynamics of ER remodeling under these conditions. Here, we use budding yeast meiosis to study ER remodeling in real time in a natural developmental context.

Meiosis is a conserved cell differentiation program that produces gamete cells specialized for sexual reproduction. In meiosis, a diploid progenitor cell undergoes a single chromosome duplication event followed by homolog pairing, recombination and two successive rounds of chromosome segregation, resulting in genetically distinct haploid gametes. In addition to ensuring the proper distribution of chromosomes, cells undergoing meiosis must deliver a full complement of cellular components while preventing the inheritance of toxic or deleterious material. While the regulation of meiotic chromosome segregation is well studied, mechanisms governing the inheritance and elimination of other cellular components during meiosis are relatively poorly defined.

In this study, we define key steps and mechanisms in ER inheritance and quality control budding yeast meiosis. During meiosis, the cortical ER undergoes apparent fragmentation into new subcompartments and collapses from the plasma membrane, a process which depends on the meiotic transcription factor Ndt80 but not chromosome segregation itself. Fragmentation and cortical detachment rely on reticulon proteins and Lnp1, while collapse depends on the actin cytoskeleton. A subset of ER fragments is retained at the plasma membrane, and therefore excluded from gametes, in an ER-PM tether-dependent manner. In late meiosis, the ER is subject to extensive degradation by a selective autophagy mechanism that depends on cortical ER collapse, as ER proteins that naturally or artificially localize to the cortically retained ER compartment are exempt from autophagic degradation. Together, our work defines a developmental quality control mechanism in which programmed changes in ER morphology determine both the inheritance and selective exclusion of ER subdomains by gamete cells.

2.3 Results

2.3.1 The ER detaches from the plasma membrane during meiosis

Meiotic differentiation involves regulated partitioning of organelles to ensure the development of healthy spores. In order to characterize ER dynamics during meiotic differentiation, we used time-lapse microscopy to monitor cells expressing fluorescent markers of the ER lumen (GFP-HDEL) and chromatin (Htb1-mCherry). Premeiotic cells displayed characteristic ER morphology, with ER distributed around the cell periphery (cortical ER) and the nucleus (perinuclear ER). As cells progressed through meiosis, the cortical ER underwent a striking series of morphological changes occurring in discrete steps. First, shortly before anaphase I, the cortical ER coalesced into bright, highly dynamic rope-like structures, a phenomenon we refer to as “ER cabling” (figure 2.1A-B). Next, concurrent with anaphase II, the ER detached from the cell periphery and abruptly relocalized to an area in the center of cells roughly bounded by the four gamete nuclei (figure 2.1A, C). We refer to the abrupt detachment of cortical ER as “ER collapse”, a phenomenon that was previously observed in fixed cells during late meiosis but has not yet been characterized in live cells (Suda et. al. 2007). Finally, as spore packaging progressed, collapsed ER was inherited by each gamete and took on the characteristic cortical and perinuclear structures seen in premeiotic cells (figure 2.1A, H).

In budding yeast, meiosis is coupled to spore formation, in which gamete plasma membranes (also called prospore membranes) are synthesized de novo and grow to encapsulate the full complement of cellular material to be inherited by gametes (Neiman, 2011). Imaging the ER alongside a marker of prospore membrane synthesis, mKate-Spo20$^{51\text{-}91}$ (Nakanishi et al., 2004), revealed that ER collapse takes place after prospore membrane nucleation but prior to closure (figure 2.1D-E). Based on the timing of ER collapse and the spatial relationship between collapsed ER and nascent prospore membranes, it appears that cortical ER collapse is an important step in its delivery into gamete cells.

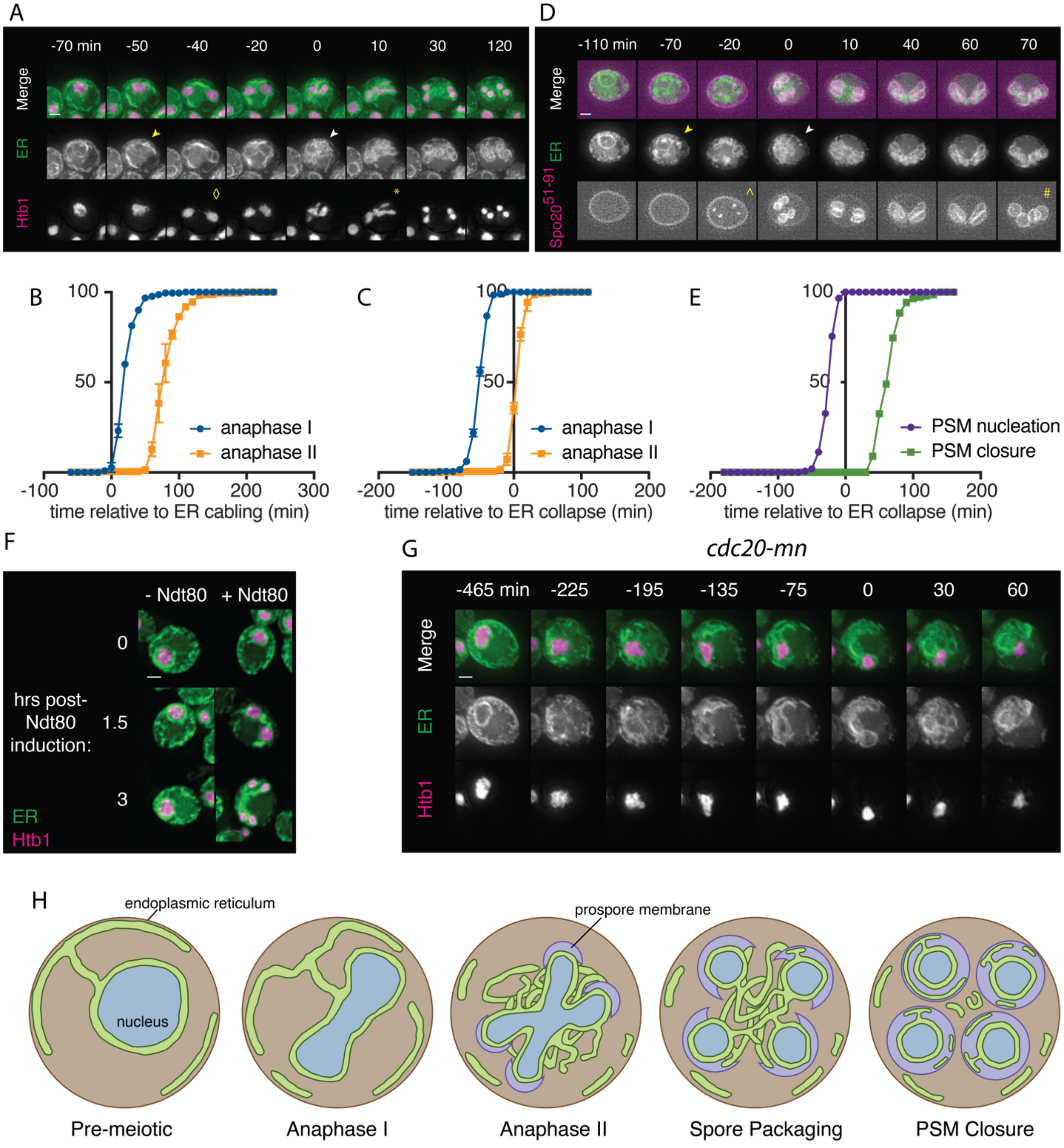

Figure 2.1. The ER undergoes developmentally regulated structural remodeling during meiosis. (A) Time-lapse microscopy of cells expressing GFP-HDEL to mark the ER (ER) and either Htb1-mCherry to mark chromatin (Htb1) imaged every 10 minutes during meiosis. Symbols mark the onset of ER cabling (yellow arrowhead), ER collapse (white arrowhead), anaphase I (◊) or anaphase II (*). 0 min is defined as the time of ER collapse. (B) Quantification of the time of anaphase I and anaphase II relative to the onset of ER cabling. (C) Quantification of the time of anaphase I and anaphase II relative to ER collapse. (DTime-lapse microscopy of cells expressing GFP-HDEL (ER) and mKate-Spo20$^{51\text{-}91}$ to mark the prospore membrane (PSM) imaged every 10 minutes during meiosis. Symbols mark PSM nucleation (^) and closure (#). (E) Quantification of the time of PSM nucleation and closure relative to ER collapse. (F) As in (A) but with cells with the endogenous promoter of *CDC20* replaced with the mitosis-specific *CLB2* promoter (*cdc20-mn*), and cells imaged every 15 minutes. (G) Cells expressing GFP-HDEL (ER), Htb1-mCherry (Htb1) and an estrogen-inducible allele of *NDT80* treated with 1 µM β-estradiol (+ Ndt80) or vehicle (-Ndt80) after 5 hours in sporulation media and imaged at the indicated times after induction. (H) Schematic of meiosis-coupled ER remodeling with organelles and stages of meiosis and spore formation labeled. Scale bar for all panels = 2µm.

The precise timing with which ER detachment takes place relative to meiotic chromosome segregation and prospore membrane formation suggests that this process is tightly regulated as part of the broader developmental program that coordinates meiosis and spore formation. To further test this idea, we disrupted normal meiotic progression and assessed the impact on ER dynamics. First, we arrested cells in prophase I by withholding the meiotic transcription factor Ndt80, which is required to initiate the two meiotic nuclear divisions following homologous recombination (figure 2.1F) (Benjamin et al., 2003; Chu and Herskowitz, 1998). Arrested cells did not undergo ER cabling or collapse, indicating that these processes happen downstream of Ndt80 induction and not merely in response to the nutrient-poor conditions that stimulate meiosis in budding yeast. We next blocked meiotic chromosome segregation using an allele of the anaphase-promoting complex/cyclosome (APC/C) activator Cdc20 that is not expressed in meiosis (*cdc20-mn*; Lee and Amon, 2003). Cortical ER in *cdc20-mn* cells still detached from the plasma membrane and coalesced around the single, undivided nucleus, reminiscent of the anaphase II morphology observed in wild type cells (figure 2.1G). Together, these data indicate that meiotic ER remodeling is triggered by a developmental cue downstream of Ndt80 but independent of chromosome segregation.

2.3.2 ER-plasma membrane tethers define a cortically retained ER compartment

How is the abrupt detachment of the ER from the plasma membrane (PM) achieved? In budding yeast, at least six proteins function as ER-PM tethers. These include Ist2, the tricalbins Tcb1, Tcb2 and Tcb3, and the vesicle-associated membrane protein-associated protein (VAP) orthologs Scs2 and Scs22. Mitotic cells lacking all six tethers have drastically reduced levels of cortical ER, disrupted lipid homeostasis, and reduced tolerance to ER stress (Manford et. al., 2012). We sought to determine the role of ER-PM tethering proteins in meiotic ER collapse by imaging each tether during meiosis. To our surprise, Ist2 and all three tricalbins remained cortically localized throughout meiosis, even during anaphase II when the ER has collapsed (figure 2.2A, 2.S1A-D). In contrast, Scs2 and Scs22 demonstrated collapsed morphology during anaphase II (figure 2.2A, 2.S1E-F).

The cortical retention of a subset of ER-PM tethers was unexpected because all four proteins have integral membrane domains anchoring them in the ER and are therefore predicted to localize with the bulk of the ER. We therefore tested whether the cortically retained ER-PM tethers represented previously overlooked fragments of ER that failed to detach from the PM with the bulk of the ER. Imaging Tcb3-mKate alongside GFP-HDEL revealed that Tcb3 signal at the cell cortex indeed overlapped with small islands of ER lumen, even when the vast majority of the ER was collapsed (figure 2.2B). Together, our observations indicate that a subset of ER-PM tethers define a previously unappreciated, cortically retained ER compartment.

Because the gamete plasma membrane is formed de novo rather than inherited from the progenitor cell, any cellular component that is attached to the mother plasma membrane is necessarily excluded from gametes. We observed an abrupt decrease in the signal of all four excluded tethers in late meiosis, suggesting that excluded ER fragments are degraded during this time (figure 2.2C, 2.S1G). Late in meiosis, the yeast vacuole dramatically expands before ultimately lysing, releasing its contents into the ascoplasm region outside of spores, resulting in the degradation of material that has been excluded from spores, including protein aggregates and nuclear pore complexes (Eastwood et. al., 2012; King et. al., 2019). To determine whether this is also the mechanism responsible for eliminating cortically retained ER, we performed time-lapse imaging of cells expressing Vph1-mCherry along with Tcb3-GFP or GFP-Ist2. Vacuole lysis, as marked by a switch in mCherry signal from vacuole membrane-localized to diffuse, coincided perfectly with the disappearance of cortical ER signal, supporting a model in which the release of vacuolar proteases into the ascoplasm is responsible for the degradation of cortically retained ER (figure 2.2C, 2.S1G). Thus, cortical ER retention is a means by which cells can exclude portions of the ER from gamete cells, and may serve as an ER quality control mechanism during meiotic differentiation.

2.3.3 ER-PM tethers promote the cortical retention of ER fragments during ER collapse

Cortically retained ER fragments represent a relatively small portion of the cell's total ER pool. Nonetheless, we observed considerable cell-to-cell heterogeneity in the amount of retained cortical ER in our live-cell microcopy experiments. To quantify this heterogeneity, and to enable us to assess the effect of genetic manipulation on cortical ER retention, we developed a metric in which we classified cells into four distinct groups: class I (no discernable ER retention), class II (small cortical ER fragments), class III (intermediate between classes II and IV), and class IV (large spans of cortical ER) (figure 2.2D). The vast majority of wild-type cells scored at anaphase II of meiosis fell into classes II and III, though we did observe a small subset of class I and class IV cells (figure 2.2E). Deletion of the four cortically retained tethers (4xΔtether) resulted in a significant increase in the frequency of cells falling into class I, and fewer cells in class III, indicating an overall decrease in the amount of retained cortical ER in this genotype (figure 2.2E, 2.S1K). Cells lacking only a subset of these four tethers showed an intermediate phenotype, suggesting that the loss of ER-PM tethers has an additive effect on the amount of retained cortical ER (figure 2.2E, 2.S1H-I). We conclude that Ist2 and the tricalbins promote the exclusion and subsequent degradation of cortical ER fragments in meiosis.

2.3.4 Clustering of ER-PM tethers precedes ER collapse

The contrasting dynamics between the four retained ER-PM tethers and the bulk of the ER is striking. We noted that, while these tethers did not collapse with the rest of the ER, their behavior was not entirely static over time. Early in meiosis, tether signal was distributed relatively homogenously around the cell cortex, as expected, based on its known mitotic localization. However, this pattern changed as meiosis progressed, with tether signal becoming more clustered over time, resulting in tether-rich islands separated by stretches of cell cortex with no tether signal (figure 2.2F). To quantitatively assess the degree to which tether signal is asymmetrically distributed within the cell cortex, we employed a metric called the Gini coefficient (G), which measures inequality within a dataset on a scale from zero to one (Rouskin et al., 2014; Wittebolle et al., 2009). If tether signal were distributed perfectly evenly throughout the cell cortex, it would receive a Gini coefficient of zero, whereas a highly asymmetric distribution of signal would be closer to one. Cells in early meiosis had a relatively low Gini coefficient for GFP-Ist2 distribution (G = 0.153 +/- 0.034) (figure 2.2F-G). This value steadily increased over time before plateauing (G = 0.304 +/- 0.049) at the time of ER collapse. This analysis demonstrates that the onset of tether clustering precedes ER collapse by several hours and therefore represents an early step in meiotic ER remodeling. Though the exact relationship between tether clustering and ER collapse is still unclear, our observations support a model in which the cortical ER separates into tether-containing (cortically retained) and tether-free (collapsed) domains to allow selective ER inheritance by gametes (figure 2.2H).

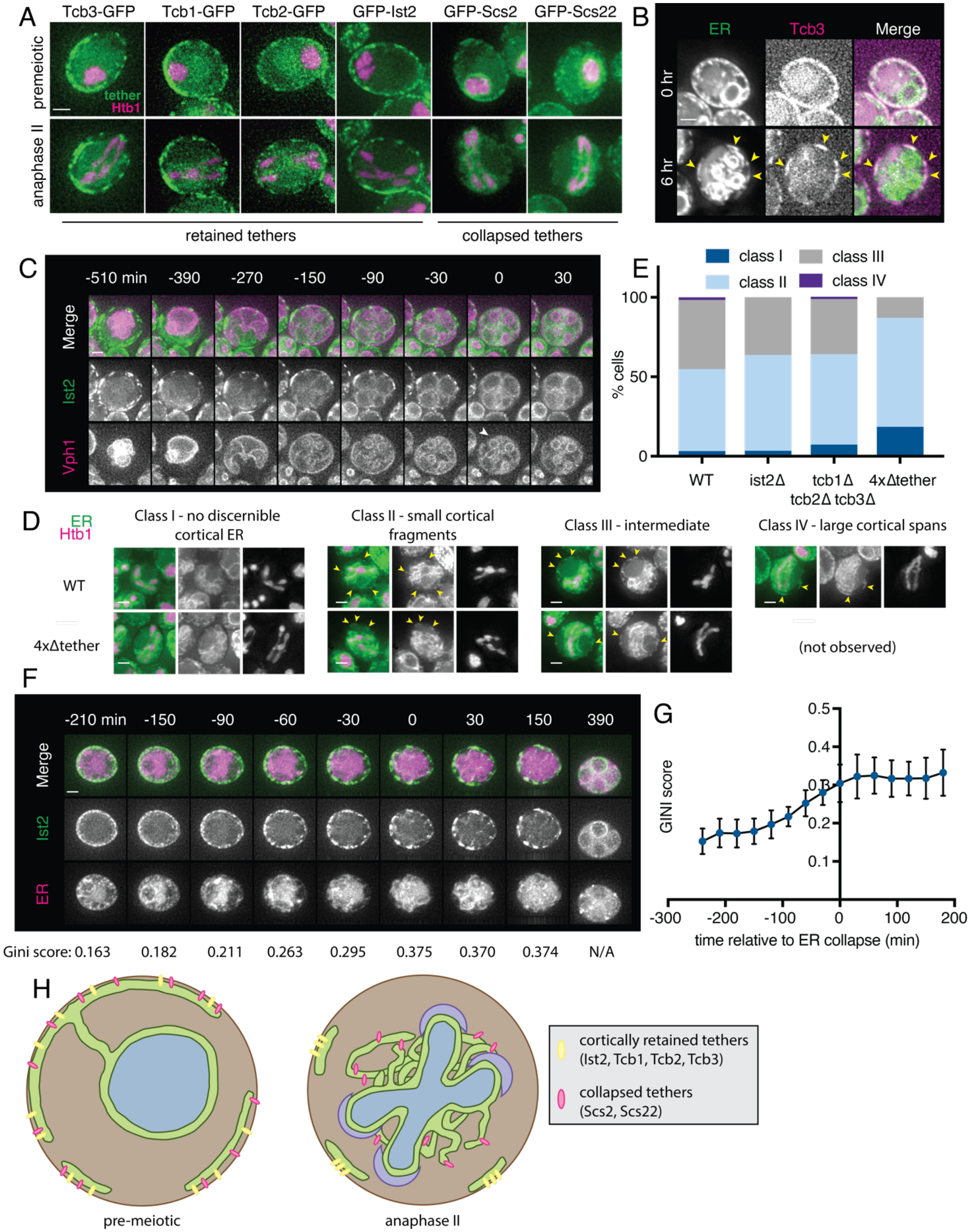

Figure 2.2. A subset of ER-PM tethering proteins marks cortically retained ER islands. (A) Time-lapse microscopy of cells expressing the indicated ER-PM tether tagged with GFP (tether) and Htb1-mCherry (Htb1) imaged during meiosis. A representative cell is shown prior to meiosis (top) and during anaphase II (bottom). Tethers are categorized as retained or collapsed based on anaphase II localization. (B) Cells expressing GFP-HDEL (ER) and Tcb3-mKate (Tcb3) imaged at 0 hr (top) and 6 hr (bottom) after introduction to SPO. Arrowheads mark islands of colocalized ER lumen

and Tcb3 signal. (C) Time-lapse microscopy of cells expressing GFP-Ist2 and Vph1-mCherry to mark the vacuole imaged every 30 minutes in meiosis. Arrowhead marks the time of vacuole lysis, which is defined as time 0. (D) Images of WT or ist2Δ tcb1Δ tcb2Δ tcb3Δ (4xΔtether) cells expressing GFP-HDEL (ER) and Htb1-mCherry (Htb1) taken at anaphase II. When possible, a representative cell of each genotype is shown for each indicated cortical ER classification. (E) Quantification of n >100 cells for the indicated genotypes following the classification system in (D). (F) Time-lapse microscopy of cells expressing GFP-Ist2 and mCherry-HDEL (ER) imaged every 30 minutes. The GINI score based on quantification of Ist2 signal is shown below each timepoint. Minute 0 is defined as the time of ER collapse. (G) GINI quantification based on cortical Ist2 signal over time. Values are the average of 10 cells scored across each timepoint. Error bars represent standard deviation. (H) Schematic showing ER morphology and tether localization in pre-meiotic and anaphase II cells. Scale bar = 2 μm for all panels.

2.3.5 Reticulons promote ER detachment

How is the normally continuous cortical ER separated into collapsed and retained pools? One means of separating a continuous compartment into two separate topologies is by membrane fission, a phenomenon underlying key biological processes such as endocytosis, mitochondrial division, and cytokinesis. While the molecular mechanisms driving many membrane fission events are well characterized, the regulation of membrane fission in the ER is relatively poorly defined. Nevertheless, a growing body of evidence supports a role for membrane curvature in driving ER tubule fission *in vitro* and *in vivo*. Reticulons are a conserved class of proteins that generate ER membrane curvature via a double-hairpin reticulon homology domain (RHD) (Voeltz et. al., 2006; Hu et. al., 2008). Overexpression of reticulon proteins results in ER fragmentation in cell culture and Drosophila models, while *in vitro* reconstituted ER networks containing reticulons spontaneously fragment in the absence of fusion-promoting factors (Wang et. al., 2016; Powers et. al. 2017; Espadas et. al., 2019). These observations led us to pursue the hypothesis that reticulons mediate the topological separation of retained and collapsed ER by promoting curvature-dependent membrane fission.

Budding yeast have two reticulons, Rtn1 and Rtn2, as well as a reticulon-like protein Yop1, that together are required for normal ER tubule formation (Voeltz et. al., 2006). As expected, *rtn1Δ rtn2Δ yop1Δ* mutants displayed a drastic reduction in tubules and an apparent increase in ER sheet structures under mitotic growth conditions (figure 2.S2A). Additionally, in meiotic cells, we observed a striking increase in the amount of ER that remained cortically localized beyond anaphase II (figure 2.3A-B). Relative to WT, *rtn1Δ rtn2Δ yop1Δ* cells were much less likely to have class II cortical ER at anaphase II and much more likely to fall into class IV. Moreover, the cabling behavior that we observe in WT cells immediately prior to collapse was absent in *rtn1Δ rtn2Δ yop1Δ* cells, suggesting that membrane curvature and/or fission are important for ER cabling, and that the cabling process may promote cortical ER detachment (figure 2.3A, 2.S2B-C). These observations support a role for reticulon-mediated membrane curvature in promoting meiotic ER collapse via fragmentation.

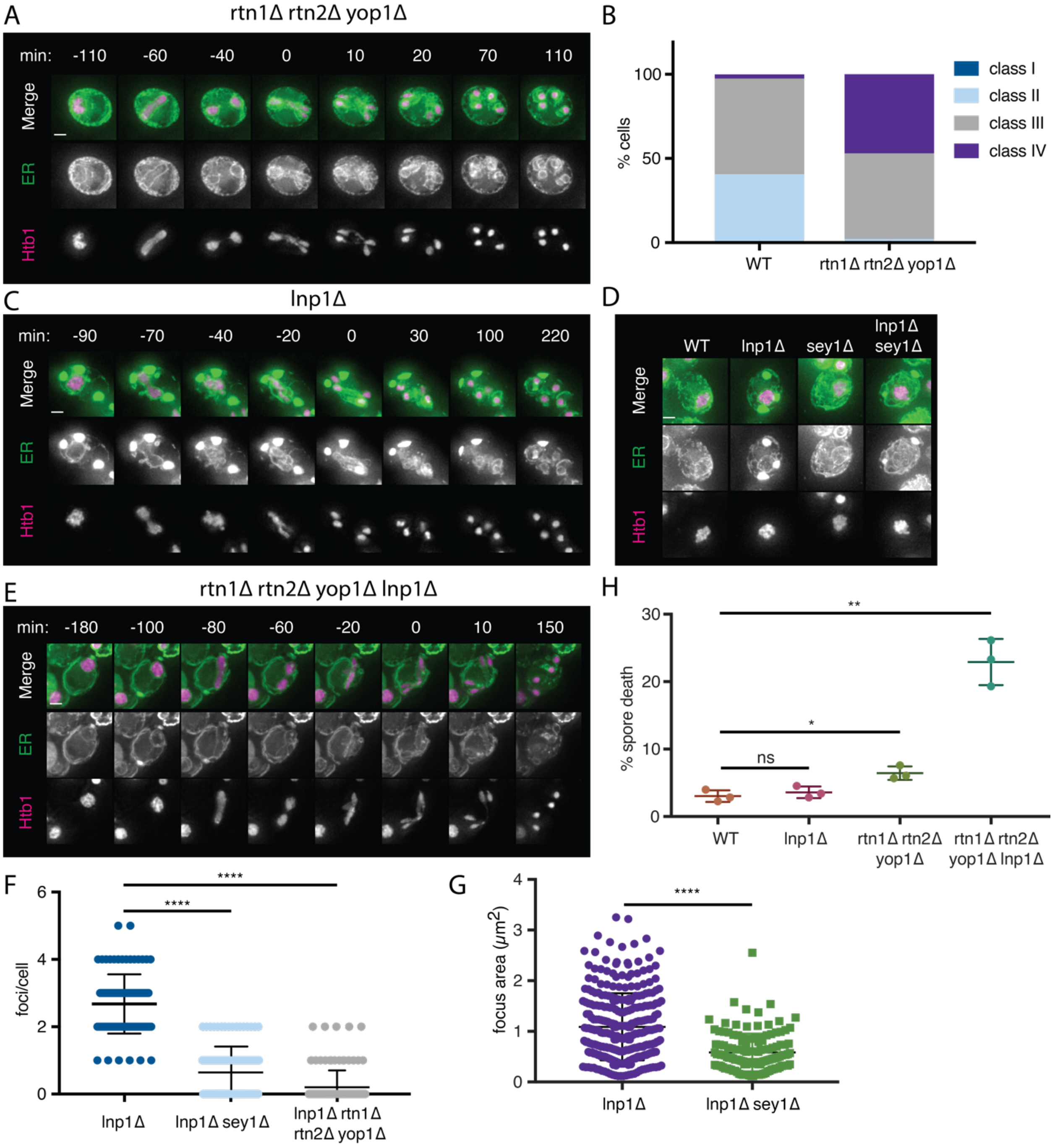

Figure 2.3. Reticulons and Lnp1 regulate meiotic ER remodeling. (A) Time-lapse microscopy of rtn1Δ rtn2Δ yop1Δ cells expressing GFP-HDEL (ER) and Htb1-mCherry imaged every 10 minutes during meiosis. Time 0 is defined as the time of ER collapse. (B) Classification of n > 100 cells for the indicated genotypes. (C) As in (A) but with cells of genotype lnp1Δ. (D) Cells of the indicated genotypes expressing GFP-HDEL and Htb1-mCherry imaged at 0 hr in SPO. (E) As in (A) but with cells of genotype rtn1Δ rtn2Δ yop1Δ lnp1Δ. (F) Quantification of the number of foci/cell for n > 100 cells of each of the indicated genotypes. Average and standard deviation are shown. (G) Quantification of focus size for n>100 cells of each of the indicated genotypes. Average and standard deviation are shown. (H) Spore viability quantification after 24 hr in SPO followed by germination for 48 hours on YPD. Each replicate represents results for at least 176 individual spores. Scale bar = 2 μm for all panels.

2.3.6 Lnp1 is required for ER detachment

Both normal ER tubule fission in unperturbed cells and ER fragmentation upon reticulon overexpression can be countered by homotypic membrane fusion, which is carried out by the dynamin-like GTPase Sey1 (Atlastin in plants and metazoans) (Wang et. al. 2016; Espadas et. al. 2019; Hu et. al., 2009; Orso et. al. 2009; Anwar et. al., 2012). While the factors regulating Sey1/Atlastin activity are incompletely defined, the lunapark protein Lnp1 displays functional antagonism with Sey1 in mitotic yeast cells (Chen et. al., 2012). We reasoned that Lnp1 may directly or indirectly promote ER collapse by negatively regulating Sey1-mediated ER membrane fusion. If this were the case, cells lacking Lnp1 would be expected to show increased ER retention.

To our surprise, and in contrast to mitotic cells, *lnp1Δ* mutants displayed massive cortical ER puncta when placed in sporulation media (figure 2.3C, 2.S2D). We examined multiple ER markers, including luminal and transmembrane proteins, and found that all of them localized to large ER puncta in *lnp1Δ* cells, indicating that these aberrant structures are generally representative of ER in this condition (figure 2.S2E). Consistent with a role for Lnp1 in promoting ER detachment, ER puncta in *lnp1Δ* cells retained their cortical localization throughout meiosis and spore packaging, resulting in their exclusion from gamete cells (figure 2.3C). Puncta in *sey1Δ lnp1Δ* double mutants were smaller and less abundant than those found in *lnp1Δ* mutants, suggesting that these phenotypes result from excessive Sey1-mediated membrane fusion (figure 2.3D, F-G).

To determine the relationship between reticulons and Lnp1 in promoting ER collapse, we examined ER dynamics in the quadruple mutant *lnp1Δ rtn1Δ rtn2Δ yop1Δ*. Strikingly, these mutants rarely formed ER foci, suggesting that foci are normally comprised of highly reticulated and/or fragmented ER (figure 2.3F). Moreover, they showed a dramatic increase in cortical ER retention during anaphase II, with all observed cells observed falling into class IV (figure 2.3E). We also found that *lnp1Δ rtn1Δ rtn2Δ yop1Δ* mutants had dramatically reduced spore viability, whereas mutants lacking only the three reticulons had a modest viability defect and *lnp1Δ* cells were unaffected (figure 2.3H). Together, these data reveal a role for the regulation of membrane shape and fusion in ensuring normal ER detachment during meiosis and, ultimately, the health of the gametes produced during this process.

2.3.7 Artificial ER-PM tethering does not prevent ER collapse

Impaired ER collapse in cells lacking reticulons could result directly from reduced reticulon-dependent tubule severing, or indirectly from altered ER morphology. We thus asked whether we could artificially tether cortical ER to the plasma membrane throughout meiosis without altering reticulon levels (figure 2.4A). We constitutively tethered GFP-Scs2 to the cell cortex using the plasma membrane protein Pil1 fused to a genomically encoded antibody against GFP (Pil1-antiGFP; Schmidt et. al., 2018). Whereas Scs2-GFP in WT cells localized with collapsed ER in anaphase II, GFP signal remained strictly cortical in cells expressing Pil1-antiGFP, indicating that our artificial tethering strategy was successful (figure 2.4B-C). To our surprise, this manipulation did not have a strong effect on overall cortical ER retention at anaphase II, as assessed by mCherry-HDEL localization, which was largely collapsed in late meiosis. This result shows that

that introducing an artificial constitutive ER-PM tether does not prevent collapse, and, incidentally, that cortical release of the ER-PM tether Scs2 does not drive meiotic ER collapse.

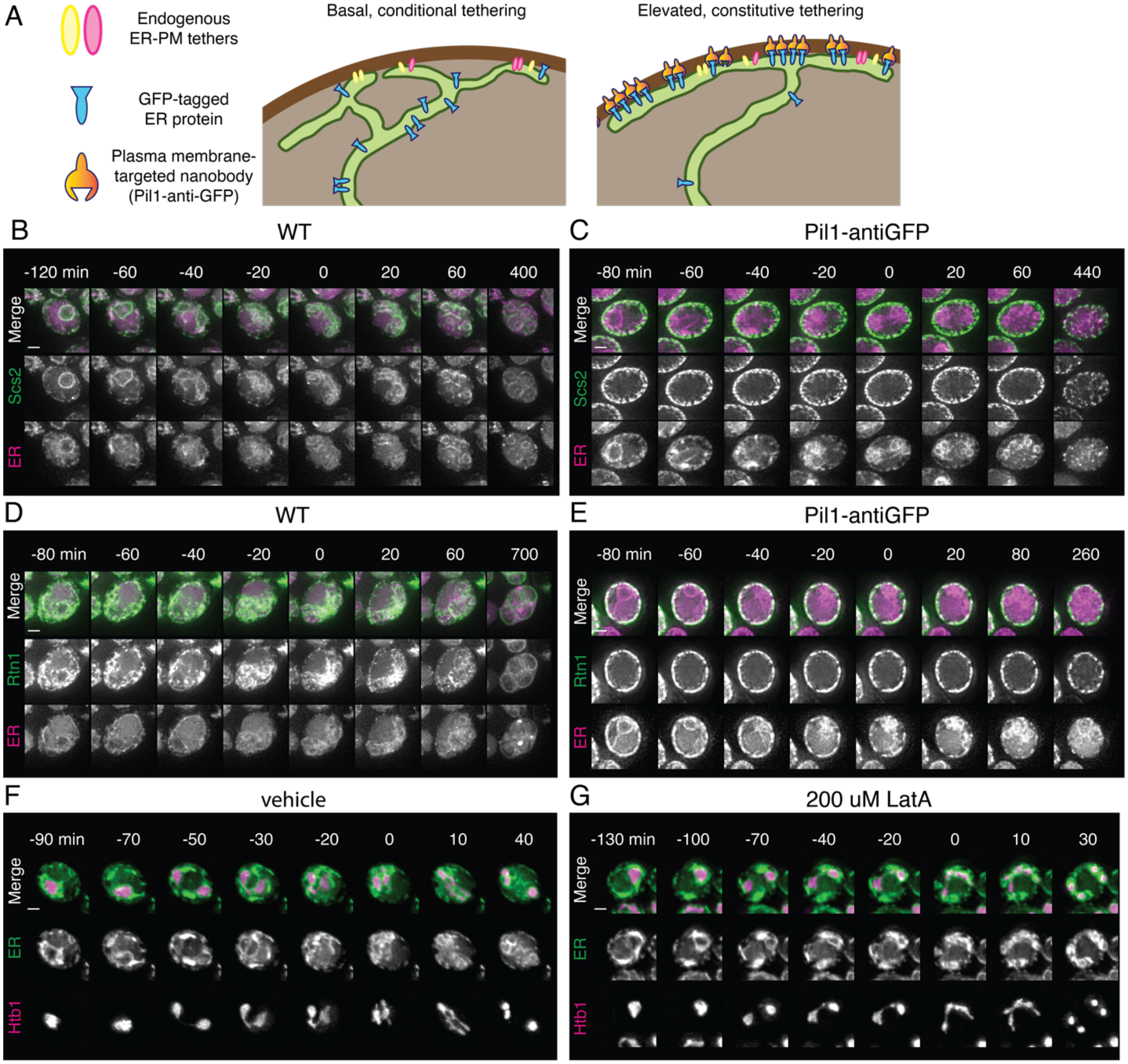

Figure 2.4. Artificial cortical ER tethering does not prevent ER collapse. (A) Schematic of artificial cortical ER tethering using Pil1-antiGFP. (B) Time-lapse microscopy of cells expressing GFP-Scs2 and mCherry-HDEL (ER) imaged every 10 minutes during meiosis. 0 min is defined as the time of ER collapse. (C) As in (B) but with cells expressing Pil1-antiGFP nanobody. (D) As in (B) but with cells expressing Rtn1-GFP instead of GFP-Scs2. (E) As in (D) but with cells expressing Pil1-mCherry. (F) Cells expressing GFP-HDEL (ER) and Htb1-mCherry treated with DMSO (vehicle) at 4.5 hr in meiosis and imaged every 10 min. 0 min is defined as the onset of anaphase II. (G) As in (F) but cells were treated with 200 uM LatA instead of vehicle. Scale bar = 2 μm for all panels.

We reasoned that forced tethering of a more abundant cortical ER protein may be necessary to prevent collapse, leading us to perform a similar approach to that described above, this time using the abundant reticulon protein Rtn1. Although forced tethering of Rtn1-GFP increased the overall amount of cortically retained ER, collapse was not prevented, as assessed by a substantial amount of mCherry-HDEL signal in the collapsed ER pool at anaphase II and a corresponding reduction in cortical mCherry-HDEL signal (figure 2.4D-E). These results support a model in which the cortical ER is prone to reticulon-dependent fragmentation during meiosis II, resulting in either collapse or cortical retention based on each ER fragment's local association (or lack of association) with ER-PM tethers. Thus, introduction of an abundant artificial tether increases the amount of ER that is cortically retained, but cannot prevent some amount of ER from dissociating from the plasma membrane.

2.3.8 The actin cytoskeleton promotes ER collapse

The abrupt, coordinated movement of cortical ER away from the plasma membrane suggests the involvement of a force-generating mechanism rather than passive diffusion. During mitosis in yeast, ER tubules are delivered into the daughter cell along actin cables (Estrada et al., 2003). To determine whether the actin cytoskeleton is also involved in meiotic ER dynamics, we treated cells undergoing meiosis with Latrunculin A (LatA), a drug that prevents actin polymerization. LatA-treated cells were still able to undergo ER cabling, but cabled structures failed to collapse, instead remaining cortical throughout chromosome segregation, suggesting that cabled ER is pulled away from the plasma membrane along actin filaments (figure 2.4F-G).

2.3.9 The ER undergoes turnover during meiosis

To determine if the dramatic ER remodeling that we observe in meiosis is accompanied by a fundamental change in the molecular composition of the ER, we analyzed the expression of all ER proteins over the course of meiosis using a previously published dataset with global matched measurements for protein abundance and translation levels (Brar et al., 2012; Cheng et al., 2018). Because cell number remains constant throughout meiosis, decreases in protein abundance over time indicate active degradation. We observed evidence for degradation for almost every ER-localized protein during mid- to late-meiosis in multiple waves, concomitant with or after ER collapse. Of the 658 proteins characterized for ER localization, we also observed robust synthesis (above 50 RPKM) for 81.3% of them, with this synthesis occurring late in meiosis (after ER collapse) for 85.2% of this set (figure 2.5A, 2.S3A). Together, these data suggest largescale turnover and resynthesis of many ER components during the meiotic program.

To independently assess the turnover of an abundant ER protein during meiosis, we used an assay that takes advantage of the diploid status of meiotic cells (Eisenberg et. al., 2018) by imaging cells with heterozygous tags marking the ER (*RTN1-GFP/RTN1*^{WT}) and nucleus (*HTB1-mCherry/HTB1*^{WT}). In this system, preexisting ER is marked by Rtn1-GFP, whereas newly synthesized ER following spore closure will either be marked or unmarked, depending on if the spore inherited *RTN1-GFP* or *RTN1*^{WT}, respectively. Similar GFP levels across all four spores would suggest no degradation or synthesis of Rtn1. A GFP signal increase in two spores would indicate Rtn1 resynthesis, while a GFP signal decrease in two spores indicates Rtn1 degradation. Consistent with our analysis of ER proteins globally, we saw two spores per tetrad retaining high levels of GFP signal, while GFP levels in the other two spores progressively declined, supporting a process of concerted ER degradation and resynthesis in late meiosis (figure 2.5B-E).

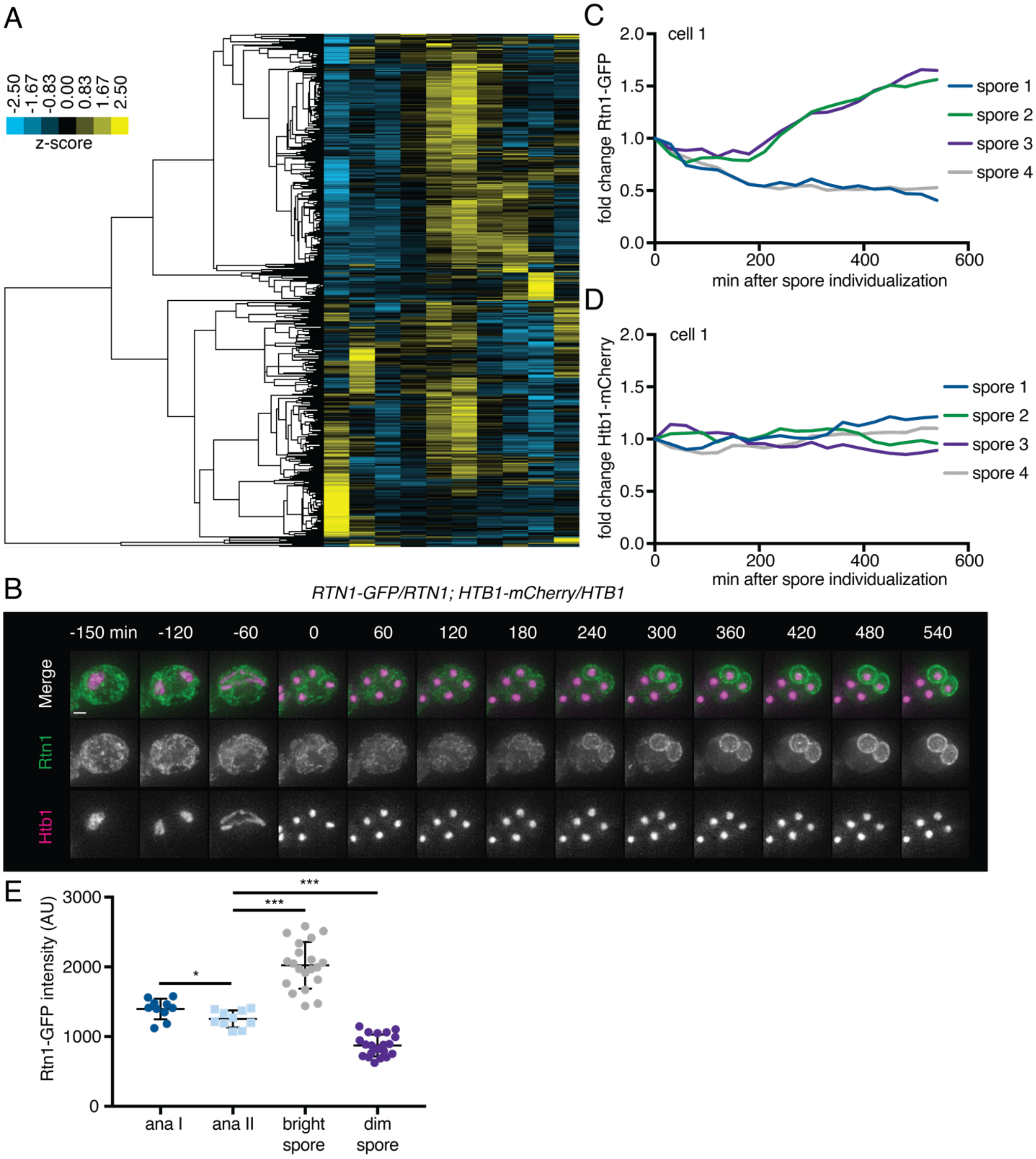

Figure 2.5. The ER undergoes turnover and resynthesis during meiosis. (A) Hierarchical clustering of z-score quantification of protein measurements published in Cheng *et. al.* (2018) for all quantified proteins annotated for ER localization. Each row represents one protein and each column is a timepoint in meiosis. (B) Time-lapse microscopy of cells heterozygous for Rtn1-GFP and Htb1-mCherry imaged every 30 minutes in meiosis. Time 0 is defined as the time of spore individualization. Scale bar = 2 μm. (C) Quantification of the average GFP signal for each spore for the cell in (B). (D) Quantification of the average mCherry signal for each spore for the cell in (B). (E) Quantification of the average GFP signal for ten cells at anaphase I, anaphase II, and the last imaged timepoint separated based on signal brightness (bright spore and dim spore).

2.3.10 The ER is degraded by autophagy during meiosis

What mechanisms mediate ER turnover during meiosis? One possibility was autophagy, in which cargo such as organelle fragments are engulfed by a double-membrane autophagosome and targeted to the vacuole (lysosome in metazoans) for degradation (Morishita and Mizushima, 2019). General autophagy factors are highly upregulated during meiosis and the kinase Atg1, which is essential for the initiation of autophagy, is also required for meiotic entry (Brar et. al., 2012; Wen et. al. 2016). Because GFP is resistant to vacuolar proteases while cargo proteins are not, GFP-tagged proteins that have been degraded by autophagy leave behind a GFP epitope that can be readily detected by western blot (Torggler et al., 2017). We tagged several ER resident proteins with GFP and observed the accumulation of a GFP-only band in meiosis, suggesting that the ER as a whole is a target of autophagy during this process (figure 2.6A, 2.S4A-C). A faint GFP fragment was visible as early as a few hours into meiosis, but the greatest accumulation occurred as cells progressed through anaphase II and beyond (figure 2.6A-B). As an orthogonal means of observing ER autophagy (ERphagy), we imaged cells expressing Rtn1-GFP and Vph1-mCherry, a marker of the vacuole membrane. Prior to meiosis, there was very little GFP within the vacuole, whereas cells in late meiosis displayed strong, diffuse GFP signal throughout the vacuole, providing further evidence that cells induce ERphagy as they progress through meiosis (figure 2.6C).

Atg1 is required for entry into meiosis, so we could not assess the role of the canonical Atg1-dependent autophagy pathway in meiotic ERphagy using *atg1Δ* cells. Instead, we conditionally depleted cells of Atg1 after meiotic entry using the auxin-inducible degron system, in which TIR1, a plant-derived ubiquitin ligase, targets degron-bearing substrates for proteasomal degradation only in the presence of the plant hormone auxin (Nishimura et al., 2009). By withholding auxin until after meiotic entry, we were able to deplete cells of degron-tagged Atg1 (Atg1-AID) without blocking meiosis. Both the accumulation of Rtn1-GFP in the vacuole as seen by microscopy and the appearance of GFP as a lone fragment by western blot in Rtn1-GFP cells were strongly reduced by depletion of Atg1, an effect that was stronger the earlier cells were treated with auxin (figure 2.6C-E). Thus, ERphagy in meiosis takes place through the canonical Atg1-dependent pathway.

We next sought to determine whether ERphagy is induced as part of the developmental program of meiosis or simply in response to sporulation media, which is nutrient-poor. Cells progressing through meiosis induced ERphagy much more strongly than cells arrested in prophase I (*ndt80Δ*) or prior to meiotic entry (*ime1Δ*), indicating that this process is enhanced by meiotic progression (figure 6F-H). Interestingly, ERphagy differs from other forms of autophagy in this respect. With the same experimental setup, we assessed general autophagy using GFP-Atg8 and mitochondrial autophagy (mitophagy) using OM45-GFP. Autophagy in general, and mitophagy in particular, are induced immediately upon introduction into sporulation media, even when cells are arrested prior to meiotic entry (figure 2.S4D-E). Together these results indicate that cells perform autophagy throughout meiosis, but prevent ERphagy until a later developmental stage. Because ERphagy has previously only been studied in the context of prolonged starvation or exposure to harsh chemical stress, it is intriguing to see its induction in a developmental context where external stressors are absent.

2.3.11 Meiotic ERphagy is mediated by selective autophagy receptors

Autophagy can occur either selectively or non-selectively. In selective autophagy, cargo-specific autophagy receptors recruit autophagosomes to their cargo via LC3-interacting region (LIR) motifs, ensuring precise target degradation (Anding and Baehrecke, 2017). Two budding yeast proteins, Atg39 and Atg40, have been identified as LIR motif-containing, ER-localized autophagy receptors (Mochida et. al., 2015). During nitrogen starvation and rapamycin treatment, Atg39 mediates the autophagic degradation of the perinuclear ER and some nuclear material, whereas Atg40 promotes autophagy of the cortical ER. The developmental specificity of ERphagy induction suggests that cells exert some degree of selectivity in defining meiotic autophagy targets. To further determine if ERphagy in meiosis takes place selectively, we examined cells lacking either or both ERphagy receptors. Cells lacking Atg40 progressed normally through meiosis but autophagy of the cortical ER marker Rtn1-GFP was almost completely blocked (figure 2.6I-K). Atg39 was dispensable for degradation of cortical ER markers but important for autophagy of Sec63, a member of the translocon complex that localizes throughout the cortical and perinuclear ER (figure 2.S4F-G). Thus, cells undergoing meiosis selectively target the ER for degradation via Atg39- and Atg40-mediated autophagy. Consistent with their roles in starvation-induced autophagy, these proteins specifically target the perinuclear and cortical ER, respectively, during meiotic differentiation.

We also noted that ERphagy affects the overall abundance of target proteins over time, as Rtn1-GFP accumulates to much higher levels at late timepoints in autophagy-deficient *atg39Δ atg40Δ* mutants compared to WT (figure 2.6L). These results suggest that the remodeling of the ER proteome in late meiosis seen in our mass spectrometry data is driven, at least in part, by selective ERphagy.

2.3.12 Atg40 expression is a developmental cue that triggers cortical ERphagy

ERphagy occurs primarily in late meiosis, downstream of the transcription factor Ndt80, but the precise developmental cues promoting ERphagy are still unclear (figure 2.6F-H). We examined Atg40 abundance during meiosis to determine if autophagy receptor expression itself might be the trigger for ER degradation. Atg40 was lowly expressed in vegetative cells and in early meiosis but was strongly induced in late meiosis, peaking in expression at around 6 hours before gradually declining (figure 2.6G, 2.S4H). This spike in Atg40 levels immediately preceded the autophagic degradation of Rtn1, indicating that developmentally regulated autophagy receptor expression precisely coincides with the induction of autophagy.

Do other cues feed into ERphagy induction, or is autophagy receptor expression the principal regulatory cue? We noted that *ime1Δ* cells arrested prior to meiotic entry or in prophase I show low Atg40 expression and exhibit very little ERphagy (figure 2.6G). To determine if providing cells with Atg40 in this context would be sufficient to induce ERphagy, we constructed a conditional allele of Atg40 using the copper-inducible *CUP1* promoter (*pCUP1-ATG40*). If Atg40 is the rate-limiting step for meiotic ERphagy, arrested cells should show Rtn1 degradation upon Atg40 induction. If additional developmental cues are required, Atg40 expression should be insufficient to trigger Rtn1 degradation. Consistent with the former model, copper-induced Atg40 expression resulted in robust autophagic degradation of Rtn1 during premeiotic arrest (figure 2.6M). In contrast, Atg40 overexpression in mitotic cells grown in rich media did not result in enhanced Rtn1 degradation. These results indicate that cells in sporulation media are primed for autophagy, and that the developmentally regulated expression of a single autophagy receptor is necessary and sufficient to trigger cargo degradation in this context.

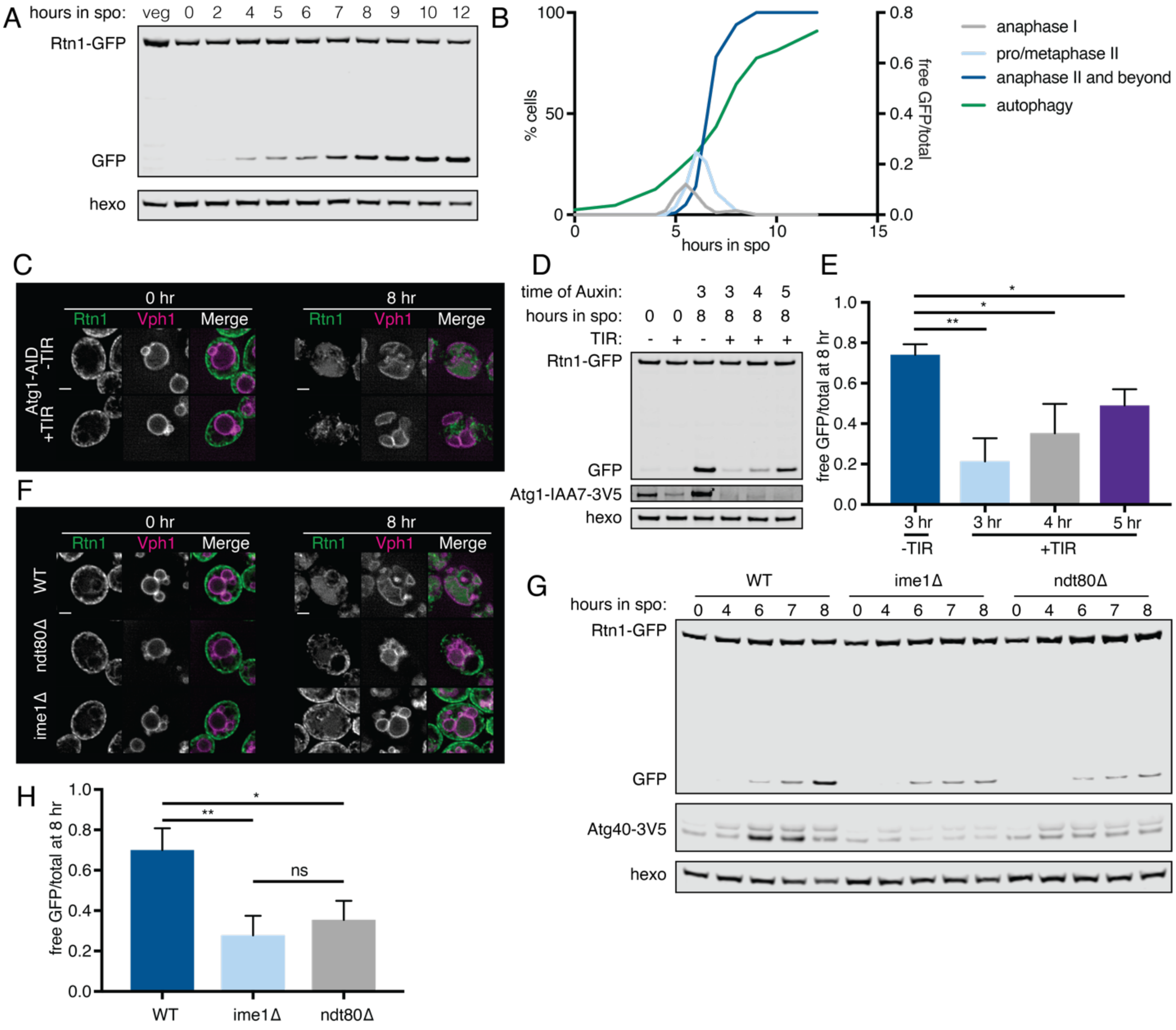

Figure 2.6 – continued on next page with figure legend

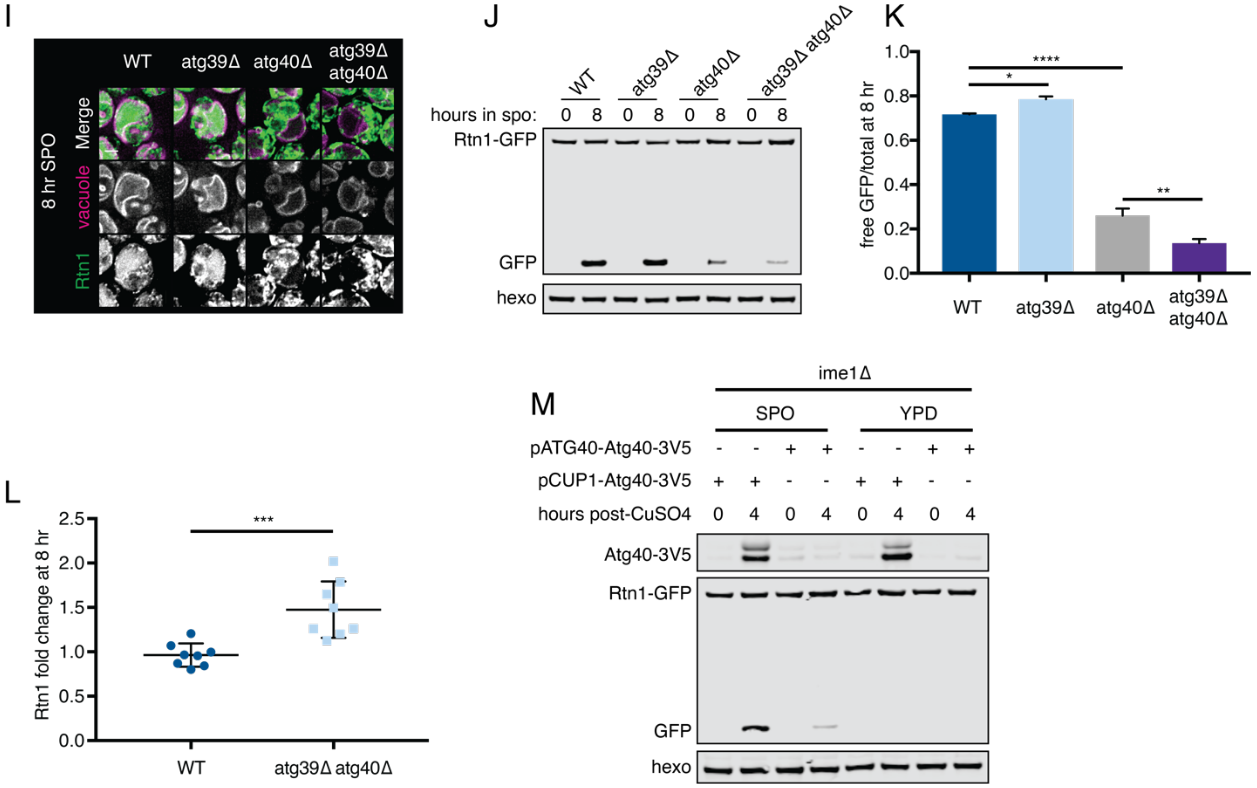

Figure 2.6. The ER is degraded by selective autophagy during meiosis. (A) Western blot with samples taken from cells expressing Rtn1-GFP during vegetative exponential growth (veg) or at the indicated time in meiosis probing for GFP and hexokinase (hexo) loading control. (B) Quantification of meiotic staging and autophagy using samples taken in parallel to those in (A). Left axis shows the % of cells at the indicated stage in meiosis and right axis shows the free GFP signal as a proportion of the total (Rtn1-GFP + free GFP). (C) Microscopy of cells expressing Rtn1-GFP, Vph1-mCherry, and Atg1-AID and imaged at the indicated times after transfer to SPO. Cells on the bottom also carry the osTIR allele. Cells were treated with 500 μM auxin after 4 hr in SPO. (D) Western blot of cells of the same genotypes as in (C) probing for GFP, V5 and hexo. Cells were treated with 500 μM auxin at the indicated times. Quantification of free GFP as a proportion of total GFP signal for three replicates of the experiment in (D). (F) Microscopy of cells of the indicated genotypes expressing Rtn1-GFP and Vph1-mCherry and imaged at the indicated times after transfer to SPO. (G) Western blot with samples taken from cells of the same genotypes as in (F) at the indicated times after transfer to spo, probed for GFP and hexo. (H) Quantification of free GFP as a proportion of total GFP signal for three replicates of the experiment in (G). (I) Microscopy of cells of the indicated genotypes expressing Rtn1-GFP and Vph1-mCherry and imaged at 8 hr after transfer to SPO. (J) Western blot with samples taken from cells of the indicated genotypes expressing Rtn1-GFP following transfer to spo. Probed for GFP and hexokinase. (K) Quantification of free GFP as a proportion of total GFP signal at 8hr following transfer to SPO for three replicates of the experiment in (J). (L) Quantification of Rtn1-GFP signal at 8 hr following transfer to SPO normalized to hexokinase loading control and to 0 hr measurement for eight replicates of the experiment in (J). (M) Western blot with samples taken from ime1Δ cells expressing Rtn1-GFP and Atg40-3V5 under the endogenous promoter (*pATG40-ATG40-3V5*) or the *CUP1* promoter (*pCUP1-ATG40-3V5*). For YPD samples, cells were diluted to 0.05 ODU in YPD, allowed to grow to exponential phase, treated with50 μM $CuSO_4$. For SPO samples, cells were transferred to SPO for 2 hours and treated with 50 μM $CuSO_4$. Protein samples were taken at the indicated times after $CuSO_4$ treatment. Scale bar = 2 μm for all microscopy panels.

2.3.13 ER collapse is required for ERphagy

We noted that mutants with increased cortical ER retention in meiosis, namely *lnp1Δ* and *rnt1Δ rtn2Δ yop1Δ* cells*,* are also reported to be deficient in starvation-induced ERphagy (Chen et al., 2018). It is worth noting that the converse is not true, as autophagy-deficient (*atg40Δ)* mutants display normal ER collapse (figure 2.S5A). We confirmed that *lnp1Δ* and *rtn1Δ rtn2Δ* *yop1Δ* mutant cells showed reduced ERphagy in the context of meiosis, which led us to investigate whether ER collapse is important for autophagic degradation in meiosis (figure 2.7A-B). One prediction of this model is that cortically retained ER is not subject to autophagy. Indeed, we saw very little autophagic degradation of the cortically retained tethers GFP-Ist2 and Tcb3-GFP relative to GFP-Scs2, an ER-PM tether that is not cortically retained, or Rtn1-GFP, a non-tether control (figure 2.7C).

If meiotic ERphagy depends on ER collapse, engineered targeting of a protein that is normally abundant in collapsed ER to the retained cortical ER compartment should no longer be subject to ERphagy. Ectopically targeting Rtn1-GFP to the cortically retained ER compartment using Pil1-nanobody abolished autophagic degradation of Rtn1-GFP, supporting a model in which collapsed ER is robustly targeted by autophagy while cortically retained ER is not (figure 2.7C-D). This result establishes a key link between the dramatic morphological changes in the ER during meiosis and its regulated degradation.

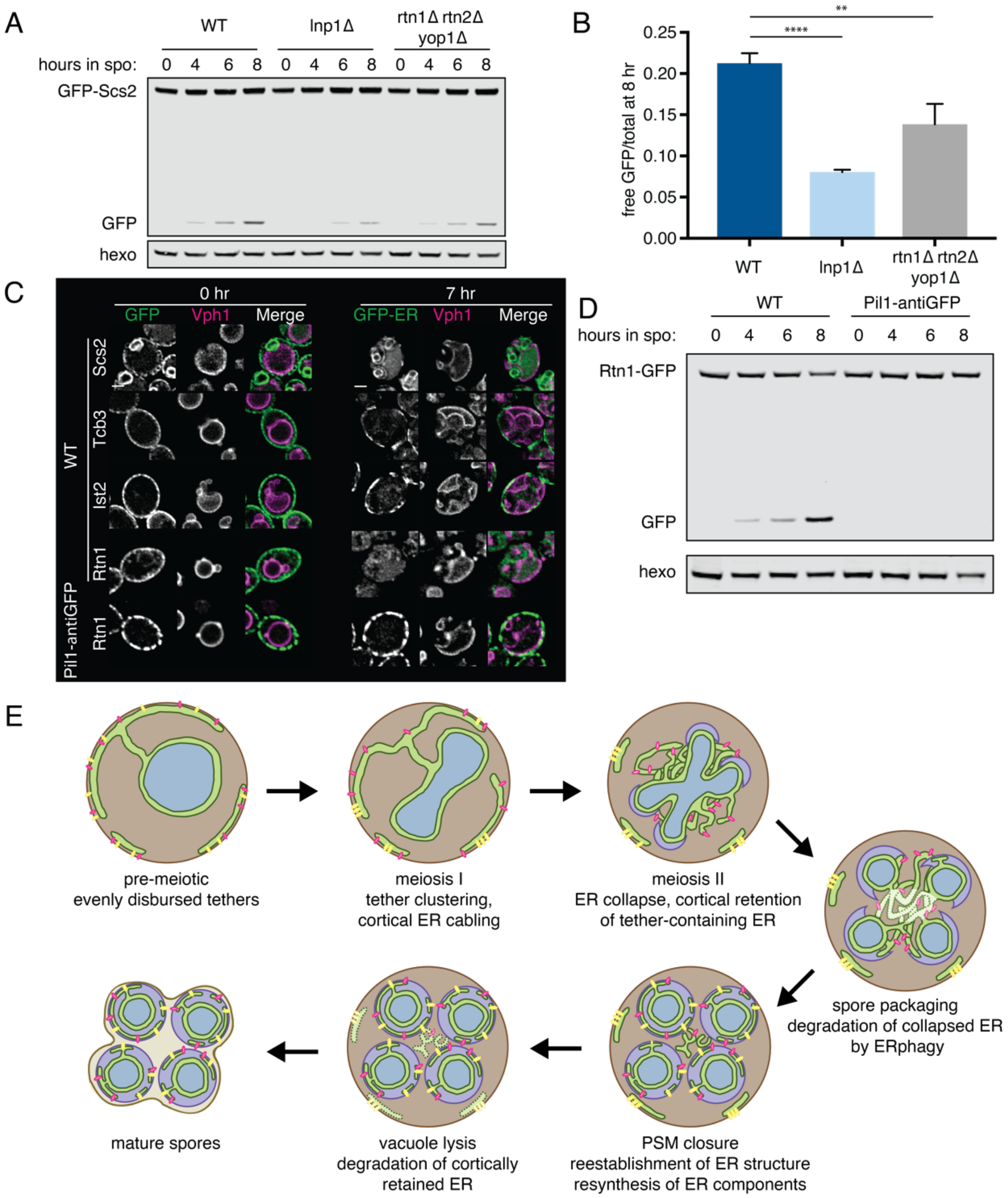

Figure 2.7. ER collapse is required for ERphagy. (A) Western blot with samples taken from cells of the indicated genotypes expressing GFP-Scs2 and Atg40-3V5 at the indicated times after transfer to SPO and probed for GFP, V5 and hexo. (B) Quantification of free GFP as a proportion of total GFP signal at 8 hours after transfer to SPO, using three replicates of the experiment from (A). (C) Microscopy images of cells expressing Vph1-mCherry and the indicated GFP-tagged ER protein and either an untagged (WT) or anti-GFP nanobody-tagged allele of Pil1 (Pil1-antiGFP). Images were taken at 0 and 7 hr following transfer to SPO. Scale bar = 2 μm. (D) Western blot with samples taken from cells expressing Rtn1-GFP and either WT Pil1 or Pil1-antiGFP. Samples were taken at the indicated times following transfer to SPO and probed for GFP and hexo. (E) Schematic showing key steps in meiotic ER remodeling.

2.4 Discussion

In this study, we investigated the extensive ER remodeling that occurs in the natural developmental context of budding yeast meiosis (figure 2.7E). We observed a series of dramatic changes in ER morphology and identified a set of surprising mechanisms that together support an integrated model of programmed meiotic ER remodeling. Early in meiosis, the cortical ER undergoes cabling and ER-PM tethers begin to cluster together. Next, coincident with anaphase II, most cortical ER collapses away from the plasma membrane, while a subset of ER islands colocalize with ER-PM tethers and remain at the cell cortex. Cortical ER collapse relies on reticulon-dependent membrane scission, the proposed inhibitor of ER membrane fusion Lnp1, and the actin cytoskeleton. Structural remodeling of the ER is accompanied by large-scale degradation of a subset via selective autophagy, prior to ER partitioning into gametes. After gamete membrane closure, cortically retained ER is degraded by vacuolar proteases following vacuole lysis. Thus, our work shows that developmentally regulated ER compartmentalization, membrane tethering, and two parallel pathways for ER degradation combine to broadly mediate ER inheritance by gametes while selectively eliminating a subset of ER. These findings illuminate several important new areas of inquiry into developmental ER remodeling and quality control.

An especially unexpected finding presented here is the apparent role of cortical ER fragmentation in meiotic ER inheritance. The ER is defined as being a continuous organelle, but the cortically retained islands of ER must be physically separate from collapsed ER, as they are excluded from inheritance into spores by continuous membranes that surround these maturing gametes. Although this type of programmed ER fragmentation has not, to our knowledge, been described during differentiation, it enables an effective strategy for meiotic ER collapse. Without the ability of meiotic cells to physically separate cortical ER subdomains, degradation or inhibition of ER-PM tethers would be required to release cortical ER from the plasma membrane. Our microscopy experiments refute this model, however, as four canonical tethers remain highly expressed and cortically localized throughout meiosis. Instead, our data are consistent with a model in which the ER undergoes a developmental transition from one continuous membrane system to separate, fragmented topologies, with the fate of each fragment determined by whether or not it contains ER-PM tethers. Consistently, we find that artificial cortical tethering of an abundant tubular ER protein, Rtn1, increases cortical ER retention but does not prevent separation of regions of ER without Rtn1 to a collapsed pool in meiosis. Therefore, ER fragmentation elegantly achieves two distinct outcomes at once, allowing cortical ER inheritance while partitioning specific ER fragments away from gametes.

In support of a model in which ER fragmentation contributes to the detachment of cortical ER in meiosis, normal programmed meiotic collapse of most cortical ER relies on the reticulon proteins Rtn1 and Rtn2, and the reticulon-like protein Yop1. This class of proteins was initially identified for their role in structuring ER membranes via the conserved reticulon homology domain (RHD), a wedge-like intramembrane domain that increases surface area in the cytosolic leaflet of the ER membrane, thereby generating positive membrane curvature and promoting tubule formation (Voeltz et. al., 2006; Hu et. al., 2008). More recently, studies have shown that reticulon overexpression causes ER fragmentation in flies, mammalian cells, and *in vitro* reconstituted ER, suggesting that reticulons promote membrane scission, at least at high concentrations (Wang et. al., 2016; Powers et. al., 2017; Espadas et. al., 2019). These studies, together with our findings, suggest that reticulons drive cortical ER fragmentation and subsequent cortical detachment during meiosis. This raises the important question of how reticulon-mediated membrane scission is regulated to allow precisely timed ER collapse. It seems unlikely that reticulon expression levels alone would be sufficient to drive this process, as Rtn1, Rtn2 and Yop1 abundance are static from early meiosis through ER collapse (Figure 6A; Brar et. al., 2012; data not shown). One example of conditional reticulon-driven ER fragmentation is in the context of ERphagy. Many ERphagy receptors, including Atg40 and the human proteins FAM134B and Rtn3, contain a reticulon homology domain that is important for delivery of ER fragments into autophagosomes via membrane fission (Mochida et. al., 2020; Grumati et. al. 2017; Bhaskara et. al., 2019; Jiang et. al., 2020). In these cases, autophagy receptors oligomerize to produce a high local concentration of RHD proteins, thus driving membrane fission locally without affecting global ER structure. In the case of FAM134B, oligomerization is enhanced by phosphorylation of serine residues within the RHD (Jiang et. al., 2020). Our finding that yeast reticulons are involved in meiotic ER collapse and inheritance further highlights that these proteins are more than inert structural proteins, and instead can serve important roles in dynamic ER remodeling. It will be important to determine the developmental cues regulating reticulon-dependent membrane scission in meiosis, and whether coordinated reticulon oligomerization drives this phenomenon.

Morphological homeostasis of the tubular ER network requires a balance between membrane fusion and fission. Our data support a model in which this balance shifts toward fission in meiotic cells, resulting in fragmented ER. Consistent with a need for reduced tubule fusion in this process, we found that Lnp1, which has been proposed as a negative regulator of Sey1-mediated tubule fusion (Chen et. al., 2012), is important for ER collapse in meiosis. Cells lacking Lnp1 formed massive ER foci that remained attached to the cell cortex throughout meiosis. How these structures form and their precise composition are still unclear, though the decrease in focus size and abundance in *lnp1Δ sey1Δ* double mutant cells suggests that they are the result of excessive membrane fusion in the absence of Lnp1. These structures are not present in *lnp1Δ* cells undergoing exponential mitotic growth, though we did observe them in saturated *lnp1Δ* cultures (data not shown), suggesting an unexpected role for Lnp1-dependent ER remodeling during nutrient adaptation. Further elucidation of the function of Lnp1 in these conditions may provide crucial insight into the role of this conserved yet poorly understood family of proteins.

What is the purpose of excluding certain parts of the ER from inheritance by gametes? One possibility is that this process serves as a form of ER quality control, selectively preventing the inheritance of damaged or toxic ER or ER-associated material. Targeting deleterious ER contents to the cortically retained compartment would be an efficient means of ensuring their physical exclusion from gametes. An important challenge with such a system would be achieving specificity in what is targeted to cortically retained ER. Thus far, the only proteins that we identified to preferentially localize to the cortically retained compartments are ER-PM tethers themselves. It will be important to determine in future studies whether other ER proteins or cellular components selectively localize to this compartment, and the role that ER-PM tethers play in this process.

The most widely studied substrates for ER quality control are misfolded proteins, which are induced by genetic or chemical disruption of ER protein folding capacity, or through exogenous expression of model aggregate-prone proteins. During mitosis in budding yeast, misfolded ER proteins are retained in mother cells, promoting daughter cell rejuvenation at the expense of reduced mother cell lifespan (Clay et. al., 2014; Piña and Niwa, 2015). Intriguingly, while the vast majority of ER components enter into the daughter cell during mitotic ER inheritance in the absence of ER stress, all four cortically retained tethers are tightly restricted to the mother cell (Takizawa et. al., 2000; Okada et. al., 2017; Sugiyama and Tanaka, 2019). Moreover, asymmetric inheritance of both misfolded proteins and ER-PM tethers relies on an ER membrane diffusion barrier established by septin ring components at the bud neck (Clay et. al., 2014; Sugiyama and Tanaka, 2019), suggesting a shared mechanism to control the selective inheritance of ER protein aggregates and ER-PM tethers, and raising the possibility that ER-PM tethers themselves may be markers of age-induced ER stress. A conserved but understudied feature of gametogensis is the elimination of age-induced damage to produce healthy, youthful gametes (Goodman et. al., 2020). In budding yeast, a variety of abnormal structures, including cytosolic protein aggregates, extrachromosomal rDNA circles, and expanded nucleoli, accumulate with age and are retained by mother cells during cell division (Shcheprova et. al., 2008). During gamete formation, most of these structures are excluded from gamete cells and eliminated, likely contributing to gamete rejuvenation (Ünal et. al., 2011; King et. al., 2019). While naturally occurring markers of age-induced ER damage have not been described in yeast, there are clear parallels between the cortically retained ER compartment and these established hallmarks of aging. Our work motivates further study of relationship between ER stress, aging, and cortical ER inheritance in meiosis and mitosis.

Deletion of the four previously identified ER-PM tethers (Ist2 and the tricalbins Tcb1, Tcb2 and Tcb3) that mark cortically retained ER fragments reduces the amount of cortically retained ER at anaphase II, but does not completely prevent ER retention, suggesting that additional tethers and/or alternative mechanisms ensure cortical ER tethering in this context. While Scs2 and Scs22 are normally released from the plasma membrane during meiosis, they may contribute to cortical ER retention in the absence of the other four tethers. However, deletion of all six tethers together eliminates almost all cortical ER even in non-meiotic cells, complicating our ability to assess meiotic cortical ER retention in this genotype. Additional proteins beyond these six tethers have been observed to localize to ER-PM contact sites, and some have been proposed as additional ER-PM tethering proteins (Petkovic et. al., 2014; Topolska et. al., 2020). Study of these additional factors will be important to further interrogate the molecular basis of cortical ER retention during meiosis and its role in ensuring gamete health.

In addition to the exclusion of cortically retained ER from gametes, we identified programmed selective autophagy as a parallel, mutually exclusive means of eliminating ER subdomains during meiosis. Whereas ERphagy has previously only been studied in the context of nutrient limitation or ER stress in the presence of harsh chemical treatment, our identification of its natural role in meiosis provides an opportunity to study its endogenous regulation in a developmental context. We identified the timed expression of the ER-specific autophagy receptor Atg40 as a key developmental cue regulating ERphagy. Atg40 expression occurs downstream of the meiotic transcription factor Ndt80. Our findings warrant a more detailed study of how its expression and activity are regulated, and the role of ERphagy in the broader developmental context of meiosis.

As with cortical ER retention, it is appealing to hypothesize that ERphagy serves as a meiotic quality control mechanism. The autophagy receptors Atg39 and Atg40 are selective for perinuclear and cortical ER, respectively, during starvation-induced and meiotic ERphagy. However, whether there is any additional specificity to which ER components are degraded in any context is yet to be determined. ERphagy receptors in mammalian cells have been shown to preferentially degrade subsets of the ER proteome, including misfolded proinsulin and procollagen aggregates, but the molecular basis for this specificity is largely unknown (Forrester et. al., 2018; An et. al., 2019; Cunningham et. al., 2019). In the future, understanding how cells precisely target cargo for degradation by ERphagy to remodel the ER and mitigate ER stress will be crucial for defining the role of ERphagy meiosis. Moreover, owing to the conservation of ERphagy factors in mammals, we propose that the natural role of ERphagy in meiotic development suggests a more widespread role for this newly uncovered process in mammalian cellular development programs.

2.5 Methods

2.5.1 Yeast strains, plasmids, and primers

All experimental strains are diploid *Saccharomyces cerevisiae* derivatives of the SK1 strain as detailed in Table 2.1. The following alleles were derived from previous studies: *pGAL-NDT80* and *GAL4.ER* (Benjamin et. al., 2003; Carlile and Amon, 2008), *pCLB2-CDC20* (Lee and Amon, 2003), *pCUP1-oSTIR* (Sawyer et. al., 2019), *mKate-SPO20*$_{51-91}$ and *VPH1-mCherry* (King et. al., 2019), *HTB1-mCherry* (Matos et al., 2008), *ndt80Δ* (Xu et al., 1995), *GFP-ATG8* (Graef et al., 2013). The *atg8::LEU2* allele was a gift from Hilla Weidberg and Angelika Amon.

Deletion and C-terminal tagging of genes at their endogenous loci were performed using an established PCR-based technique (Janke et al., 2004; Longtine et al., 1998)using the primers indicated in Table 2.2 and plasmids indicated in Table 2.3. *GFP-SCS2* and *GFP-IST2* were created using the Cas9-based method described in Sawyer et. al. (2019) using guide RNAs detailed in Table 2. The repair template containing GFP and a linker sequence was amplified from pÜB1548. GFP-Scs22 expressed from its endogenous locus was not detectable by microscopy in our strain background (not shown), so we generated an allele that is highly expressed in meiosis (*pATG8-GFP-SCS22*). *SCS22* was amplified from SK1 genomic DNA and cloned into pÜB 1548 by Gibson assembly (Gibson et al., 2009), replacing the *ATG8* ORF. The *SCS22* intron was removed following the Q5 Site-Directed Mutagenesis protocol (New England Biolabs) to generate pÜB1889. This plasmid was digested with PstI and transformed into WT SK1. To generate *pCUP1-ATG40-3V5*, *ATG40-3V5* was amplified from yeast harboring that allele and cloned together with the *CUP1* promoter into the pÜB217 plasmid by Gibson assembly. The resulting plasmid was amplified with the primers indicated in Table 2.2 and transformed into a strain harboring *atg40::KanMX*, replacing the KanMX cassette to give *atg40::pCUP1-ATG40-3V5-HygB*. To construct a *GFP-HDEL* construct that is stably expressed throughout meiosis, the *GFP-HDEL* sequence published in Rossanese et al. (2001)was cloned into a *TRP1* integrating vector harboring the *ARO10* promoter, obtained from Leon Chan. The resulting *pARO10-GFP-HDEL-TRP1* construct was used to generate *pARO10-mCherry-HDEL* by Gibson assembly. Both constructs were transformed into yeast following digestion with PmeI.

2.5.2 Media and growth conditions

Prior to the induction of meiosis, cells were grown at room temperature for 20-24 hr to a density of $OD_{600} \geq 10$ in YEPD (1% yeast extract, 2% peptone, 2% glucose, 22.4 mg/L uracil, 80 mg/L tryptophan). Cultures were then diluted to $OD_{600} = 0.25$ in BYTA (1% yeast extract, 2% bacto tryptone, 1% potassium acetate, and 50 mM potassium phthalate) and grown for 16-18 ($OD_{600} \geq 4.5$) hr at 30° C. Cells were then pelleted, washed with sterile MilliQ water and resuspended to $OD_{600} = 1.9$ in sporulation medium (SPO; 2% potassium acetate, 40 mg/L adenine, 40 mg/L uracil, 10 mg/L histidine, 10 mg/L leucine and 10 mg/L tryptophan adjusted to pH 7.0 and supplemented with 0.02% raffinose). Cultures were allowed to shake at 30° C for the duration of the experiment. For each stage, culture volume was 1/10th of the flask volume to ensure proper aeration.

For experiments conducted during vegetative growth, cells were grown in YEPD for 16-18 hours at 30° C ($OD_{600} \geq 10$). Cultures were then back-diluted to $OD_{600} = 0.02$-0.05. For imaging experiments, cells were examined at a density of $OD_{600} = 0.6$-0.8. For copper-inducible expression experiments, $CuSO_4$ or an equivalent volume of water (vehicle) was added to a final concentration of 50 μM when cells were at a density of $OD_{600} = 0.2$. For estrogen-inducible expression experiments, β-estradiol or an equivalent volume of 100% EtOH was added to a final concentration of 1 μM.

2.5.3 Live-cell imaging

Live-cell imaging was performed exactly as described in King et. al. (2019), except fresh SPO was used in place of conditioned spo. Specific imaging conditions are noted in Supplementary Table 2.4. All time-lapse experiments were performed using the CellAsic system (EMD Millipore) in Y04D or Y04E microfluidics plates, with the exception of the Latrunculin A experiments, for which we used glass-bottom 96-well plates (Corning).

2.5.4 Image quantification

In time-lapse microscopy, anaphase I was defined as the first frame in which an elongated nucleus was observed (if applicable), or the first frame at which two distinct nuclear masses were visible. Anaphase II was defined as the first frame at which two elongated nuclei were observed following anaphase I. ER cabling was defined as the first frame at which ER cables were visible ER cables are bright, cortically localized ER structures that are thicker and more dynamic than pre-meiotic cortical ER. ER collapse was defined as an abrupt movement of cortical ER toward the center of cells. Prospore membrane nucleation was defined as the first frame at which mKate-$Spo20_{51\text{-}91}$ signal was visible as distinct puncta in the center of cells rather than plasma membrane-localized. Prospore membrane closure was defined as the frame at which membrane structure transitioned from elongated to circular. Vacuole lysis was defined as the time at which signal became diffuse rather than membrane-localized. Degradation of GFP-Ist2 and Tcb3-GFP was defined as the frame at which their signal disappeared from the cell cortex.

Qualitative cortical ER classification was performed at anaphase II according to the guidelines outlined in figure 2D. Class III ER ("intermediate") includes cells that had either a mixture of small fragments and large spans of cortical ER AND/OR fragments that were intermediate in size and therefore not categorized as small fragments or large spans.

For Gini index calculation, the cell periphery was traced for the centermost Z-slice using the program Fiji. Pixel intensity was calculated along the length of the trace, resulting in a finite number of measurements "n". These measurements were then ordered from smallest to largest and given an integer ranking "i" based on this order (i.e. for each value 1 ≤ i ≤ n, where the smallest number in the dataset has i=1 and the highest number has i=n). Background was subtracted using average pixel intensity from a cell-free region of the image. The Gini index (G) was determined using the formula:

$$G = \frac{2}{\overline{x}n^2}\sum_{i=1}^{n} i(x_i - \overline{x})$$

"$\overline{x}$" is the average of all measurements and x_i is the intensity value of ranking "i" in the dataset. For each cell (n=10), Gini values were calculated for at least seven timepoints prior to ER collapse and six timepoints following ER collapse.

For analysis of foci in lnp1Δ cells, foci were counted manually for at least 100 cells per genotype. Focus size was measured using Fiji. Briefly, images were z-projected using maximum intensity projection, converted to 8-bit, and threshold was adjusted so that foci were clearly visible. Foci were detected automatically using the "analyze particles function, resulting in measurements for at least 134 foci across over 100 cells per genotype.

For measurements of Rtn1 and Htb1 abundance in heterozygously tagged cells, images were maximum projected over the full imaging volume in Fiji. Tracing was performed for the whole cell (anaphase I and anaphase timepoints) or for individual spores, and average pixel intensity for the traced area was calculated for both channels. Measurements for the cells shown in figure 5C-F were obtained from the first frame at which individual spores were easily distinguishable until spores became tightly packed and therefore had significantly overlapping signal (at least 480 min). Bright spore and dim spore images in figure 5G were taken from the last timepoint at which spores did not significantly overlap.

2.5.5 Meiotic staging

Meiotic staging was performed scoring DAPI and tubulin morphology by fluorescent microscopy as described in Sawyer et. al. (2019). Samples were fixed in 3.7% formaldehyde for 12-24 hr at 4° C. Cells were then washed with 100 mM potassium phosphate pH6.4, once with sorbitol citrate (100 mM potassium phosphate pH7.5, 1.2 M sorbitol), and digested in 200 µL sorbitol citrate, 20 μL glusulase (Perkin-Elmer) and 6 μL of zymolase (10 mg/mL, MP Biomedicals) for 3 hours at 30° C while rotating. Samples were pelleted at 900 rcf for 2 min, washed with 100 μL sorbitol citrate, pelleted again and resuspended in 50 μL sorbitol citrate. Samples were then mounted on slides prepared with poly-L-lysine, submerged in 100% methanol at -20° C for 3 min, transferred to 100% acetone at -20° C for 10 sec, then allowed to air dry. Samples were then incubated at RT for 1 hr in primary anti-tubulin antibody (Bio-Rad, 1:200) in PBS-BSA (5 mM potassium phosphate, 15 mM NaCl, 1% BSA, 0.1% sodium azide). Samples were then washed 3x in PBS-BSA and incubated with preabsorbed FITC-conjugated secondary antibody (Jackson ImmunoResearch Labs, 6:200) for 1 hr at RT. Samples were washed 3x with PBS-BSA and mounted with VectaShield Antifade Mounting Medium with DAPI (Vector Labs).

2.5.6 Western blotting

Protein samples were extracted by trichloroacetic acid (TCA) precipitation as described previously (Chen et. al., 2017), with some modifications. For meiotic samples, 1.8 mL culture was mixed with 200 μL 50% TCA (5% final concentration) and incubated at 4° C for 12-24 hr. For vegetative mitotic samples, 3.42 ODU culture was spun down for 2 min at 3000 rcf, washed in sterile MilliQ water, resuspended in 5% TCA and incubated at 4° C for 12-24 hr. All samples were precipitated for 5 min at 20,000 rcf and washed in 1 mL acetone. The acetone was aspirated and samples were allowed to dry for at least 20 minutes. Pellets were resuspended by bead beating for 5 min in 100 μL TE supplemented with 3 mM and 1x protease inhibitors (Roche) with 100 μL acid-washed glass beads. 50 μL 3x SDS loading buffer was added and samples were incubated at 95° C for 5 minutes and spun down for 5 min at 20,000 rcf. 4 μL were loaded onto a Bis-Tris acrylamide gel, separated at 150 V for 50 minutes and transferred to a nitrocellulose membrane using the TransBlot Turbo system (BioRad). Blots were blocked and probed overnight at 4° C with one or more of the following antibodies: anti-hexokinase (US Biological, 1:15,000), anti-GFP JL8 (Clontech, 1:2000), anti-V5 (Invitrogen, 1:2000). Blots were washed in PBST and incubated for 2 hr in IRDye secondary antibodies (LI-COR, 1:20,000). Blots were imaged and quantified using the Odyssey system (LI-COR).

2.6 Supplementary Tables

Table 2.1 – Strains used in this study

BrÜn strain #	genotype
3095	*MATa/alpha, sec63::SEC63-eGFP-KanMX/sec63::SEC63-eGFP-KanMX*
3286	*MATa/alpha, om45::OM45-eGFP-KanMX/om45::OM45-eGFP-KanMX*
6329	*MATa/alpha, sec63::SEC63-eGFP-KanMX/sec63::SEC63-eGFP-KanMX, atg40::KanMX/atg40::KanMX*
7369	*MATa/alpha, rtn1::RTN1-eGFP-KanMX/RTN1, htb1::HTB1-mCherry-HISMX6/HTB1*
7540	*MATa/alpha, trp1::pARO10-GFP-HDEL-TRP1/trp1::pARO10-GFP-HDEL-TRP1, htb1::HTB1-mCherry-HISMX6/htb1::HTB1-mCherry-HISMX6*
7828	*MATa/alpha, rtn1::RTN1-eGFP-KanMX/rtn1::RTN1-eGFP-KanMX, HTB1-mCherry-HISMX6/HTB1-mCherry-HISMX6*
7958	*MATa/alpha, trp1::pARO10-GFP-HDEL-TRP1/trp1::pARO10-GFP-HDEL-TRP1, htb1::HTB1-mCherry-HISMX6,htb1::HTB1-mCherry-HISMX6. rtn1::KanMX/rtn1::KanMX, rtn2::NatMX/rtn2::NatMX, yop1::KanMX/yop1::KanMX*

8070	*MATa/alpha, rtn1::RTN1-eGFP-KanMX/rtn1::RTN1-eGFP-KanMX, HTB1-mCherry-HISMX6/HTB1-mCherry-HISMX6, lnp1::NatMX/lnp1::NatMX*
8270	*MATa/alpha, ura3::GFP-ATG8-URA3/ura3::GFP-ATG8-URA3, atg8::TRP1/atg8::TRP1*
9021	*MATa/alpha, sey1::SEY1-eGFP-KanMX/sey1::SEY1-eGFP-KanMX*
9591	*MATa/alpha, trp1::pARO10-GFP-HDEL-TRP1/trp1::pARO10-GFP-HDEL-TRP1, htb1::HTB1-mCherry-HISMX6,htb1::HTB1-mCherry-HISMX6, cdc20::pCLB2-CDC20-KanMX/cdc20::pCLB2-CDC20-KanMX*
9825	*MATa/alpha, trp1::pARO10-GFP-HDEL-TRP1/trp1::pARO10-GFP-HDEL-TRP1, htb1::HTB1-mCherry-HISMX6/htb1::HTB1-mCherry-HISMX6, trp1::GAL-NDT80-TRP1/trp1::GAL-NDT80-TRP1, ura3::pGPD1-GAL4(848).ER-URA3/ura3::pGPD1-GAL4(848).ER-URA3*
10517	*MATa/alpha, trp1::pARO10-GFP-HDEL-TRP1/trp1::pARO10-GFP-HDEL-TRP1, htb1::HTB1-mCherry-HISMX6/htb1::HTB1-mCherry-HISMX6, atg40::KanMX/atg40::KanMX*
10723	*MATa/alpha, trp1::pARO10-GFP-HDEL-TRP1/trp1::pARO10-GFP-HDEL-TRP1, htb1::HTB1-mCherry-HISMX6/htb1::HTB1-mCherry-HISMX6, sey1::NatMX/sey1::NatMX*
10758	*MATa/alpha, trp1::pARO10-GFP-HDEL-TRP1/trp1::pARO10-GFP-HDEL-TRP1, htb1::HTB1-mCherry-HISMX6/htb1::HTB1-mCherry-HISMX6, rtn1::KanMX/rtn1::KanMX, rtn2::NatMX/rtn2::NatMX, lnp1::NatMX/lnp1::NatMX yop1::KanMX/yop1::KanMX*
11037	*MATa/alpha, trp1::pARO10-GFP-HDEL-TRP1/trp1::pARO10-GFP-HDEL-TRP1, htb1::HTB1-mCherry-HISMX6/htb1::HTB1-mCherry-HISMX6, sey1::NatMX/sey1::NatMX, lnp1::NatMX/lnp1::NatMX*
11132	*MATa/alpha, sec63::SEC63-eGFP-KanMX/sec63::SEC63-eGFP-KanMX, atg39::NatMX/atg39::NatMX, atg40::KanMX/atg40::KanMX*
11185	*MATa/alpha, trp1::pARO10-GFP-HDEL-TRP1/trp1::pARO10-GFP-HDEL-TRP1, htb1::HTB1-mCherry-HISMX6/htb1::HTB1-mCherry-HISMX6, lnp1::NatMX/lnp1::NatMX*
11696	*MATa/alpha, sec63::SEC63-eGFP-KanMX/sec63::SEC63-eGFP-KanMX, atg39::NatMX/atg39::NatMX*
11873	*MATa/alpha, sec63::SEC63-eGFP-KanMX/sec63::SEC63-eGFP-KanMX, htb1::HTB1-mCherry-HISMX6/htb1::HTB1-mCherry-HISMX6*
11906	*MATa/alpha, trp1::pARO10-GFP-HDEL-TRP1/trp1::pARO10-GFP-HDEL-TRP1, tcb3::TCB3-mKate-URA3/tcb3::TCB3-mKate-URA3*
13389	*MATa/alpha, trp1::pARO10-GFP-HDEL-TRP1/trp1::pARO10-GFP-HDEL-TRP1, leu2::pATG8-mKate-SPO20(51-91)-LEU2/leu2::pATG8-mKate-SPO20(51-91)-LEU2*
13527	*MATa/alpha, sec63::SEC63-eGFP-KanMX/sec63::SEC63-eGFP-KanMX, htb1::HTB1-mCherry-HISMX6/htb1::HTB1-mCherry-HISMX6, lnp1::NatMX/lnp1::NatMX*
16551	*MATa/alpha, rtn1::RTN1-eGFP-KanMX/rtn1::RTN1-eGFP-KanMX, atg40::ATG40-3V5-KanMX/atg40::ATG40-3V5-KanMX, ndt80::LEU2/ndt80::LEU2*
16552	*MATa/alpha, rtn1::RTN1-eGFP-KanMX/rtn1::RTN1-eGFP-KanMX, atg40::ATG40-3V5-KanMX/atg40::ATG40-3V5-KanMX, ime1::HygB/ime1::HygB*
18680	*MATa/alpha, tcb1::TCB1-eGFP-KanMX/tcb1::TCB1-eGFP-KanMX, htb1::HTB1-mCherry-HISMX6/htb1::HTB1-mCherry-HISMX6*
18681	*MATa/alpha, tcb2::TCB2-eGFP-KanMX/tcb2::TCB2-eGFP-KanMX, htb1::HTB1-mCherry-HISMX6/htb1::HTB1-mCherry-HISMX6*
18682	*MATa/alpha, tcb3::TCB3-eGFP-KanMX/tcb3::TCB3-eGFP-KanMX, htb1::HTB1-mCherry-HISMX6/htb1::HTB1-mCherry-HISMX6*
19479	*MATa/alpha, GFP-SCS2/GFP-SCS2, atg40::ATG40-3V5-KanMX/atg40::ATG40-3V5-KanMX*
21271	*MATa/alpha, rtn1::RTN1-eGFP-KanMX/rtn1::RTN1-eGFP-KanMX, his3::VPH1-mCherry-HISMX6/his3::VPH1-mCherry-HISMX6*
21272	*MATa/alpha, rtn1::RTN1-eGFP-KanMX/rtn1::RTN1-eGFP-KanMX, his3::VPH1-mCherry-HISMX6/his3::VPH1-mCherry-HISMX6, atg39::NatMX/atg39::NatMX*
21377	*MATa/alpha, rtn1::RTN1-eGFP-KanMX/rtn1::RTN1-eGFP-KanMX, his3::VPH1-mCherry-HISMX6/his3::VPH1-mCherry-HISMX6, atg40::KanMX/atg40::KanMX*
21378	*MATa/alpha, rtn1::RTN1-eGFP-KanMX/rtn1::RTN1-eGFP-KanMX, his3::VPH1-mCherry-HISMX6/his3::VPH1-mCherry-HISMX6, atg39::NatMX/atg39::NatMX, atg40::KanMX/atg40::KanMX*
23422	*MATa/alpha, GFP-SCS2/GFP-SCS2, htb1::HTB1-mCherry-HISMX6/htb1::HTB1-mCherry-HISMX6*
23423	*MATa/alpha, GFP-IST2/GFP-IST2, htb1::HTB1-mCherry-HISMX6/htb1::HTB1-mCherry-HISMX6*
23592	*MATa/alpha, GFP-SCS2/GFP-SCS2, htb1::HTB1-mCherry-HISMX6/htb1::HTB1-mCherry-HISMX6, lnp1::NatMX/lnp1::NatMX*

23593	*MATa/alpha, rtn1::RTN1-eGFP-KanMX/rtn1::RTN1-eGFP-KanMX, atg40::pCUP1-ATG40-3V5-KanMX/atg40::pCUP1-ATG40-3V5-KanMX, ime1::HygB/ime1::HygB*
23595	*MATa/alpha, GFP-SCS2/GFP-SCS2, trp1::pARO10-mCherry-HDEL-TRP/trp1::pARO10-mCherry-HDEL-TRP*
23677	*MATa/alpha, rtn1::RTN1-eGFP-KanMX/rtn1::RTN1-eGFP-KanMX, his3::VPH1-mCherry-HISMX6/his3::VPH1-mCherry-HISMX6, atg1::ATG1-IAA7-3V5-KanMX/atg1::ATG1-IAA7-3V5-KanMX*
23678	*MATa/alpha, rtn1::RTN1-eGFP-KanMX/rtn1::RTN1-eGFP-KanMX, his3::VPH1-mCherry-HISMX6/his3::VPH1-mCherry-HISMX6, ndt80::LEU2/ndt80::LEU2*
23679	*MATa/alpha, rtn1::RTN1-eGFP-KanMX/rtn1::RTN1-eGFP-KanMX, his3::VPH1-mCherry-HISMX6/his3::VPH1-mCherry-HISMX6, ime1::HygB/ime1::HygB*
23760	*MATa/alpha, rtn1::RTN1-eGFP-KanMX/rtn1::RTN1-eGFP-KanMX, his3::VPH1-mCherry-HISMX6/his3::VPH1-mCherry-HISMX6, atg1::ATG1-IAA7-3V5-KanMX/atg1::ATG1-IAA7-3V5-KanMX, his3::pCUP1-osTIR1-HIS3/his3::pCUP1-osTIR1-HIS3*
23901	*MATa/alpha, rtn1::RTN1-eGFP-KanMX/rtn1::RTN1-eGFP-KanMX, trp1::pARO10-mCherry-HDEL-TRP/trp1::pARO10-mCherry-HDEL-TRP*
23906	*MATa/alpha, rtn1::RTN1-eGFP-KanMX/rtn1::RTN1-eGFP-KanMX, trp1::pARO10-mCherry-HDEL-TRP/trp1::pARO10-mCherry-HDEL-TRP, ura3::PIL1-antiGFP-URA3/ura3::PIL1-antiGFP-URA3*
24144	*MATa/alpha, tcb3::TCB3-eGFP-KanMX/tcb3::TCB3-eGFP-KanMX, his3::VPH1-mCherry-HISMX6/his3::VPH1-mCherry-HISMX6*
24147	*MATa/alpha, GFP-IST2/GFP-IST2, his3::VPH1-mCherry-HISMX6/his3::VPH1-mCherry-HISMX6*
24216	*MATa/alpha, trp1::pARO10-GFP-HDEL-TRP1/trp1::pARO10-GFP-HDEL-TRP1, htb1::HTB1-mCherry-HISMX6/htb1::HTB1-mCherry-HISMX6, tcb1::HygB/tcb1::HygB, tcb2::NatMX/tcb2::NatMX, tcb3::KanMX/tcb3::KanMX*
24308	*MATa/alpha, trp1::pARO10-GFP-HDEL-TRP1/trp1::pARO10-GFP-HDEL-TRP1, htb1::HTB1-mCherry-HISMX6/htb1::HTB1-mCherry-HISMX6, tcb1::HygB/tcb1::HygB, tcb2::NatMX/tcb2::NatMX, tcb3::KanMX/tcb3::KanMX, ist2::NatMX/ist2::NatMX*
24318	*MATa/alpha, trp1::pARO10-GFP-HDEL-TRP1/trp1::pARO10-GFP-HDEL-TRP1, htb1::HTB1-mCherry-HISMX6/htb1::HTB1-mCherry-HISMX6, ist2::NatMX/ist2::NatMX*
24590	*MATa/alpha, GFP-SCS2/GFP-SCS2, trp1::pARO10-mCherry-HDEL-TRP/trp1::pARO10-mCherry-HDEL-TRP, ura3::PIL1-antiGFP-URA3/ura3::PIL1-antiGFP-URA3*
25395	*GFP-IST2/GFP-IST2, trp1::pARO10-mCherry-HDEL-TRP/trp1::pARO10-mCherry-HDEL-TRP*
25434	*MATa/alpha, GFP-SCS2/GFP-SCS2, his3::VPH1-mCherry-HISMX6/his3::VPH1-mCherry-HISMX6*
25627	*MATa/alpha, ura3::pATG8-GFP-SCS22-URA3/ura3::pATG8-GFP-SCS22-URA3, htb1::HTB1-mCherry-HISMX6/htb1::HTB1-mCherry-HISMX6*
26168	*MATa/alpha, GFP-SCS2/GFP-SCS2, atg40::ATG40-3V5-KanMX/atg40::ATG40-3V5-KanMX, lnp1::NatMX/lnp1::NatMX*
26179	*MATa/alpha, om45::OM45-eGFP-KanMX/om45::OM45-eGFP-KanMX, ime1::HygB/ime1::HygB*
26180	*MATa/alpha, ura3::GFP-ATG8-URA3/ura3::GFP-ATG8-URA3, atg8::TRP1/atg8::TRP1, ime1::HygB/ime1::HygB*
26203	*MATa/alpha, rtn1::RTN1-eGFP-KanMX/rtn1::RTN1-eGFP-KanMX, atg40::ATG40-3V5-KanMX/atg40::ATG40-3V5-KanMX*
26204	*MATa/alpha, rtn1::RTN1-eGFP-KanMX/rtn1::RTN1-eGFP-KanMX, his3::VPH1-mCherry-HISMX6/his3::VPH1-mCherry-HISMX6, ura3::PIL1-antiGFP-URA3/ura3::PIL1-antiGFP-URA3*
26260	*MATa/alpha, GFP-SCS2/GFP-SCS2, atg40::ATG40-3V5-KanMX/atg40::ATG40-3V5-KanMX, rtn1::KanMX/rtn1::KanMX, rtn2::NatMX/rtn2::NatMX, yop1::KanMX/yop1::KanMX*

Table 2.2 – Primers used in this study

construct	forward primer	reverse primer
rtn1Δ	GCAAATATGTCCGCCTCAGCTCAACATAGCCAAGCCCAACCGGATCCCCGGGTTAATTAA	GCACTCAAGCGTTGTTTTTTTCCAATTCATTTTGCAAGTTGAATTCGAGCTCGTTTAAAC
rtn2Δ	GCCACAAACTATCATCAACATGAATAGGAATACGACTACCcggatccccgggttaattaa	CTAGATTATGCGTGTTGCAATTTTTGCTTTAGGCCGTGCGgaattcgagctcgtttaaac
yop1Δ	ATGTCCGAATATGCATCTAGTATTCACTCTCAAATGAAACcggatccccgggttaattaa	CTTAATGAACAGAAGCACCTGTAGCCTTAGAAGCCTCATTgaattcgagctcgtttaaac
lnp1Δ	CATACAAAGAGGAGATCGGATATAAAAGAATAATATAAATcggatccccgggttaattaa	TAAAAATATATTATATAGGGGTACGTAGTTATTCTAACGCgaattcgagctcgtttaaac
sey1Δ	ACGGGCTACTAACTCACTCGACAGTTGACATACTTTAGTCcggatccccgggttaattaa	CAAAAAAGTAAACACGGTAAATTGAAATAAATTATTCGATgaattcgagctcgtttaaac
atg39Δ	taatagagactagtaaaacaatcgagttgtcggacctaaacggatccccgggttaat	ttgttaatttcattcttcatgctgggttttggatgatctatcgatgaattcgagctcg
atg40Δ	GAAACAACTTTCCTAAGCAGCGAAATACACGTGCAAGAGCCGGATCCCCGGGTTAATTAA	CTTCATAGACTACCATTATGGTAAAATGGAAAAACTATTCGAATTCGAGCTCGTTTAAAC
ime1Δ	ATAAAAGAAAAGCTTTTCTATTCCTCTCCCCACAAACAAAcggatccccgggttaattaa	TTGAGGGAAGGGGGAAGATTGTAGTACTTTTCGAGAAcactagtggatctgatatcatcg
tcb1Δ	TAGTGCATTCTGAAAACTTCAATTGCGTGGTACATACAATcggatccccgggttaattaa	TTTATATTTTACACAGTGCATCTTGTCCCTCTCTTTCTCGtcgatgaattcgagctcg
tcb2Δ	AACAACAGGTGTTAGGTTAAACTGCTTTGACTTTTTGTTCcggatccccgggttaattaa	GGTTCAATAGTGGGGAAAAATCGCAAATCAAATGTCAACTgaattcgagctcgtttaaac
tcb3Δ	tacgcattgaaaagtccagaaaacggatccccgggttaattaa	GCGTATAAAAGAATAGTTTTCACTGTTTgaattcgagctcgtttaaac
ist2Δ	TTGAAAAAGATTAAAACAAGCACAAGCGGTTGAGCATACTcggatccccgggttaattaa	ATATTATAAAAATAAAATTTGTTATCGTCCTAGCTTTTTTtcgatgaattcgagctcg
Sec63-GFP	CGATACGGATACAGAAGCTGAAGATGATGAATCACCAGAAGGTGACGGTGCTGGTTTA	TCTAAGAGCTAAAATGAAAAACTATACTAATCACTTATATTCGATGAATTCGAGCTCG
OM45-GFP	AAGAATGGAATGATAAGGGTGATGGTAAATTCTGGAGCTCGAAAAAGGACcggatccccgggttaattaa	ATATGTATATATGTTATGCGGGAACCAACCCTTTACAATTAGCTATCTAAgaattcgagctcgtttaaac
Rtn1-GFP	AAAGTTAGCTATTCTTGTTTGAAATGAAAAAAAAAGCACtcgatGAATTCGAGCTCG	TACAAAAAACTTGCAAAATGAATTGGAAAAAAACAACGCTGGTGACGGTGCTGGTTTA
Sey1-GFP	CAAAAAAGTAAACACGGTAAATTGAAATAAATTATTCGATtcgatgaattcgagctcg	TGAAATGAAAGACTTCTCAAAAAACGAGCAAAAAGAAAAAGGTGACGGTGCTGGTTTA
Tcb1-GFP	TAAGAAGAATCATGAGATGGGCGAAGAAGAAACTAAGTTTggtgacggtgctggttta	TTTATATTTTACACAGTGCATCTTGTCCCTCTCTTTCTCGtcgatgaattcgagctcg
Tcb2-GFP	GTCTACAACCACTGGGGACAAAAAATCCGAAGAGAAGCAAggtgacggtgctggttta	AAGATGATTTCGTGACACATACTCTTTACCATCGATAGAAtcgatgaattcgagctcg
Tcb3-GFP/RFP	GGTACCTCCCGTGCCAGAAGTTCCTCAAGAATACACGCAGggtgacggtgctggttta	AACAAACACAGAAAAGACACCTGTTAACACACCAAATGTGtcgatgaattcgagctcg
Atg1-IAA7-3V5	CAGGTTGAAAATATTGAGGCAGAAGATGAACCACCAAAATCGGATCCCCGGGTTAATTAA	GGTCATTTGTACTTAATAAGAAAACCATATTATGCATCACGAATTCGAGCTCGTTTAAAC
Pil1-antiGFP	GGACACCAGCAAAGTGAGTCTCTTCCCCAACAAACAACAGCTggtgacggtgctggttta	TTTTTTTTTTTTTGTTTCTAATAGATTGTTGATTTATTTTGAtcgatgaattcgagctcg
Atg40-3V5	TTTTATGGAGGATATTCTAGATGAGACAACTGAATTGGATcggatccccgggttaattaa	CCTTCATAGACTACCATTATGGTAAAATGGAAAAACTATTgaattcgagctcgtttaaac
Scs2 guide	gactAGCAGACATACTTAGGTTCG	aaacCGAACCTAAGTATGTCTGCT
GFP-Scs2 template	TAATAGTGTAGCAGAAGTGTATTCTACAATCTgCGCGAACCTAAGTatgggtgacggtgc	TATACACCAACACGTCAGGcGAAATTTCAACAGCAGACATtggatccactagttctagag
Ist2guide	gactAAGATTAAAACAAGCACAAG	aaacCTTGTGCTTGTTTTAATCTT
GFP-Ist2 template	tggatccactagttctagagcggccgcttgtttgtacaattcatccatacc	TAACACAATTCGGATCTAGAGATGTAATTGTCTGCGACATtggatccactagttctagag

Table 2.3 – Plasmids used in this study

plasmid name	description
pÜB1	pFA6A-KanMX
pÜB153	pFA6A-NatMX
pÜB182	pFA6A-eGFP-KanMX
pÜB185	pFA6A-mKate2-URA3
pÜB217	pFA6A-hphNT1
pÜB737	pNH604-pARO10-GFP-HDEL-TRP1
pÜB763	pFA6A-IAA7-3V5-KanMX
pÜB1185	pNH604-pARO10-mCherry-HDEL-TRP1
pÜB1548	pRS306-pATG8-linker-eGFP-ATG8
pÜB1707	pFA6A-link-VH16-caURA3
pÜB1834	URA/CEN-Cas9-SCS2gRNA
pÜB1889	pRS306-pATG8-linker-eGFP-SCS22
pÜB1977	pFA6A-pCUP1-ATG40-3V5-hphNT1
pÜB1978	URA/CEN-Cas9-IST22gRNA

Table 2.4 – Microscopy settings used in this study

Figure 2.x	GFP	RFP	Pol	Z sectioning
1A, 1F-G, 2A, 2D, 3A, 3C-E, 4F-G, 5B, S2A-F, S2H-J, S3B-C, S7A	32% T, 0.025 s	32% T, 0.025 s	32% T, 0.1 s	1 µm, 7 sections
1B, 2C, S2G	32% T, 0.025 s	100% T, 0.025 s	32% T, 0.1 s	1 µm, 7 sections
2B	32% T, 0.025 s	100% T, 0.1 s	32% T, 0.1 s	1 µm, 7 sections
2F, 4B-E	32% T, 0.025 s	100% T, 0.05 s	32% T, 0.1 s	1 µm, 7 sections
6C, 6F, 6I, 7C	100% T, 0.025 s	100% T, 0.1 s	32% T, 0.1 s	0.5 µm, 15 sections
S3A, S3D	32% T, 0.025 s	32% T, 0.025 s	32% T, 0.1 s	0.5 µm, 15 sections
S3E	100% T, 0.025 s	32% T, 0.025 s	32% T, 0.1 s	0.5 µm, 15 sections

2.7 Supplementary figures

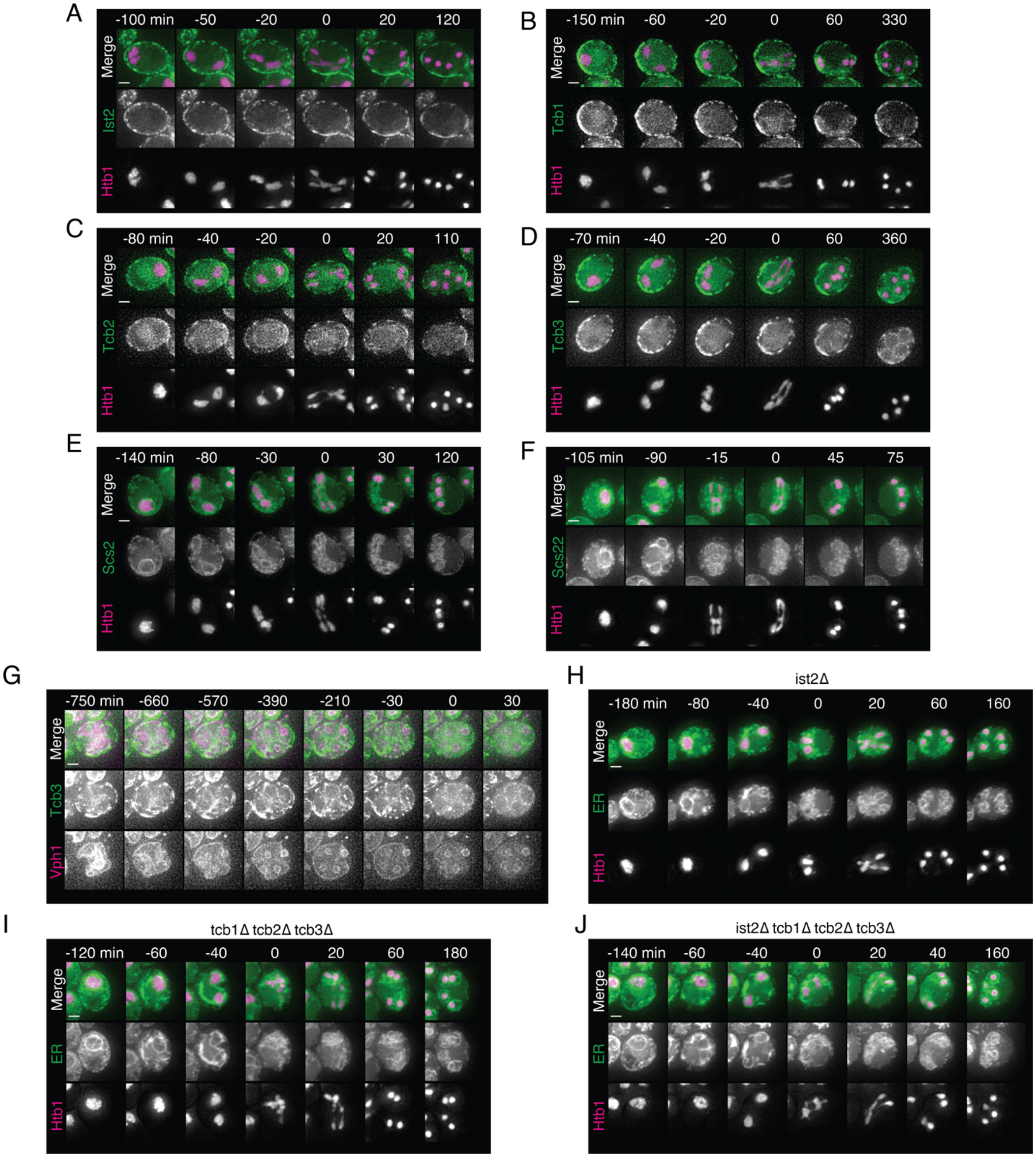

Figure 2.S1. A subset of ER-PM tethering proteins marks cortically retained ER islands. (A-F) Time-lapse microscopy of cells expressing Htb1-mCherry and the indicated GFP-tagged ER-PM tether protein, imaged every 10 minutes during meiosis. Minute 0 is defined as the onset of anaphase II. (G) Time-lapse microscopy of cells expressing Tcb3-GFP and Vph1-mCherry imaged every 30 minutes during meiosis. Minute 0 is defined as the time of vacuole lysis. (H-I) Time-lapse microscopy of cells of the indicated genotypes expressing GFP-HDEL (ER) and Htb1-mCherry imaged every 10 minutes during meiosis. Scale bar = 2 μm for all panels.

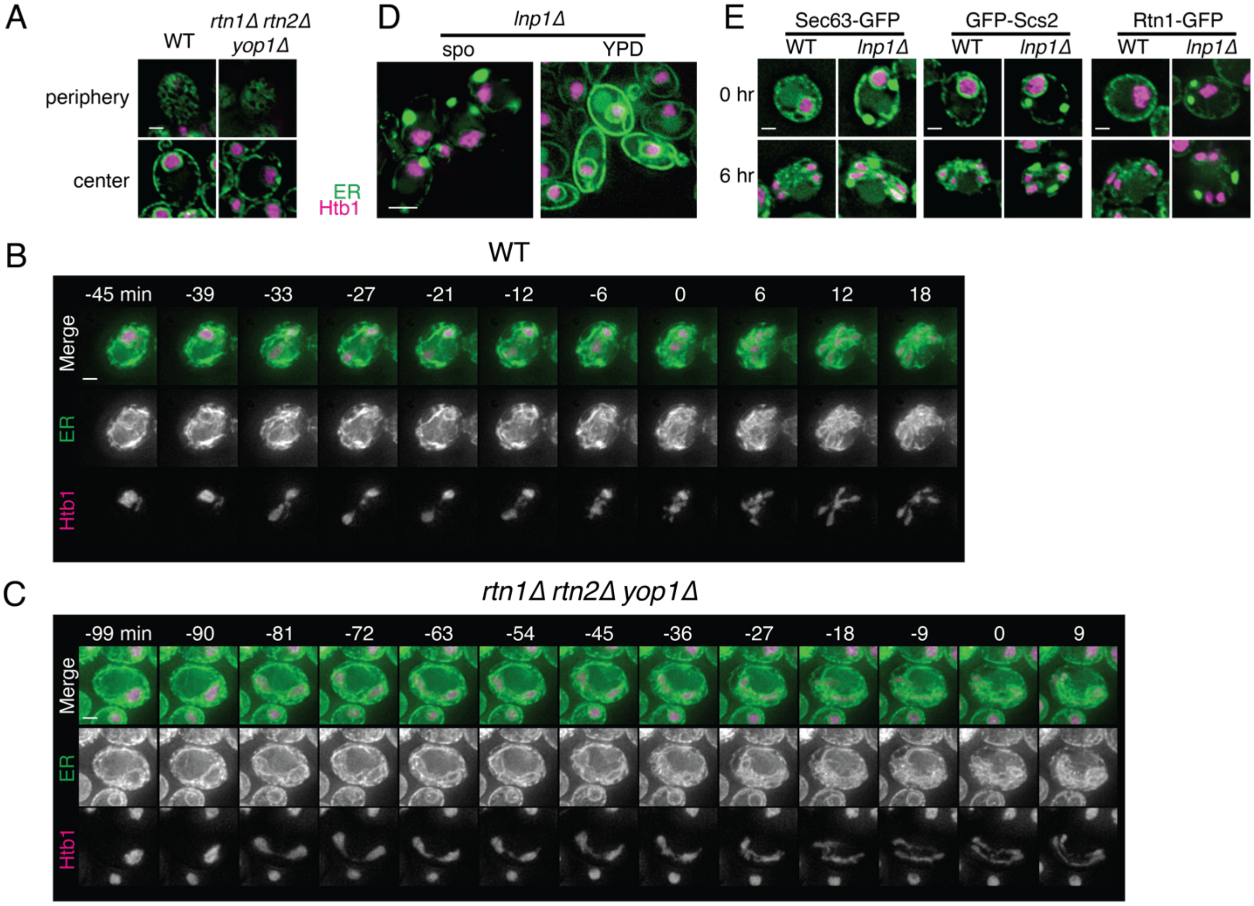

Figure 2.S2. Reticulons and Lnp1 regulate meiotic ER remodeling. (A) WT and rtn1Δ rtn2Δ yop1Δ cells expressing GFP-HDEL (ER) and Htb1-mCherry imaged at the cell periphery and cell center immediately after transfer to SPO. (B) Time-lapse microscopy of cells expressing GFP-HDEL (ER) and Htb1-mCherry imaged every 3 minutes in meiosis. Minute 0 is defined as the time of ER collapse. (C) As in (B) but with cells of genotype rtn1Δ rtn2Δ yop1Δ. (D) lnp1Δ cells expressing GFP-HDEL (ER) and Htb1-mCherry imaged immediately following transfer to SPO, or during exponential growth in YPD. (E) WT and lnp1Δ cells expressing Htb1-mCherry and the indicated GFP-tagged protein imaged at 0 or 6 hr after transfer to SPO. Scale bar = 2 μm for all panels.

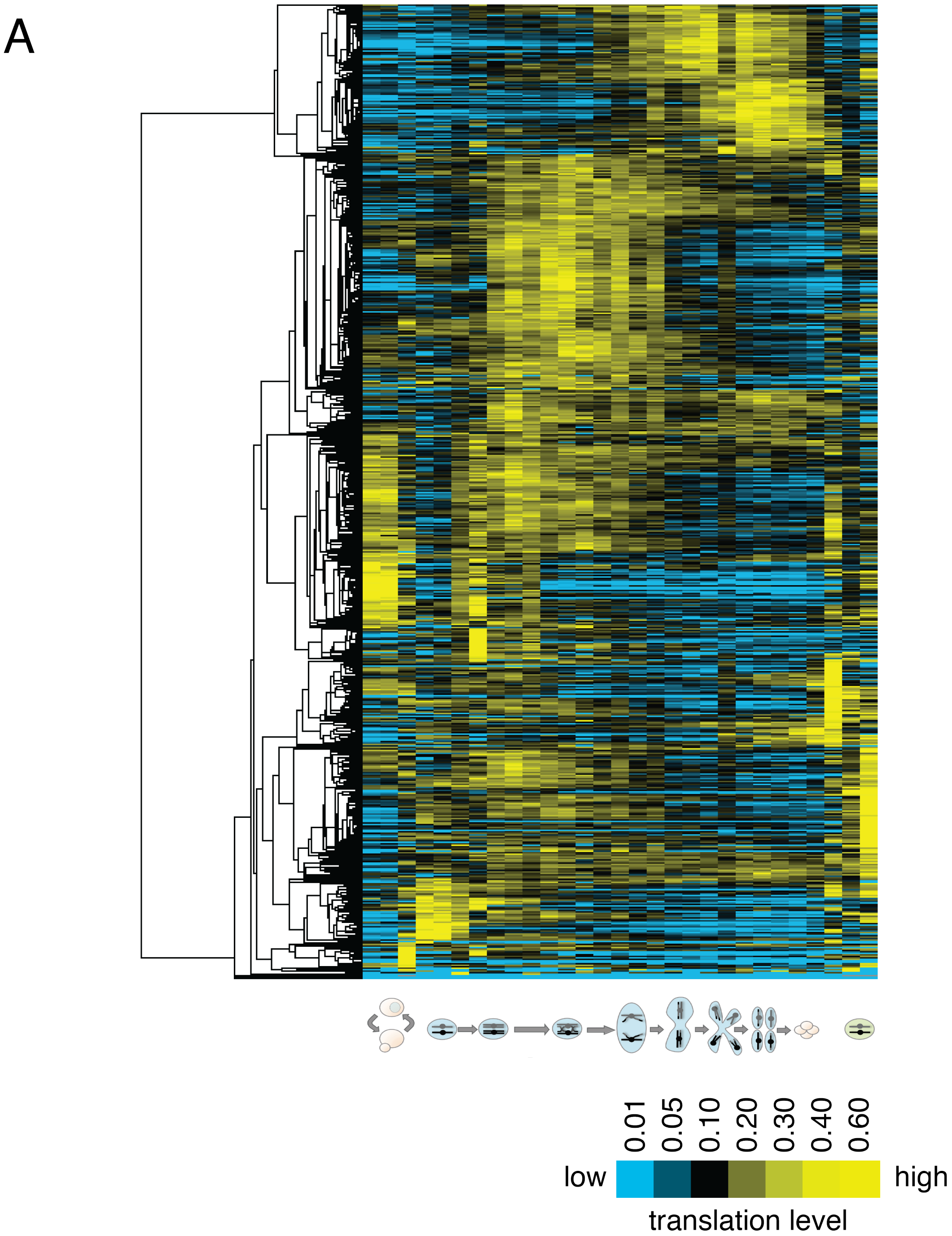

Figure 2.S3. The ER undergoes turnover and resynthesis during meiosis. (A) Hierarchical clustering of translation levels for all genes annotated for ER localization using on ribosome profiling data published in Brar, *et. al.* (2012). Footprint FPKM are normalized within each gene to facilitate comparisons of expression patterns between genes indpendent of overall abundance.

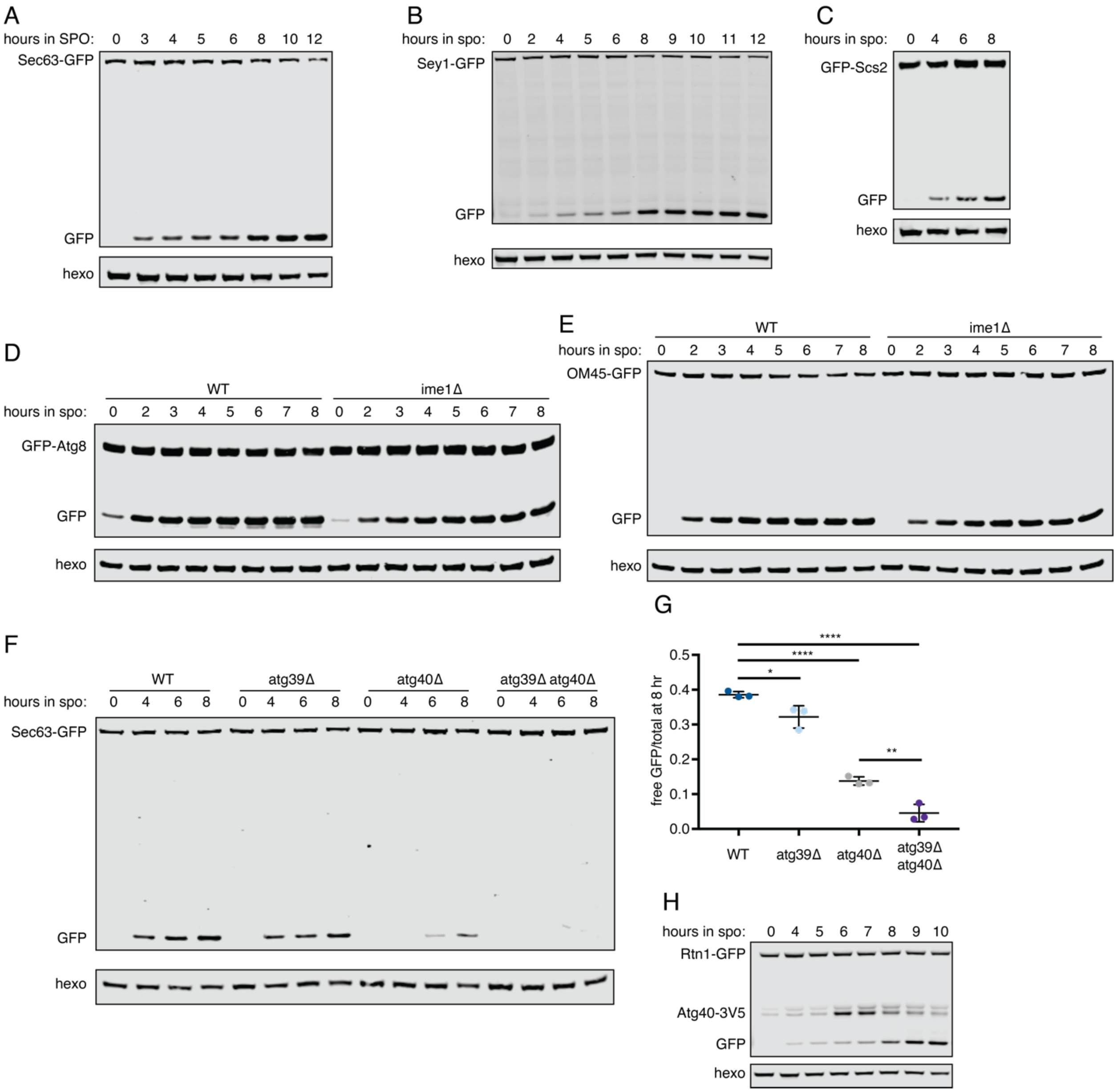

Figure 2.S4. The ER is degraded by selective autophagy during meiosis. (A-C) Western blot using samples from WT cells expressing the indicated GFP-tagged protein taken at the indicated times in meiosis. Blots were probed for GFP and hexokinase. (D) Western blot using samples from WT and ime1Δ cells expressing GFP-Atg8 taken at the indicated times during meiosis. Blots were probed for GFP and hexokinase. (E) As in (D) but with cells expressing OM45-GFP instead of GFP-Atg8. (F) Western blot using samples from cells of the indicated genotypes expressing Sec63-GFP taken at the indicated times in meiosis. Blots were probed for GFP and hexokinase. (G) Quantification of free GFP as a proportion of the total GFP signal at 8 hr from three replicates of the experiment in (F). (H) Western blot using samples from WT cells expressing Rtn1-GFP and Atg40-3V5 taken at the indicated times in meiosis. Blot was probed for GFP, V5 and hexokinase.

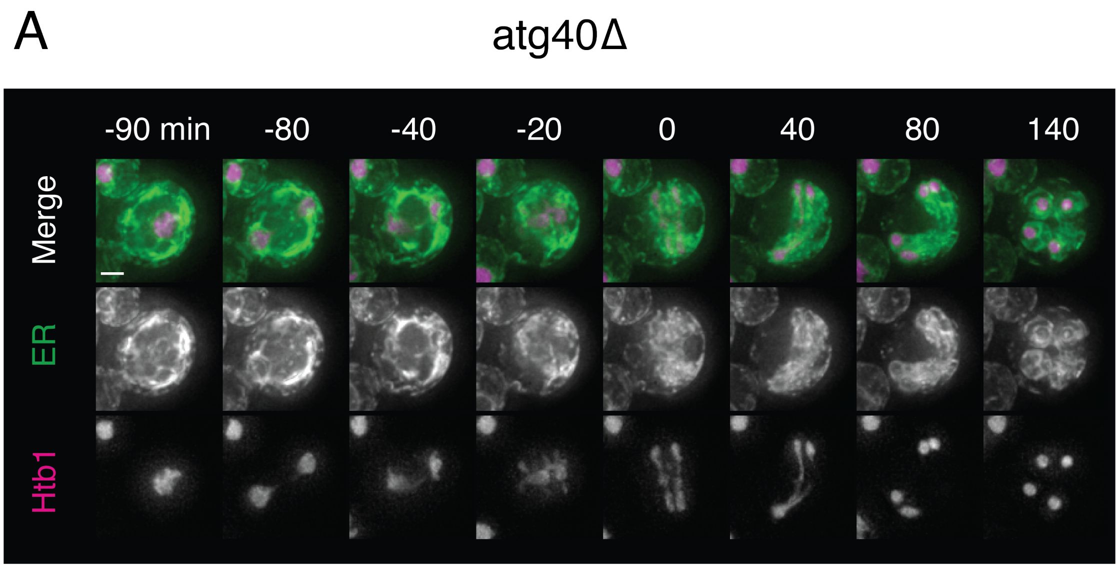

Figure 2.S5. ER collapse is required for ERphagy. (A) Time-lapse microscopy of atg40Δ cells expressing GFP-HDEL (ER) and Htb1-mCherry imaged every 10 minutes during meiosis. 0 min is defined as the time of ER collapse. Scale bar = 2 μm.

Chapter 3: ER remodeling and quality control in meiosis – discussion and future directions

In chapter 2, we identified a developmental pathway that remodels the ER to simultaneously ensure organelle degradation and inheritance in a selective manner. Central to this pathway is a transition in the fundamental nature of the ER from continuous to fragmented, which we propose is achieved by reticulon-mediated membrane fission and inhibition of fusion by Lnp1. Selective ER destruction is achieved by two parallel mechanisms: cortical ER retention and selective autophagy. Overall, these results identify novel roles for ER structuring proteins, ER-PM tethers, and ERphagy in meiotic ER remodeling and provide a framework for further investigation of ER dynamics and quality control during cell differentiation.

3.1 Regulation of ER remodeling in meiosis

Developmental regulation of ER dynamics by membrane fragmentation is an intriguing new concept. It will be important to further characterize cortical ER fragments by electron microscopy and fluorescence recovery after photobleaching (FRAP)-based assays. Once we have a better understanding for the structure of the cortically retained compartment, we can address how compartmentalization is regulated during meiosis.

3.1.1 How is reticulon-dependent membrane fragmentation regulated?

A major unanswered question raised by the work presented here is how reticulon-mediated membrane fragmentation is regulated to achieve precisely timed ER detachment. One potential driver of membrane fission is elevated reticulon concentration. In some cases, fragmentation occurs globally upon reticulon overexpression (Espadas et. al., 2019; Wang et. al., 2016), whereas in other cases fragmentation relies a high *local* reticulon concentration achieved through multivalent interactions or oligomerization (Mochida et. al., 2020; Bhaskara et. al., 2019; Jiang et. al., 2020; Grumati et. al., 2017). In at least one case, reticulon phosphorylation promotes oligomerization and consequent fragmentation (Jiang et. al., 2020). Several lines of reasoning lead us to favor a regulated oligomerization model rather than increased reticulon expression as the mechanism driving meiotic ER fragmentation. First, new protein synthesis on the scale required to drive fragmentation is slow and energetically costly relative to the regulatory mechanisms that might control oligomerization, such as phosphorylation. Second, global measurements of protein synthesis and abundances suggest that reticulon levels do not appreciably increase during the time leading up to ER collapse (Brar et. al., 2012; Cheng et. al., 2018). Third, fragmentation purely as a result of reticulon abundance has only been observed in artificial contexts, such as *in vitro* or overexpression systems in which reticulons greatly exceed physiological levels. In contrast, regulated reticulon oligomerization is a logical and concerted mechanism deployed by cells in response to specific challenges (Jiang et. al., 2020).

In exploring the mechanistic role of reticulons in ER collapse, it will first be important to determine the extent to which reticulons oligomerize and whether this characteristic changes throughout meiosis. Reticulon oligomerization can be assessed by fractionation along a sucrose gradient, with higher-order oligomers sedimenting at higher sucrose densities (Shibata et. al., 2008). Alternatively, reticulon self-interaction can be demonstrated by co-immunoprecipitation from samples harboring two differently tagged reticulon proteins (Jiang et. al., 2020), or by immunoblotting following chemical crosslinking (Zurek et al., 2011). All of these methods have been used to characterize mutants that affect oligomerization, suggesting that they will be sensitive to potential changes in this parameter over the course of meiosis.

What other factors regulate reticulon-dependent membrane remodeling? There is precedent in the literature for phosphorylation as a driver of both reticulon oligomerization (Jiang et. al., 2020) and organelle remodeling in meiosis (Sawyer et. al., 2019), making this an appealing potential mechanism. Detection of meiosis-specific phosphorylated species by mass spectrometry and/or Phos tag gel shift would provide support for this model (Jiang et. al., 2020). Ime2 is a meiosis-specific kinase and a promising candidate regulator of reticulon function and meiotic ER dynamics. Alleles for inhibition or ectopic activation of Ime2 are well characterized and can easily be integrated into the reticulon and ER dynamics assays described above and in chapter 2 (Berchowitz et. al., 2013). Moreover, there is precedent for Ime2-dependent organelle remodeling in meiosis, as phosphorylation of the mitochondria-ER cortical anchor (MECA) complex, leads to MECA degradation and consequent mitochondrial detachment from the plasma membrane (Sawyer et. al., 2019). Regardless of if we are able to detect reticulon phosphorylation in meiosis, it will be important to determine the role of Ime2 in meiotic ER remodeling.

3.1.2 How do ER-PM tethers affect ER collapse?

We found that four ER-PM tethers anchor ER fragments at the cell cortex throughout meiosis, ensuring their exclusion from gametes and subsequent degradation. These tethers also progressively cluster together prior to ER collapse and coincident with ER cabling, suggesting a potential role for tether dynamics in meiotic ER remodeling. Tricalbins and the related extended synaptotagmins have been reported to dimerize, though whether and how these interactions might be regulated, and if they have the propensity to form higher-order structures, is not well established (Creutz et al., 2004; Giordano et al., 2013). It may be informative to dissect the molecular requirements for tether clustering, and whether disrupting these clusters affects ER cabling and collapse. A complimentary line of inquiry would be to assess how tether clustering is affected in mutants with altered ER dynamics in meiosis, namely *lnp1Δ* and *rtn1Δ rtn2Δ yop1Δ*. Tricalbins contain a hairpin-like transmembrane segment that causes them to localize preferentially to ER tubules, an effect that is exaggerated when tubules are depleted via loss of Rtn1 and Yop1 (Hoffman et. al., 2019). Moreover, tricalbins are unique among yeast ER-PM tethers in that they form peaks of exceptionally high curvature when contacting the plasma membrane (Collado et. al., 2019). Whether the tricalbin hairpin-like membrane domain can directly promote membrane curvature is still unclear, but is seems plausible that tether clustering, similar to reticulon oligomerization, could generate an area of high membrane curvature favorable for fission. Loss of the tricalbins does not prevent ER collapse, likely because the absence of their tethering activity would likely mask any potential effect on membrane fission. One way to test a potential role of tricalbins in membrane fission would be to combine *tcb1Δ tcb2Δ tcb3Δ* with the *rtn1Δ rtn2Δ yop1Δ* background. If tricalbins promote membrane scission in this context, their deletion might paradoxically result in an *increase* in cortically retained ER, as fragmentation would be further disrupted and at least one cortically retained tether (Ist2) would still be expressed.

Cells lacking the four cortically retained ER-PM tethers still show some amount of cortical ER throughout meiosis, suggesting the presence of other tethering factors. Scs2 and Scs22, the other validated ER-PM tethers in yeast (Manford et. al., 2012), are not cortically retained in WT meiosis, but it is possible that they compensate for loss of Ist2 and the tricalbins to promote cortical ER retention. Loss of all six tethers (Δtether) reduces basal cortical ER levels and cell fitness, making it difficult to analyze cortical ER dynamics in this context. A combination of conditional depletion and fully null alleles may be necessary to determine the set of tethers required for cortical ER retention in meiosis.

Apart from the six characterized tethers, additional yeast proteins are plausible mediators of ER-PM contacts. In yeast and human cell lines, Sec22 interacts with plasma membrane proteins and alters inter-membrane distance (Petkovic et. al., 2014). Other proteins have been found to localize to ER-PM contacts, even in Δtether cells (Topolska et. al., 2020), suggesting that they or an associated protein may mediate tethering. Imaging of these proteins in meiosis may yield insight into their potential function as ER-PM tethers.

3.1.3 What is the role of the actin cytoskeleton in ER collapse and inheritance?

We found that preventing actin polymerization using Latrunculin A (LatA) also blocked ER collapse, though whether actin-dependent forces directly mediate collapse is yet to be determined. The actin cytoskeleton is known to have a direct role in ER inheritance during mitotic cell division in yeast. Tubular ER is delivered to the bud along actin cables via the motor protein Myo4 and the adaptor protein She3 (Estrada et. al. 2003). It will be important to determine whether these proteins also mediate ER collapse and delivery into gametes in meiosis, or whether alternative meiosis-specific motor/adaptor proteins serve an analogous role. Because LatA treatment prevents the completion of meiosis, likely due to general toxicity, identification of specific proteins responsible for a meiotic actin-ER interface will be crucial for characterizing actin-dependent ER inheritance without the complicating effects of harsh drug treatment.

In vitro experiments indicate that a combination of tubule curvature and pulling forces increase the propensity of tubules to undergo scission (Espadas et. al., 2019). This raises the possibility that forces generated by actin motors pulling on the cortical ER may contribute directly to the fragmentation process rather than simply promoting the collapse of ER that is already fragmented. Thus, actin-dependent fragmentation may explain the persistence of ER collapse in the absence of reticulons.

3.1.4 "You can observe a lot just by watching"

Yogi Berra, as far as I am aware, never touched a microscope. Nevertheless, his words ring true in the context of my PhD. Some of the most exciting and surprising results presented here were the result of taking a look at a new genotype or fluorescently tagged protein under the microscope and seeing a surprising but unmistakable result that I would never have predicted beforehand. With that in mind, there are advanced imaging techniques that, with careful time investment and help from expert collaborators, could greatly improve our understanding of the phenomena presented here, as well as other cell biological phenomena in meiosis.

A full accounting of ER and other membrane structure at the various stages of meiotic cell remodeling would provide important context and generate new avenues of investigation. The gold standard for this approach is fixed ion beam scanning electron microscopy (FIB-SEM), which can be used to produce stunning, high resolution 3D reconstruction images of virtually any cellular structure (Nixon-Abell et al., 2016; Parlakgül et al., 2020). Recent technological advances have streamlined throughput, image segmentation and reconstruction, greatly facilitating data analysis (Parlakgül et al., 2020; Zachs et al., 2020). FIB-SEM reconstructions of cells undergoing meiosis would be an invaluable resource for understanding the changes in cellular structures that drive meiosis. As an alternative to FIB-SEM, it may be worth investing effort in serial transmission EM, which has reduced resolution in the Z plane compared to FIB-SEM but is more widely available and cheaper.

A drawback of FIB-SEM is that it cannot be used to examine live cells. Structured illumination microscopy (SIM) is a super-resolution imaging technique that can achieve resolution as low as 100 nm (compared to 200 nm in diffraction-limited microscopy), and can be used in live or fixed cells (Chang et al., 2017). Even a marginal improvement in resolution for the live cell imaging presented in chapter 2 would help our understanding of ER fragmentation, cabling and collapse. Of particular interest would be greater insight into the dynamics of ER-PM tethers, reticulons, and Lnp1 relative to the rest of the ER.

3.2 Cortical ER retention as a meiotic quality control mechanism

One of the most surprising findings presented in chapter 2 is the existence of an ER compartment that is physically excluded from gamete cells by virtue of its tethering to the plasma membrane. This raises the intriguing possibility that cells partition toxic or otherwise unwanted material to this compartment as a means of ER quality control during meiosis. In this way, cortically retained ER may be analogous to the gametogenesis uninherited nuclear compartment (GUNC), a nuclear envelope fragment that topologically separates from the rest of the nuclei late in meiosis and is excluded from gametes (King et. al., 2019). The GUNC contains nuclear pore complexes as well as several hallmarks of aging, including protein aggregates, extrachromosomal rDNA circles, and abnormal nucleolar structures. Cortically retained ER may serve a similar function for materials that need to be sequestered from gametes but are inaccessible to the GUNC. This raises several new questions about the molecular nature of cortically retained ER and its role in ensuring gamete health.

3.2.1 What is the molecular composition of cortically retained ER?

What proteins localize to the cortically retained ER? We have already identified Ist2 and the tricalbins as specific markers of cortically retained ER, but identifying other proteins enrich there would help us to define the function of this compartment. One potential approach to this question involves membrane fractionation and detergent-free immunoprecipitation of a tagged ER protein followed by mass spectrometry, which has been used to identify tubular ER-enriched proteins in yeast (Wang et. al., 2017). Because membranes are preserved in this approach, it enables detection of proteins that are present within the same membrane domain but do not physically interact with the immunoprecipitated protein. The four cortically retained ER-PM tethers would all be suitable bait proteins, as they appear to localize exclusively to cortical ER fragments. Ist2 and Tcb3 are the most abundant, and have also been suggested to mark overlapping but distinct cortical ER domains (Hoffman et. al., 2019), so it may be useful to try this approach with multiple tethers.

As an alternative to biochemical purification of cortically retained ER microsomes, proximity labeling can be used to detect proteins that are in close contact with ER-PM tethers. By tagging one or more tethers with a promiscuous biotin ligase and pulsing biotin into cultures after ER collapse, we should be able to specifically label proteins in the cortically retained ER (Branon et al., 2018). Additional specificity may be achieved using a split biotin ligase that is only active when both components are present and in close proximity (Cho et al., 2020). Tagging a plasma membrane protein with one half of the split ligase and a tether protein with the other would give us additional confidence that only those proteins within the cortical ER are labeled. The ease of purifying biotin conjugates is a benefit of this approach. Drawbacks include the difficulty of preparing cells for synchronous meiosis in the absence of biotin, potential inefficient biotin entry into meiotic cells, and the inability to simultaneously modify cytosolic and luminal proteins. These drawbacks are avoided in the microsome pulldown approach described above, as samples are prepared from unperturbed cells.

3.2.2 How are meiotic ER dynamics altered in aged cells?

If cortically retained ER functions analogously to the GUNC in mediating the elimination of damaged materials that accrue with age, one might expect this compartment to take on an expanded or otherwise altered appearance in aged cells. Any differences between aged and young ER in meiotic cells would provide new insight into the function of meiotic ER remodeling. More generally, the effects of aging on ER morphology in yeast are underexplored and likely worth examining in WT cells and mutants with disruptions in established or putative ER quality control pathways, such as ERphagy, ERAD, UPR and ER-PM tethers. Among these, ERAD and UPR mutants are known to accelerate the effects of aging, and we should test for this phenotype in mutants for which an effect on aging has not been established (Chadwick et al., 2020; Clay et al., 2014).

3.2.3 What is the fate of ER aggregates in meiosis?

Misfolded, aggregation-prone proteins are the most commonly studied substrates for ER quality control pathways. Given their toxicity and the lengths to which cells go to eliminate other toxic materials during gametogenesis, one might predict that ER aggregates would also be actively excluded from gametes. Model aggregate-prone ER proteins include mutant versions of carboxypepdidase Y (CPY*), human alpha-1 antitrypsin (ATZ), and the cystic fibrosis transmembrane conductance regulator (CFTR), all of which can be expressed ectopically and observed as large ER-localized puncta by microscopy (Clay et. al., 2014; Piña and Niwa, 2015; Cui et. al., 2019). At least one of these aggregates, CPY*, is retained in mother cells during cell division, suggesting that ER aggregates accumulate with age and may be eliminated as part of gametogenesis-coupled rejuvenation (Clay et. al., 2014). Additionally, a mutant allele of the gene encoding translocon component Sec61, *sec61-2*, is prone to misfolding and is retained in mother cells but does not produce visible aggregates by microscopy (Clay et. al., 2014). It will be interesting to monitor the behavior of misfolded and/or aggregate-prone ER proteins during meiosis and, in particular, to see if they are sequestered from gametes via the cortically retained ER compartment. If they are indeed excluded, it will be important to test candidate factors mediating their exclusion, including ER-PM tethers, reticulons, Lnp1, and the autophagy machinery.

Apart from overexpression of protein aggregates, other conditions promote the accumulation of misfolded proteins in the ER lumen, including loss of ERAD components and treatment with UPR-inducing drugs like DTT and tunicamycin (Clay et. al., 2014; Babour et. al., 2010). These conditions also shorten replicative lifespan, suggesting that ER aggregates accelerate aging and that cells accumulating these aggregates may be particularly sensitive to the need for ER quality control in meiosis (Clay et. al., 2014). We can test this by looking for synthetic interactions between aggregate-promoting conditions and candidate quality control factors, with spore viability, ER dynamics and resetting of replicative lifespan as potential readouts.

Ist2 and the tricalbins are retained in the mother cell during mitosis and at the cell cortex during meiosis (Takizawa et. al., 2000; Okada et. al., 2017; Sugiyama and Tanaka, 2019). In other words, these tethers behave exactly the way we predict ER-associated damage to behave. We should therefore consider the possibility that ER-PM tethers are involved in the process of mitotic aggregate sequestration and/or aging. Nothing on this topic has been published, but I am sure the labs who study it have considered this possibility and it would be worth discussing with them. If ER-PM tethers are required for mitotic ER stress/aggregate accumulation, it may be difficult to assess meiotic aggregate sequestration using, for example, the 4xΔtether background described in chapter 2. One way around this would be to use the auxin-inducible degron system to deplete one or more tethers at the onset of meiosis. For example, *tcb1Δ tcb2Δ ist2Δ* cells expressing Tcb3-AID would still be able to sequester ER damage in mitosis, so depleting Tcb3 at the onset of meiosis would allow us to assess the role of these tethers in determining the fate of ER aggregates specifically in meiosis.

3.2.4 Foci in *lnp1Δ* cells as potential substrates for ER quality control

We found that *lnp1Δ* cells form massive cortical foci (blobs) that do not undergo collapse and are consequently excluded from gametes. The reduced size and frequency of blobs in *lnp1Δ sey1Δ* double mutants suggest that these blobs result from excessive Sey1-mediated fusion in the absence of Lnp1, consistent with the previously reported antagonistic relationship between these two proteins (Chen et. al., 2012). Questions still remain as to the precise structural and functional nature of ER blobs. Electron microscopy of *lnp1Δ* mutants should clarify blob structure and membrane composition. On the functional side, it is appealing to speculate that blobs are a manifestation of ER stress and therefore must be excluded from gametes. If this stress results from lack of Lnp1, rather than from the presence of ER blobs *per se*, then dissolving these blobs without resolving the stress that caused them could have negative consequences for gamete health. Indeed, *rtn1Δ rtn2Δ yop1Δ lnp1Δ* mutants lack Lnp1, fail to form blobs, and have massive (~30%) spore death. Therefore, the possibility that ER blobs are a means of sequestering ER stress in the absence of Lnp1 merits further exploration.

lnp1Δ blobs remain strictly cortical throughout meiosis. Preliminary evidence indicates that ER-PM tethers are present at the cortical edge of blobs (not shown). It will be interesting to determine whether tethers are required for the exclusion of blobs from gametes, and whether this has an effect on gamete health.

If *lnp1Δ* blobs are markers of ER stress, one might expect their inheritance to be restricted during mitosis. To test this, *lnp1Δ* cells could be arrested in meiosis prior to Ndt80 induction in a microfluidics chamber, then reintroduced to rich medium and imaged for several divisions. If blobs are detected as ER stress similar to ER aggregates, they should be retained by mother cells in a manner that can be reversed by disruption of septins (e.g. *cdc12-ts*), bud organization (e.g. *bud1Δ* or *bud6Δ*) or sphingolipid homeostasis (e.g. *sur2Δ*) (Clay et. al., 2014; Shcheprova et. al., 2008). We observed blobs in saturated culture in addition to meiosis, suggesting that their formation results from reduced nutrient availability (and possibly other conditions) rather than upon meiotic entry. It is unclear whether blob structures resolve over time when transferred from saturated to dilute rich media, or if instead they are effectively diluted out as cells divide because no new blobs are being formed. This question will be resolved in the return-to-growth experiments following meiotic arrest, but if they are naturally resolved rather than diluted out it may become necessary to identify conditions that support both blob formation and continual proliferation, such as intermediate nutrient levels or some type of stress. A screen for non-starvation conditions that produce *lnp1Δ* blobs would also serve to identify conditions in which Lnp1 activity is important. Because Lnp1 function in general is mysterious and few conditions that elicit ER remodeling have been described, this approach is likely to give rise to interesting new lines of inquiry.

Finally, we noted highly abnormal structures in *rtn1Δ rtn2Δ yop1Δ lnp1Δ* cells that do not resemble *lnp1Δ* blobs and that were inherited by gamete cells. It is possible that these structures represent stressed or damaged ER that would otherwise be localized to blobs in the presence of reticulons. These structures should first be systematically categorized and quantified. If they are present in only a subset of gametes, we can assess their effect on gamete viability by germinating cells and tracking the fate of gametes that inherited abnormal structures versus those that did not.

3.3 The developmental regulation of ERphagy

Experimental induction of ERphagy generally relies on starvation or the artificial introduction of ER stress. Our finding that ERphagy is initiated as part of the meiotic program opens up the possibility to study how this conserved process is regulated in a natural context.

3.3.1 How is autophagy receptor expression regulated in meiosis?

Previous work has identified transcriptional repressors controlling the expression of ERphagy receptor-encoding genes *ATG39* and *ATG40* during ER stress and starvation, respectively (Mizuno et. al., 2020; Cui et. al., 2019). However, whether those mechanisms activate ERphagy in a developmental context has not been addressed. None of the reported regulators of receptor expression (Mig1/Mig2 for Atg39 and Rpd3/Pho23 for Atg40) have reported roles in meiosis. If these factors are involved in the meiotic regulation of Atg39/Atg40, it will be interesting to determine their other transcriptional targets and what role they play in the meiotic program. Transcriptional regulation in meiosis is much more complex than can currently be explained by the activity of well-defined meiotic transcription factors (Brar et. al., 2012). It is therefore important to identify novel regulators of gene expression meiosis, particularly in late meiosis where dramatic cell remodeling events occur but for which defining gene regulatory events have not been fully elucidated.

3.3.2 What cargo is subject to meiotic ERphagy?

ERphagy receptors selectively target specific subdomains of the ER for degradation (Mochida et. al., 2015; Morishita and Mizushima, 2019). However, whether there is any selectivity for which components of the ER lumen or membrane are degraded has generally been hard to ascertain. Work in our lab used global mass spectrometry data collected throughout synchronous meiosis to identify protein degradation that correlated with the period of activity of the meiotic ubiquitin ligase Ama1, and further showed that many proteins degraded in this window were novel Ama1 targets (Eisenberg et al., 2018). Similarly, in work presented in chapter 2, I observed degradation for a large subset of ER genes late in meiosis, coincident with Atg40 expression. Follow-up experiments assessing global protein abundance throughout meiosis in WT cells compared to cells lacking one or both ERphagy receptors would help to identify the natural and receptor-specific targets of ERphagy.

3.3.3 Does ERphagy serve a meiotic quality control function?

Selective autophagy receptors have been shown to promote the degradation of aggregate-prone proteins such as proinsulin and procollagen in mammalian cells (Forrester et. al., 2019;

Cunningham et. al., 2019), and Atg40 is important for degrading ectopically expressed ATZ aggregates in yeast (Cui et. al., 2019). It will be interesting to determine whether Atg39/Atg40 are involved in the meiotic clearance of ER aggregates, and how disrupting ERphagy in this context affects the outcome of meiosis. Similar to the proposed experiments described in section 3.2.3, combining *atg39Δ* and/or *atg40Δ* mutants with chemical stress or conditions that cause ER protein aggregate accumulation will help us assess the role of ERphagy in meiotic ER quality control.

Chapter 4: Pervasive, Coordinated Protein-Level Changes Driven by Transcript Isoform Switching during Meiosis

This chapter is an adaptation of the following publication:

Cheng, Z., Otto, G.M., Powers, E.P., Keskin, A., Mertins, P., Carr, C.A., Jovanovic, M., Brar, G.A., 2018. Pervasive, Coordinated Protein-Level Changes Driven by Transcript Isoform Switching during Meiosis. *Cell,* 172, 910-923.

4.1 Introduction

The decoding of cellular information from DNA to protein determines cellular identity. Despite a strong body of knowledge of how transcription and translation are controlled, our understanding of how their regulation drives fluid changes in cell structure and function over a developmental program is rudimentary. Global studies have revealed complex patterns of gene expression regulation in contexts of cellular change, especially during developmental programs, with evidence accumulating for much more regulation than we can currently explain mechanistically (e.g., see Blank et al., 2017; Brar et al., 2012; Duncan and Mata, 2014; Jovanovic et al., 2015; Kronja et al., 2014; Peshkin et al., 2015; Tanenbaum et al., 2015) (for a review, see Liu et al., 2016). Developmental programs include embryogenesis, as well as cellular differentiation, and are characterized by rapid and unidirectional transitions in cellular state. These changes are largely thought to be driven by transcriptional activators, which turn up mRNA production to promote protein synthesis, and repressors, which turn down mRNA production and allow gene expression to be reduced. By such classical models, gene expression patterns are thus set by transcriptional regulation, which may be subsequently enhanced or dampened by post-transcriptional regulation.

Meiosis is one such conserved process of differentiation, during which chromosome and organelle segregation are coupled to gamete formation (sporulation in budding yeast). The large body of knowledge about meiotic progression in the budding yeast Saccharomyces cerevisiae and the tractability of isolating large numbers of synchronous cells makes this system a valuable model for studying gene regulation during cellular differentiation. Our previous study (Brar et al., 2012), revealed extensive formerly unrecognized transcriptional and translational regulation in meiotic cells, but the mechanisms responsible for this regulation and their impact on protein levels were unclear. We therefore performed a deeper global study here, aimed at determining the impact of transcriptional and translational regulation on the meiotic proteome. To our knowledge, the resultant dataset represents the most complete gene expression atlas to date for any developmental process.

We were surprised to identify a large subset of genes for which mRNA abundance patterns were not predictive of protein patterns despite high quality and reproducibility of measurements. Our deep dataset, enabling robust detection of both qualitative and quantitative features of gene expression, allowed us to discover that many such cases show hallmarks of a non-canonical mode of regulation that involves transcriptional toggling between two transcript isoforms encoding identical open reading frames (ORFs), one of which is a traditional mRNA that is well translated and results in protein accumulation, and one of which is an often abundant transcript that cannot be efficiently translated and results in decreased protein production (Chen et al., 2017; Chia et al., 2017). We find that this is a global regulatory mechanism that sets protein levels for over 8% of all measured genes over meiotic differentiation. By this mechanism, a transcription factor can drive synthesis of mRNA for a set of genes in concert, but this transcriptional activation results in gene expression activation in some cases and repression in others, depending on the type of transcript produced. Here, transcriptional and translational control are integrated in their regulation rather than sequential, such that the translatability of an mRNA isoform—rather than its quantity per se—is fundamental in setting protein levels through a natural and conserved developmental process.

4.2 Results

4.2.1 A Deep Dataset Reveals Meiotic Gene Regulation in Detail from Transcript to Protein

To assay the degree of change in gene regulation as cells progress through meiosis, we measured matched samples for protein levels by quantitative mass spectrometry (isobaric TMT10-plex labeling), mRNA levels by mRNA sequencing (mRNA-seq), and translation by ribosome profiling on 8 stages of natural meiotic differentiation, one vegetative exponential control in rich media, and one sporulation media-matched non-meiotic (MATa/a) control (Figures 4.1A and 4.S1). Our protein measurements were highly reproducible, both when comparing to biological replicates and to label-free quantification (LFQ; Figures 4.S1C and 4.S1D). Our mRNA-seq and ribosome profiling measurements also show high reproducibility (Figure 4.S1C).

We were able to quantify 4,464 annotated proteins at every time point, with an average coverage of 10.7 peptides/protein. We efficiently captured proteins from most cellular compartments, with few exceptions. Our mass spectrometry measurements reveal extensive protein level regulation when looking broadly at all quantified genes and suggest that most proteins are subject to active degradation in the meiotic program, with decreases in abundance observed for nearly every protein despite no dilution due to cell division, as would be seen during mitosis (Figures 4.1B and 4.S1E). Patterns of protein abundance for well-studied genes confirmed known regulation and were remarkably consistent with known function (Figures 4.S1F–4.S1K) (Zaslaver et al., 2004).

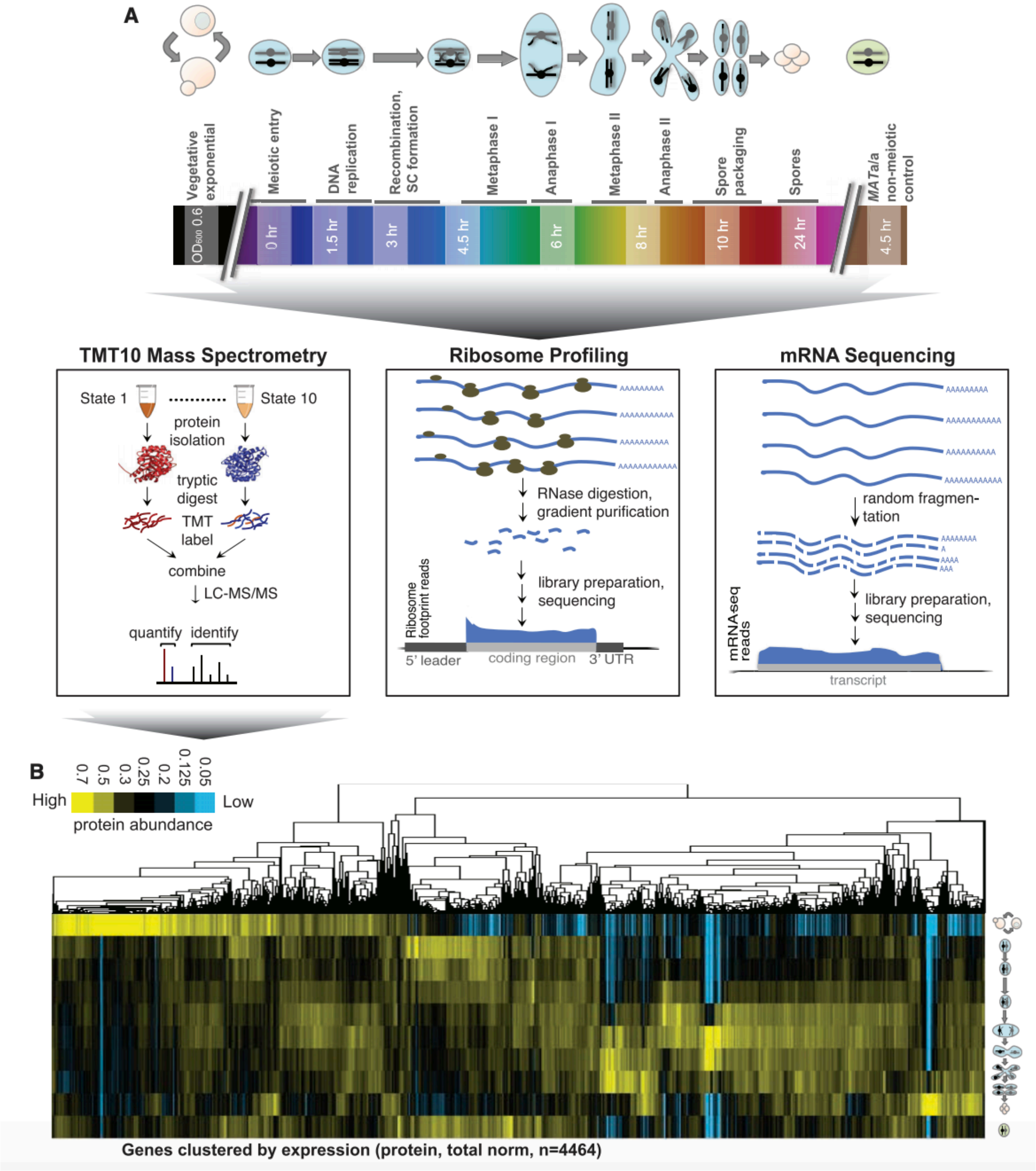

Figure 4.1 Gene Expression through Meiotic Differentiation, from mRNA to Protein (A) Matched extract was used for mRNA-seq, ribosome profiling, and quantitative mass spectrometry. (B) Hierarchical clustering of protein measurements for all quantified annotated genes (n = 4,464, columns) over all time points (rows) is shown. Total signal is normalized per column to allow comparison of patterns.

4.2.2 Discordant mRNA and Protein Levels Are Common and Reflect Biological Regulation

The degree to which regulation at the level of transcription, translation, and protein degradation drive protein levels has been a topic of extensive debate (Liu et al., 2016). We first investigated this issue in our dataset by examining the degree to which mRNA patterns predicted protein patterns. A plot of the correlation coefficients between mRNA and protein abundances revealed a positive trend, as expected based on canonical models of gene regulation (Figure 4.2A). We were surprised to see, however, a subset of genes that showed poor, even negative, mRNA: protein correlations (Figures 4.2A and 4.S2A). Given the large number of genes in this group, we tested whether they were lowly expressed, and thus the poor correlation could be driven by measurement noise. However, analyses of mean mRNA and protein abundance measurements indicated no association with mRNA to protein agreement over time (Figure 4.2B). We determined that a parallel set of mRNA-seq without polyA-selection was similar to our original mRNA-seq data, and thus that the discrepancy between mRNA and protein patterns was not an artifact of polyA tail length changes, which have been observed during developmental processes (Figures 4.S2B–4.S2D) (e.g., Subtelny et al., 2014). We concluded that the poor mRNA to protein correlation that we detect for a large subset of genes is likely to result from biological regulation.

4.2.3 A Subset of Transcriptionally Co-regulated Genes Show Discordant Protein Patterns

We hypothesized that we might be able to identify regulatory mechanisms that lead to specific cases of poor mRNA:protein concordance by focusing on a set of genes that are transcriptionally co-activated, and thus allow straightforward parallel comparison of their post-transcriptional regulation. To this end, we clustered our mRNA-seq data and observed, as previously seen, that a large group of transcripts are sharply induced in concert in late meiotic prophase (Figure S2E). Several features suggest that these genes are targets of the transcription factor Ndt80 (Xu et al., 1995): they include known Ndt80 target genes (Figures 4.2C and 4.S2E) (Chu and Herskowitz, 1998); they show a high expression correlation and a pattern matching expectations for Ndt80 induction (Figure S2E); and the consensus Ndt80 binding motif, termed the “middle sporulation element” (MSE), was strongly enriched in their promoters (Figures 4.S2F and 4.S2G) (Chu and Herskowitz, 1998).

We isolated data for the 241 of these genes that were quantified for protein and determined that, as expected, the most well characterized Ndt80 targets (including NDT80 itself and the Polo kinase-encoding CDC5) showed a sharp uptick in protein abundance that mirrors patterns of mRNA abundance. Protein levels decrease with timing similar to mRNA decreases, suggesting short protein half-lives (Figures 4.2C and 4.2D). Such high mRNA:protein agreement is seen for 150 (62%) of targets (Figures 4.2C and 4.2D). However, the protein levels for the other Ndt80 targets were not well predicted by the patterns of mRNA levels, showing, for example, markedly delayed protein accumulation (orange box in Figure 4.2C; Figure 4.2D) or protein patterns that appeared to have little relationship to transcript patterns (blue and green boxes in Figure 4.2C; Figure 4.2D). These cases showed the type of paradoxical poor mRNA:protein correlation seen to be prevalent in the full dataset (Figures 4.2A, 4.2C, 4.S2A, 4.S2H, and 4.S2I), and we proceeded to investigate their regulation in detail.

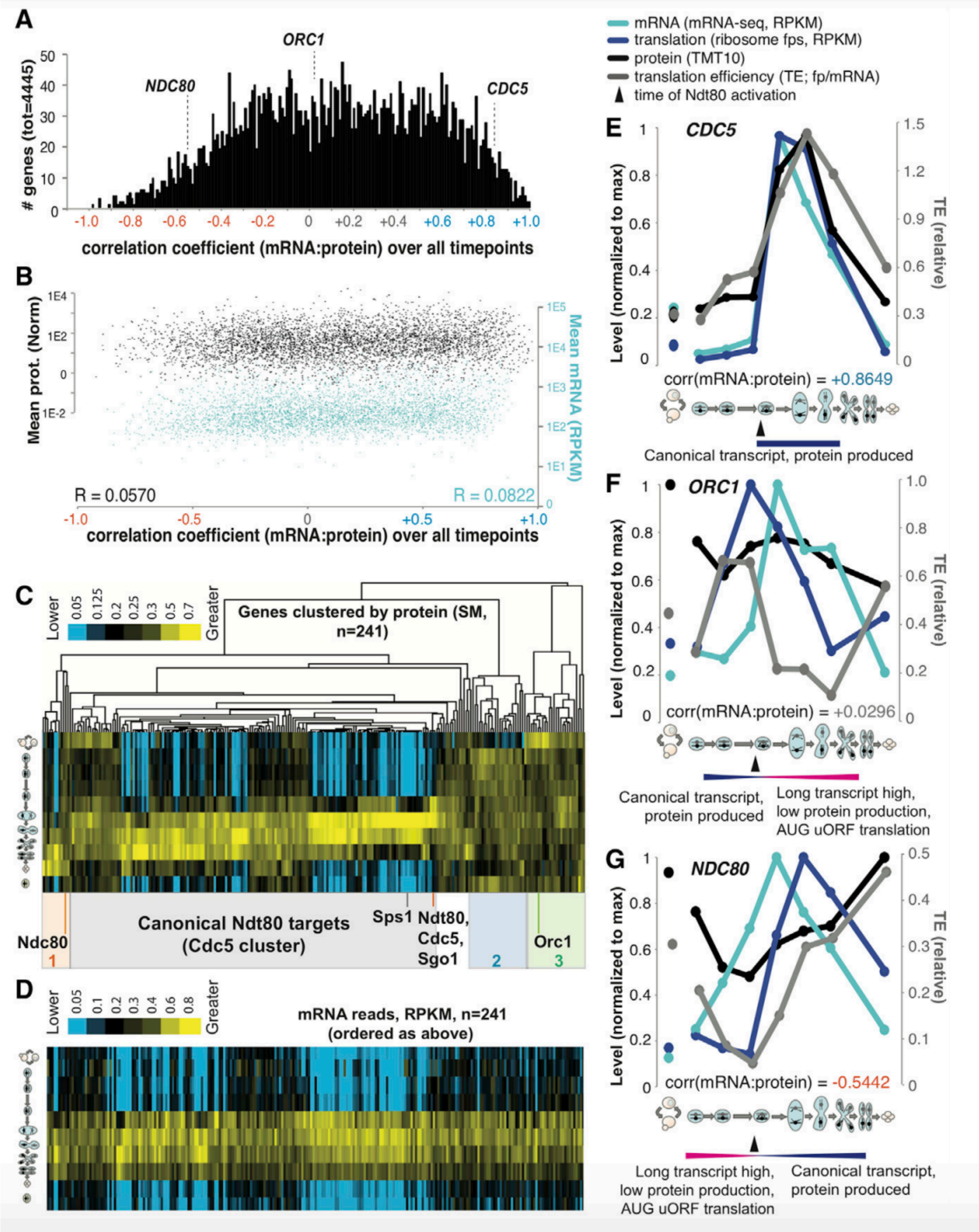

Figure 4.2. Many Genes Show a Poor Correlation between mRNA and Protein in Meiotic Differentiation that Is Associated with Alternative Transcripts (A) A histogram of the Pearson correlation coefficients between mRNA and protein abundance measurements over all time points for all genes is shown. Note the general skew toward a positive correlation and a subdistribution (centered on -0.2) with a poor correlation. (B) Mean levels of mRNA (blue) and protein (black) for each of the genes in the above distribution is shown. (C) Protein abundances for Ndt80 targets. Columns are genes, and rows are time points. Shaded boxes denote discrete clusters representing patterns of protein abundance. The gray box denotes the set of genes that show protein abundance patterns that fit well with mRNA abundances in (D). (D) mRNA abundances matched to the columns in (C). (E–G) Pink bars denote the timing of production of long transcripts, and blue bars denote the timing of production of short, canonical transcripts. mRNA, ribosome footprints, protein, and TE are plotted for canonical Ndt80 target CDC5 (E), ORC1 (F), and NDC80 (G).

4.2.4 Decoupled mRNA and Protein Levels Are Associated with Transcript Isoform Toggling

We noted that two members of this aberrant class of Ndt80 targets were ORC1 and NDC80 (Figures 4.2C and 4.S2I), encoding conserved proteins that are required for DNA replication and kinetochore function, respectively. Both genes have recently been shown to be associated with regulation involving mutually exclusive alternative transcript isoforms, so we investigated the possibility that this could account for their poor mRNA: protein agreement. A recent study showed that the 50 extended ORC1 transcript isoform results from Ndt80 activation of an upstream transcription start site (TSS), producing a transcript that is poorly translated for the ORC1 ORF and instead shows translation of several upstream ORFs (uORFs) (Brar et al., 2012; Xie et al., 2016). Comparison to a canonical Ndt80 target, CDC5 (Figures 4.2E and 4.2F), revealed that both show a robust boost in overall mRNA levels consistent with Ndt80 activation. However, in the case of ORC1, the translation of the ORF on the longer Ndt80-induced transcript is poor and thus results in a peak in translation that precedes the peak in total mRNA accumulation (Figure 4.2F) (Brar et al., 2012). In contrast, induction of higher transcript levels of CDC5 by Ndt80 results in increased translation and protein accumulation, as expected from canonical models of gene regulation (Figure 4.2E).

Regulation of the kinetochore component NDC80 shows the opposite pattern as ORC1 with respect to transcript induction by Ndt80. In the case of NDC80, a long, translationally silent transcript is present early in meiosis (Chen et al., 2017; Chia et al., 2017). The poor synthesis of Ndc80 protein from the long transcript led to it being named a "LUTI," or "long undecoded transcript isoform," and depends on the translation of AUG-initiated uORFs. The short, translatable version of the NDC80 transcript is induced later by Ndt80 (Figure 4.2G) (Chen et al., 2017; Chia et al., 2017). In our dataset, NDC80 showed a translation peak after the mRNA peak, and the gap was more prominent than we see for known cases of translational repression (Figures 4.2G and 4.S2J). We interpret this delay to reflect the switch between the abundant LUTI transcript and activation of the previously silenced proximal TSS to produce the shorter transcript. This results in mRNA and protein bursts that are out of phase by hours, which is not typical of canonically regulated genes in meiosis. Strikingly, this regulation results not just in a poor correlation between mRNA and protein abundance, but an anti-correlation (Figures 4.2G and 4.S2I).

Differences in translatability of alternative transcripts produced at ORC1 and NDC80 are apparently more important in setting protein output than the differences in overall mRNA abundance for these genes, explaining the discordance between mRNA and protein level patterns in these cases (Figures 4.2C, 4.2F, and 4.2G). Thus, the single transcription factor, Ndt80, is capable of activating transcription of three types of target genes (Figures 4.3A and 4.3C). First, CDC5 is a canonical target that promotes meiotic progression and its translation and protein levels increase in a manner that mirrors its sole, canonical transcript (Figures 4.2E, 4.3A, and 4.3C). Second, ORC1, whose protein levels decrease late in meiosis when DNA replication is complete, is silenced by Ndt80 induction through production of a longer transcript that does not efficiently produce protein and is associated with shutdown of the short, translatable transcript (Figures 4.2F, 4.3A, and 4.3C) (Xie et al., 2016). Translation efficiency ([TE]; ribosome footprints/mRNA) of the early short ORC1 transcript is high, but TE of the abundant longer Ndt80-induced ORC1 transcript is low (Figures 4.2F and 4.3A). Thus, counterintuitively, because of the scale of these differences in TE for the ORC1 isoforms, Ndt80-mediated transcriptional activation is actually associated with repressed translation for this target (Figures 4.3A and 4.3C). Third, NDC80, whose protein levels are kept low early to enable normal assembly of the meiosis I kinetochore, is required for chromosome segregation. Ndt80 drives the necessary late burst in protein levels and overcomes the silencing mediated by previous longer transcript production (Figures 4.2G, 4.3A, and 4.3C) (Chen et al., 2017; Chia et al., 2017). Taken together, Ndt80 is capable of functioning via transcriptional activation as both an inducer (CDC5 and NDC80) and as a repressor (ORC1) of protein expression, depending on the position of its binding site relative to the positions of other features of the genomic locus, including uORF sequences and the ORF start codon (Figures 4.3A and 4.3C).

4.2.5 Transcript Toggling Is Common and Reshapes the Meiotic Proteome

We noted that ORC1 and NDC80 were both members of a group of genes that we previously predicted to have alternative transcripts in meiosis, solely based on mRNA-seq data (Brar et al., 2012). Analysis of the 55 genes in the Ndt80 regulon that showed the poorest mRNA to protein correlation (< 0.4; Figure 4.S2H) revealed that this set was greatly enriched for genes with observed alternative transcripts (Figure 4.3B), suggesting that a similar transcript toggling mechanism might be responsible for other cases of discordant mRNA to protein patterns in meiosis. We sought to define simple rules that could be used to detect such regulation in an unbiased manner. We noted that an essential feature of LUTI regulation for the one mechanistically well-defined case, NDC80, was a translated AUG-initiated uORF, specifically on the long transcript isoform, which prevented ribosomes from translating the ORF (Chen et al., 2017). Downregulated ORF translation as a result of conditional uORF translation is a known mechanism, although in most reported examples, temporal control results from a change in trans-factor activity (e.g., Hinnebusch, 1993; Palam et al., 2011), while in this case, uORF translation is enabled and ORF translation disabled simply by timed production of a longer transcript that encodes uORF sequences. We previously annotated genes with meiotically translated AUGinitiated uORFs, of which 911 were quantified at the protein level here (Figure 4.3D) (Brar et al., 2012). We filtered the set of genes that show poorly correlated mRNA and protein profiles (Figure 4.2A) for meiotic translation of an AUG uORF and examined each of these loci for evidence of a clear alternative 50 extended transcript at some point in meiosis and uORF translation that was negatively associated with ORF translation (Figure 4.3D). In 380 cases, or 68% of genes for which these analyses were possible, we indeed observed evidence for regulation based on transcript toggling of differentially translated isoforms (Figures 4.3D and 4.S3A). This value changed little if discovery was conducted using mRNA-seq without single round poly-A-selection. We noted that the clusters representing aberrant protein accumulation patterns in the Ndt80 regulon were strongly enriched for these newly annotated cases of LUTI-like regulation (Figures 4.2C and 4.3E).

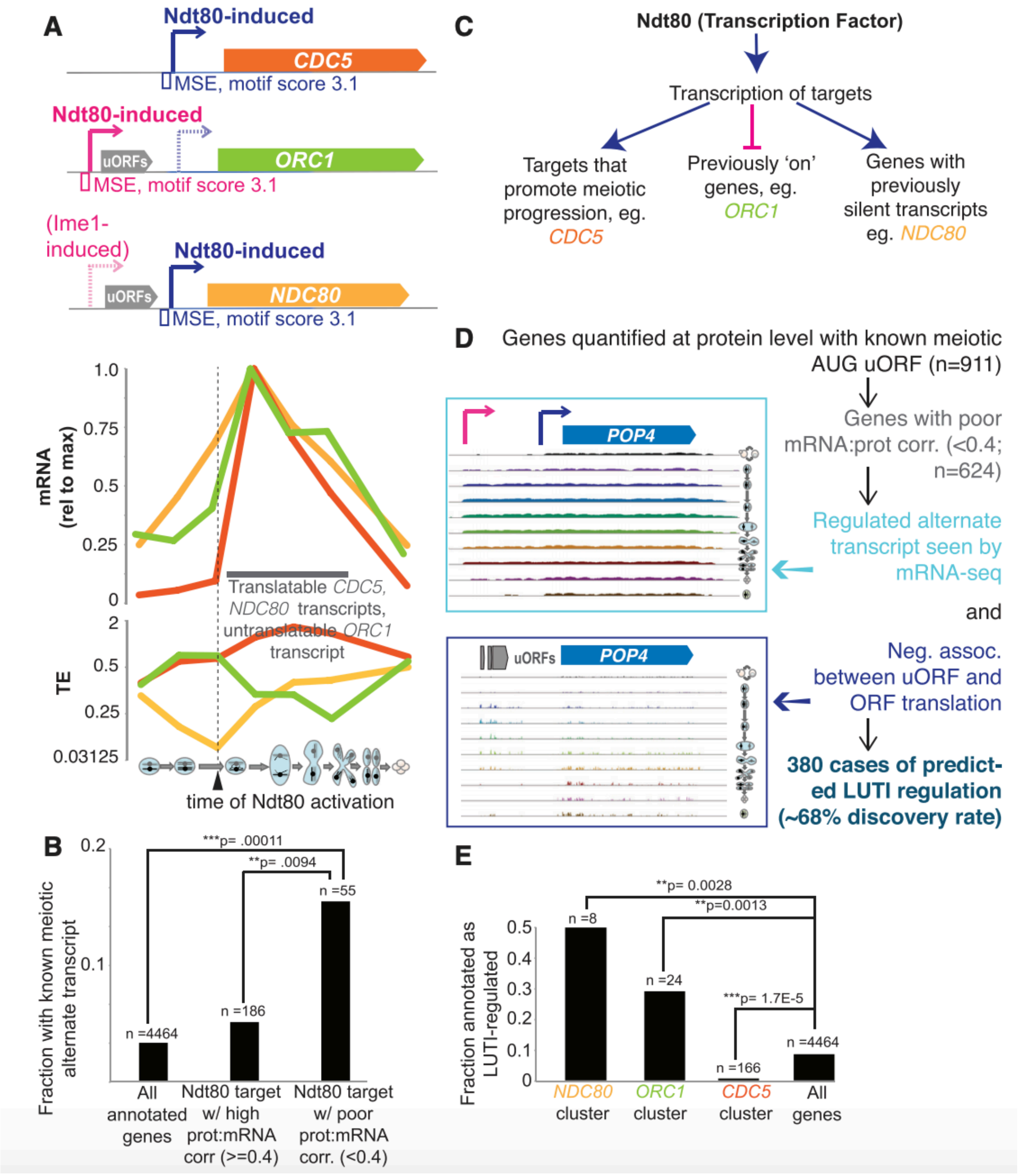

Figure 4.3. Annotation of Genes Regulated by Transcript Toggling (A) Top: transcript models are shown, along with the position of the MSE. Middle: mRNA reads (top) are plotted for CDC5, NDC80, and ORC1. Bottom, TE is plotted for these same genes. The timing of Ndt80 action corresponds with an increase in translation and TE for NDC80 and a decrease for ORC1. (B) Enrichment is shown for predicted alternative meiotic transcripts (as defined in Brar et al. [2012]) for genes in the Ndt80 regulon with poor mRNA:protein correlation (< 0.4, Pearson) in Figure S2A. **p < 0.01 by Fisher's exact test. (C) A model for Ndt80 action on three different types of targets for which it induces an abundant transcript. Canonical targets like CDC5 promote meiotic progression past pachytene. At these loci, a translatable transcript is made, resulting in rapid protein accumulation. Ndt80 induction induces an abundant and long undecoded transcript isoform (LUTI) of ORC1, which results in decreased protein levels. NDC80 is a target that was previously kept silent by a LUTI transcript. Ndt80 induces a short transcript that overcomes the silent transcript in the population and is well translated and allows protein accumulation, but at a slower rate than most canonical Ndt80 targets. (D) The description of our pipeline for LUTI identification is shown and expanded in Figure S3A. (E) Enrichment of the newly annotated LUTIs is seen in the ORC1, CDC5, and NDC80 clusters in Figure 2C. Fisher's exact test was used for statistical significance.

We expected, based on the parameters of their discovery, that the 380 proposed LUTI cases would be regulated by an NDC80/ ORC1-like mechanism involving modulation of the level of two transcripts, one of which has a long 50 leader containing at least one translated AUG uORF that results in little protein production from the canonical ORF, and one of which has a shorter 50 leader and a highly translated ORF that results in robust protein production. If this is true, we should be able to detect two transcripts that both encode the ORF, and the longer transcript should be associated with poor translation efficiency. mRNA-seq data are useful for predicting the possibility of alternative transcripts, but cannot distinguish between alternative transcripts and discontinuous, overlapping transcripts. We therefore performed northern blotting for ORFs that we predicted to show LUTI-based regulation (Figures 4.4 and 4.S4). RNA pol II mediator complex gene MED7, for example, shows two mRNA isoforms that are differentially translated for the MED7 ORF (Figures 4.4A, 4.4B, and 4.S4A). Time points with the highest total MED7 mRNA levels also showed the lowest TE and preceded a drop in protein levels, consistent with poor translation of the long transcript that was present at these times (Figures 4.4A and 4.4B).

Examination of the full set of newly proposed LUTI cases showed a variety of patterns of mRNA and protein accumulation over our time course, suggesting that several transcription factors were likely to be involved in inducing long and short isoforms at these loci (Figure 4.4C, top). In all cases, as expected, protein patterns did not resemble mRNA patterns (Figure 4.4C). We confirmed the presence of two transcript isoforms and the expected relationship with respect to TE for ten additional cases (Figures 4.4C–4.4J and 4.S4A–4.S4O). Regulation of RRD2, the gene encoding a peptidyl-prolyl-isomerase, is evident if one compares the 3 hr and 4.5 hr time points. Both show a similar amount of RRD2ORF, but the TE is higher at 4.5 hr, when we observe less RRD2LUTI isoform (Figure 4.4D and 4.S4B). Northern blots for POP7, an RNase complex component-encoding gene, and POP4, a gene encoding a fellow member of some of these complexes, showed meiotic appearance of long and poorly translated transcript isoforms at 4.5 and 1.5 hr, respectively, corresponding to low points in translation (Figures 4.4E, 4.4F, 4.S4C, and 4.S4F). DNA damage factor RAD16 primarily has a long transcript isoform through most of meiosis, corresponding with poor translation compared to vegetative cells (Figure 4.4H and 4.S4D). A long isoform of septin-encoding SHS1 was seen to peak at 6 hr into meiosis and was correlated in timing with a drop in SHS1 TE (Figure 4.4J and 4.S4E).

We noted that gene expression measurements for the 380 newly annotated LUTI cases were highly reproducible and that the unexpected relationship between protein levels was not due to our mass spectrometry approach (Figures 4.S3B–4.S3D). To further confirm our measurements, we assayed protein production from reporter constructs for three of our LUTI-regulated candidates—RAD16, SHS1, and POP4—with GFP driven by their extended promoter regions. We observed patterns that matched expectations based on LUTI-based regulation (Figures 4.4F–4.4K and 4.S4P–4.S4V). We further showed that Shs1 protein production was markedly decreased by inactivation of the predicted canonical (proximal) promoter in the reporter. Cells carrying this construct still show accumulation of the long transcript isoform, actually earlier and to a higher level than the wild-type construct, but show low levels of canonical transcript. Even at time points with high levels of the long transcript isoform present, protein levels are 30-fold lower than in cells carrying the wild-type construct (Figures 4.4K–4.4L). We conclude that, consistent with our model, the long isoform of SHS1 is not capable of efficiently supporting protein production. Based on our stringent annotation and validation approaches (Figures 4.3D, 4.4, and 4.S4), we conclude that the newly annotated cases of discordant mRNA to protein levels are indeed likely to reflect LUTI regulation of the type outlined in Figure 4.7.

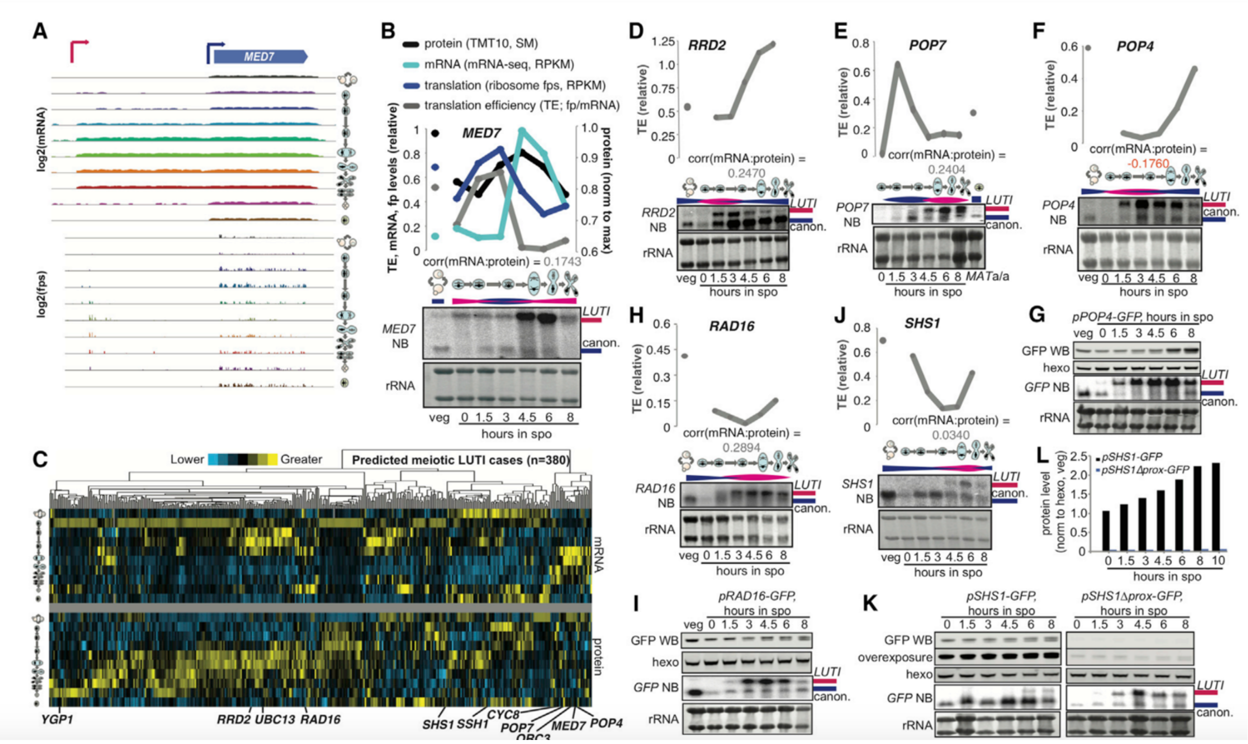

Figure 4.4. Validation of LUTI Cases Predicted by Systematic Annotation (A) mRNA-seq and ribosome profiling data are shown over all time points for the MED7 locus. Existence of a long transcript that has translated uORFs and is poorly translated for MED7 is clear at mid-meiotic time points. (B) Comparison of levels and timing between northern blots for the MED7 ORF and the mRNA-seq, translation, protein, and TE measured from matched samples shows evidence for a poorly translated long transcript isoform. (C) Z-score clustering to compare mRNA (top) and protein (bottom) patterns for each of the 380 predicted LUTIs discovered by the approach outlined in Figure 3D. Below, the positions of the genes that are investigated in more detail in Figures 4 and S4 are shown. (D–F, H, and J) A comparison of levels and timing between northern blots and the TE in matched samples shows evidence for a poorly translated long transcript for RRD2 (D), POP7 (E), POP4 (F), RAD16 (H), and SHS1 (J). Pink bars represent the presence of the long transcript, and blue bars represent the presence of the short transcript. (G, I, and K) Western blotting of a GFP reporter driven by pPOP4 (G), pRAD16 (I), and pSHS1 (K). In a paired reporter deleted for the canonical SHS1 promoter, the long transcript remains high and is increased relative to wild-type but protein production is low. Blots were run, transferred, and blotted together. (L) Quantification of the western blots in (K).

4.2.6 New LUTI Cases Show Strong Apparent Shifts in Translation Efficiency

LUTI-based regulation would be expected to result in shifts in TE over time, because TE is determined by normalizing ribosome footprint counts to mRNA counts over the ORF. Indeed, the newly proposed set of 380 LUTI-regulated genes show strong relative TE shifts compared to other genes (Figure 4.6A). It is important to note that without information about the presence of alternative transcript isoforms present at these loci, we would assume that these measurements represented temporally regulated changes in translatability for a single transcript type. In the case of genes in the NDC80 or ORC1 clusters in the Ndt80 regulon, there is evidence that transcript toggling (and TE shifts) are driven by Ndt80, either toward a translatable isoform in the NDC80 cluster or toward a translationally silent isoform in the ORC1 cluster. This conclusion is based on positioning of Ndt80 binding sites and strong similarity of our measurement patterns for these genes to others in the same clusters (Figure 4.2C, 4.2D, 4.3A, and 4.3E).

4.2.7 A Transcription Factor Can Coordinately Activate and Repress Protein Synthesis for Distinct Targets

If, as our data suggest, a single transcription factor can mediate both up- and downregulation of expression from distinct sets of target genes, this would represent a powerful mechanism for coordination in differentiation and potentially cellular transitions, more generally. To determine whether this is the case, we performed northern blotting on samples from a time course for which we had measured mRNA abundances and translation rates following timed induction of the transcription factor Ndt80 in a strain carrying GAL4 under b-estradiol (bE) control and pGAL-NDT80 (Brar et al., 2012; Carlile and Amon, 2008). We noted that three of the transcripts for which we validated transcript toggling by northern blotting, POP7, ORC3 (another origin recognition complex component) and MED7, showed similar timing for long isoform appearance following bE addition and were present in the aberrant protein level clusters among likely Ndt80 targets (Figures 4.2C, 4.2D, 4.4C, 4.4B, 4.S4F, 4.S4H, and 4.S4O). A fourth gene that we had validated by northern blotting to have two transcript isoforms, CYC8, encoding a general transcriptional co-repressor, was also present in the aberrant Ndt80 target clusters but showed the opposite pattern as the other three, with a shorter transcript isoform induced in mid-meiosis (Figures 4.2C and 4.S4N). We hypothesized that POP7, ORC3, and MED7 LUTI isoforms were driven by Ndt80, and that the CYC8 canonical isoform was driven by Ndt80, overcoming the pre-existing LUTI isoform. All four genes showed strong predicted Ndt80 binding sites adjacent to the TSS predicted to be activated (Figures 4.S5I–4.S5L). Within 1 hr of bE addition, northern blotting revealed a sharp increase in abundance of the canonical transcript for validated Ndt80 target, CDC5, a short transcript isoform of CYC8, and long isoforms of POP7, ORC3, and MED7 (Figure 4.5A). The timing of this induction was similar in all cases and corresponded with a decrease in TE of POP7, ORC3, and MED7, and an increase for canonical Ndt80 target CDC5 and CYC8 (Figures 4.5B and 4.S5E), supporting our hypothesis.

To prove that Ndt80 expression and not simply time in sporulation medium was responsible for these patterns, we arrested meiotic cells in late prophase and collected subsequent time points with or without induction of Ndt80 (Figures 4.5E and 4.S5A–4.S5D). We observed patterns of transcript appearance that matched those seen in our previous time course (Figures 4.5A and 4.5C). Moreover, matched time points at 0.5 and 1.75 hr after bE addition showed distinct patterns from those without Ndt80 induction. In the cases of POP7, MED7, and ORC3, low levels of canonical transcript remained at 1.75 hr without Ndt80 induction and long transcript was not observed (Figure 4.5C). In the case of CYC8, the canonical transcript was strongly induced in an Ndt80-dependent manner (Figure 4.5C). In all cases, analysis of our mRNA-seq data showed accumulation of overall mRNA levels to be strongly dependent on Ndt80 induction in a manner similar to that seen for canonical targets like CDC5 (Figures 4.5C, 4.5D, and 4.S5E–4.S5L). Further, we observed a sharp increase in NDT80 mRNA within 15 min of bE addition, and subsequent increases in other target transcripts, canonical (CDC5, HRR25, and CYC8) or LUTI (POP7, MED7, and ORC3), with differing degrees of induction but within a shared time span of 45 min after bE addition, supporting a model in which both of these disparate target sets are simultaneous direct targets of Ndt80 (Figures 4.5C and 4.5D).

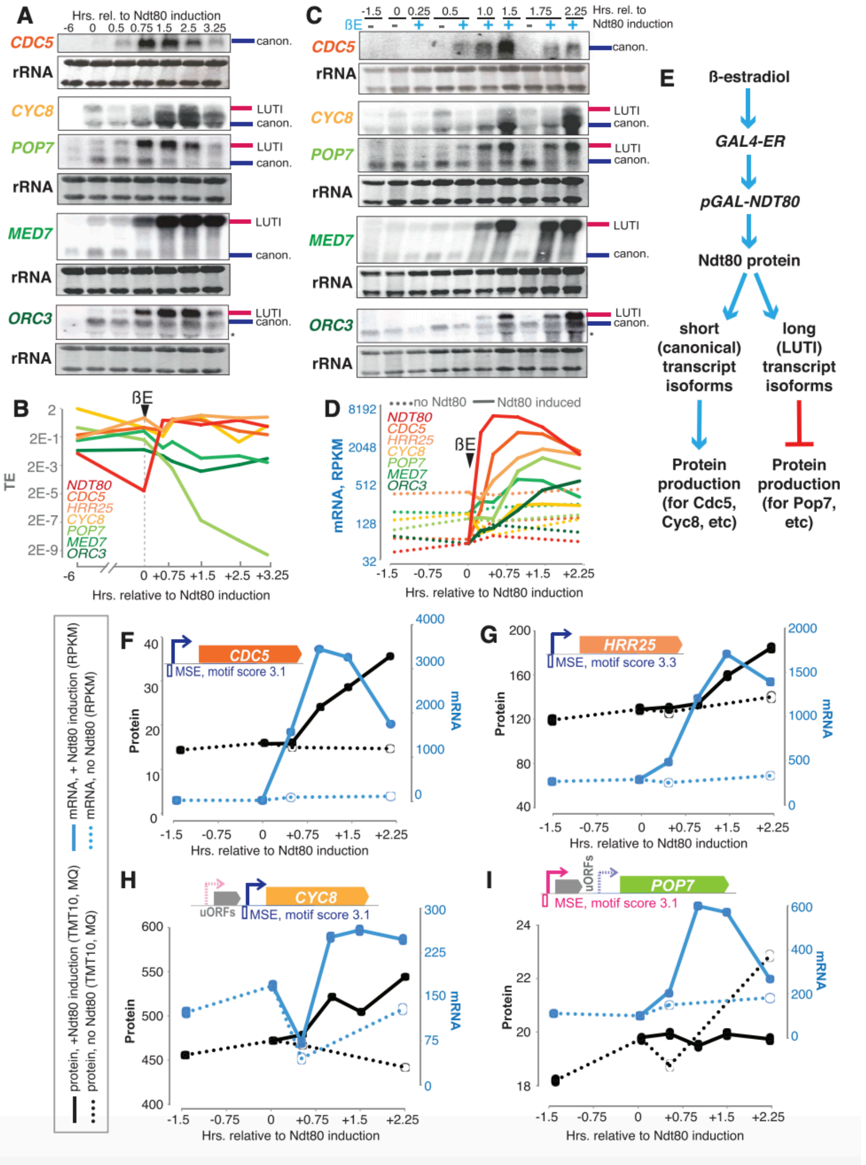

Figure 4.5. A Single Transcription Factor Coordinately Induces Long, Translationally Silent Transcript Isoforms and Canonical Transcripts, with Opposing Effects on Protein Production (A) Northern blotting reveals rapid increases in mRNA following Ndt80 induction for the canonical Ndt80 target CDC5, the canonical isoform of CYC8, and long isoforms of POP7, MED7, and ORC3. Pink and blue bars at the right of blots indicate canonical and LUTI isoforms. (B) These increases in mRNA result in decreased TE for POP7, MED7, and ORC3, whereas CDC5 and the short CYC8 isoform are better translated after Ndt80 induction. (C) Northern blotting reveals Ndt80 dependence to induction of CDC5, the canonical isoform of CYC8, and long isoforms of POP7, MED7, and ORC3. An asterisk denotes a background band. (D) mRNA abundance increases for traditional and long poorly translated Ndt80 transcript isoform targets occur with similar timing and are dependent on Ndt80. Dotted lines show mRNA abundances without addition of b-estradiol. Solid lines show measurements with b-estradiol. (E) Outline of experiments in (A) and (C) and expected effects on gene expression. (F–I) mRNA (blue) and protein (black) are shown with (solid line) and without (dotted line) Ndt80 induction for canonical targets CDC5 (F) and HRR25 (G), the canonical transcript isoform of CYC8 (H), and POP7LUTI (I). Note that induction of canonical mRNAs results in an Ndt80-dependent increase in mRNA and protein, whereas induction of the POP7 LUTI results in an Ndt80-dependent increase in mRNA but decrease in protein, relative to no Ndt80 induction.

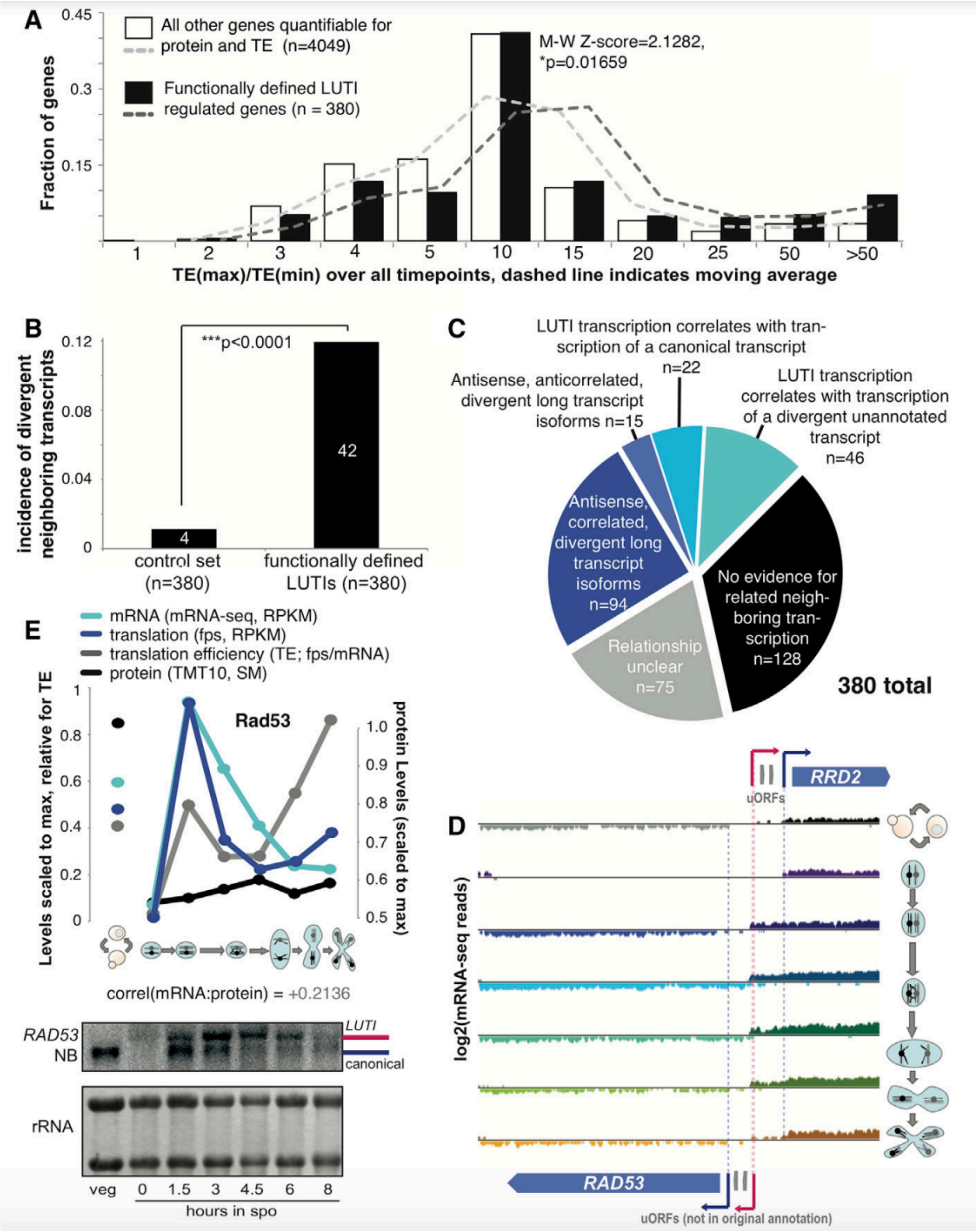

Figure 4.6. Newly Identified LUTIs Result in Strong Apparent Translational Control and Show Unusual Spatio-temporal Transcriptional Coordination (A) A histogram of the ratio between the highest and lowest TE measured is shown for the genes that we predicted to be LUTI regulated (Figure 3D), revealing a higher difference for these genes compared to others. (B) The incidence of directly adjacent and divergently oriented genes with their 50 ends close is shown for newly defined prospective LUTIs and a control set, chosen to include the 380 genes with the lowest protein:translation Pearson correlation in our dataset. (C) We examined the full set of 380 predicted LUTI cases for evidence of neighboring, correlated transcripts, with 94 of these cases oriented divergently and with apparently co-regulated long transcript isoform cases (Figure 3D). (D) mRNA-seq data for the RAD53/RRD2 locus is shown, demonstrating their divergent neighboring orientation. RAD53 shows a regulated longer transcript of the predicted size that is poorly translated. RAD53 regulation looks similar to the regulation for RRD2 (Figures 4D and 6E), but we had not previously annotated translated AUG-initiated uORFs for RAD53. (E) Translation levels, mRNA, protein, and TE for RAD53 are shown above northern blotting of matched samples.

Comparison of mass spectrometry and mRNA-seq data showed that, as expected, Ndt80 induction resulted in accumulation of first mRNA, then protein for canonical Ndt80 targets, including Cdc5 and Hrr25 (Figures 4.5F and 4.5G). We were also able to detect Ndt80-dependent protein accumulation for Cyc8, which showed a similar pattern to these targets (Figure 4.5H). Most interestingly, we quantified protein for Pop7 (Figures 4.4E, 4.5A, and 4.5C), and observed that although overall POP7 mRNA levels were drastically increased following and dependent on Ndt80, this condition resulted in slight decreases in protein levels with Ndt80 induction (Figure 4.5I). In contrast, without Ndt80 induction, Pop7 protein levels were seen to increase in this same time frame, suggesting that induction of the long POP7 isoform by Ndt80 "turns off" pre-existing default protein production from this gene (Figure 4.5I). This result shows that Ndt80 induction results in coordinate upregulation and downregulation of protein production of distinct sets of genes despite increased mRNA abundance for both types of targets (Figure 4.5E).

4.2.8 New LUTI Cases Show Evidence of Spatio-temporal Co-regulation

For most of the 380 LUTI cases, as is true of most canonically regulated genes that are expressed during meiotic differentiation, we do not know the transcription factor(s) responsible for their induction. We identified a signature in our new annotations, however, that supports the involvement of regulated differential transcriptional control in many cases. Among the 380 proposed LUTI-regulated genes, 42 of them—far more than would be expected by chance—were in adjacent genomic locations and in a divergent orientation such that the 50 ends were close (Figure 4.6B).

We wondered if this enrichment for genomically neighboring positions suggested coordinated transcriptional regulation. To investigate this possibility in greater depth, we examined mRNA read patterns over time and space in the genomic vicinity of each of our 380 predicted LUTI cases for evidence of their co-regulation with any stable neighboring transcripts. In approximately half of the cases, we observed clear evidence for co-regulation in time and genomic space (Figure 4.6C). One of these was RRD2, which we had annotated as showing LUTIbased regulation, and which appeared to be spatio-temporally co-regulated with production of a long version of the RAD53 mRNA (encoding a DNA damage kinase, CHK2 in humans) that we had not identified as a candidate for LUTI-based regulation (Figures 4.3D, 4.4D, and 4.6D). We noted that both RRD2 and RAD53 showed short transcripts at similar times and 50 extended transcripts at similar times, and the positions of 50 ends of the longer transcripts were in close proximity (within 50 nt), suggesting transcriptional coregulation. We confirmed the presence of the predicted longer version of the RAD53 transcript, and noted that the ORF appeared to be poorly translated when two AUG-initiated uORFs were translated (Figures 4.6D, 4.6E, and 4.S4G), although we had not previously annotated translated AUG-initiated uORFs for this gene. 94 of our set of 380 LUTI-based regulation candidates showed evidence for spatio-temporally coordinated co-regulation of long transcript isoforms like that seen for RAD53/RRD2 (Figures 4.6C and 4.S6B). We further observed several other patterns that suggested neighboring transcript co-regulation (Figure 4.S6), including cases in which LUTI transcription was correlated in time and genomic position with transcription of a canonical transcript for a gene with no evidence for LUTI-type regulation

(Figures 4.S6G–4.S6I) (Xie et al., 2016). We noted that in all such cases, the 50 transcript ends were either overlapping or close (within 100 nt), suggesting that co-regulation of two long transcript isoforms, or a LUTI and another transcript, may be driven by a change in chromatin structure and/or a shared transcription factor at a bi-directional promoter (Xie et al., 2016). The majority of canonical Ndt80 transcriptional targets (Figure 4.2D) also show divergent and spatio-temporally regulated transcription, consistent with this feature as a hallmark of transcriptional activation (data not shown; examples in Figures 4.S6C and 4.S6I) (Bussemaker et al., 2001).

The discovery that RAD53 showed LUTI-like regulation but was missed by our annotation approach led us to investigate if our requirement for previously annotated uORFs (Figure 4.3D) might result in other false negative cases. To investigate this possibility, we searched for genes that showed a poor mRNA:protein correlation that did not have annotated uORFs and determined whether there was evidence for translational regulation associated with an alternative transcript at the locus. We identified several cases that did appear to be associated with AUG-initiated uORF translation (Figures 4.S7A–4.S7D). In the cases of ADH1 (encoding alcohol dehydrogenase) and CTT1 (encoding catalase T), like RAD53 above (Figures 4.6D and 4.6E), the uORF in question was one that we had annotated as translated but not previously annotated within the leader of a canonical gene (Brar et al., 2012). It seems likely that there will be cases in which extended 50 leaders suppress translation independent of AUG-initiated uORF translation, but we have yet to confirm such an example. Nonetheless, cases like RAD53, ADH1, and CTT1, which our systematic approach (Figures 4.6D, 4.6E, and 4.S7A–4.S7D) failed to identify as LUTI-regulated, suggests that a regulatory mechanism in which transcript toggling drives protein levels is likely to be an even greater contributor to the dynamic content of the meiotic proteome than predicted by the evidence for 380 cases presented here (Figure 4.3D).

4.3 Discussion

We find that gene regulation based on transcript toggling, a mechanism recently dissected in detail for a single gene (Chen et al., 2017; Chia et al., 2017), is a general mode of gene regulation during meiotic differentiation in yeast, determining the protein levels for at least 8% of measured genes (Figure 4.7A). This regulatory mechanism, in which transcript isoform identity rather than transcript quantity drives protein accumulation, dramatically remodels the meiotic proteome relative to what would be expected from traditional models of gene regulation. Our results suggest that a substantial subset of the meiotic transcriptome contains protein coding regions that are not decoded by the ribosome into protein, and that this subset can change over time as part of this developmental program. As a result, total mRNA levels may have no relationship to protein levels for many genes in a changing cell.

We base our general model of this non-canonical regulation (Figure 4.7) on observations from our dataset and on recent studies of NDC80 (Chen et al., 2017; Chia et al., 2017). In short, the relative levels of two transcription factors may determine the relative levels of two transcripts for these loci. The longer transcript does not result in efficient protein synthesis due to translation of interfering uORFs, while the short transcript does (Figure 4.7A). In the case of NDC80, transcription from the distal TSS promotes cis-silencing by epigenetic modification at the proximal TSS, a key aspect of the toggling observed between the two isoforms. This may be true for many genes in our new set, as well, based on the inverse pattern generally seen for the two isoforms (in particular, Figures 4.4B, 4.4E, 4.4F, 4.4H, 4.S4O, and 4.S7C). LUTI-based regulation is analogous in many ways to transcriptional repressor-based regulation (Figure 4.7B), in that in general in both cases, two trans-factors control the capacity for protein synthesis of a gene. In the latter case, however, mRNA levels would be predictive of protein levels, while in the LUTI case, this may not be true.

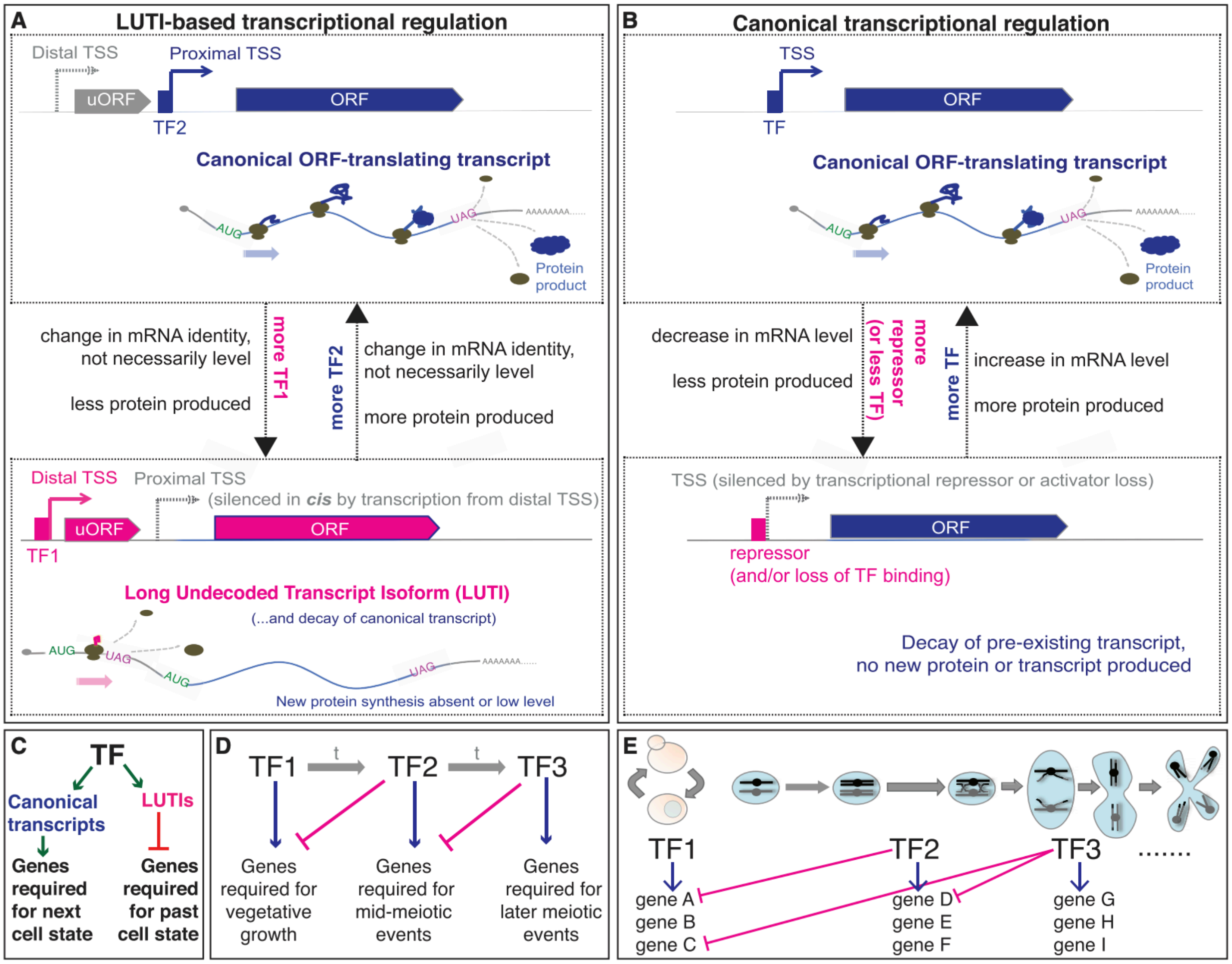

Figure 4.7. A Model for the Control of Protein Levels by Transcript Isoform Toggling in Meiosis (A) A subset of genes is encoded by two transcript isoforms, differing in their 50 end. These isoforms result from two transcription start sites (TSSs), and the choice between these two TSSs may be controlled by the relative levels of the two transcription factors (TF2 and TF1) that can bind the proximal and distal TSS, respectively. If TF2 binds the proximal TSS, a canonical transcript is produced with a short 50 leader that is well translated and results in protein accumulation. If TF1 accumulates, it binds the distal TSS and produces a longer transcript at this locus. This transcript includes the sequence for the encoded gene, but ribosomes do not decode this region into protein due to repressive uORFs in the extended leader region. Analysis of one case shows that transcription of the LUTI can silence the proximal TSS in cis (Chia et al., 2017). The difference in translatability of the two transcripts is more important than the abundance of transcript at these loci. Further, by this model, TF2 ultimately activates gene expression and TF1 ultimately represses gene expression. (B) In contrast, canonical transcriptional repression involves either loss of binding of an activating transcription factor or the additional presence of a repressor molecule. (C) In a developmental process, the LUTI mechanism can enable coordinated activation of genes required for the next cellular state and repression of genes involved in the past cellular state. (D) This mode of regulation allows a relay of sequential activation and repression to time protein levels to a window of action. (E) The modular nature of LUTI regulation allows genes to be turned on an off in a coordinated manner for windows of different lengths of time. For example, gene A protein production would be turned on by TF1 and turned off by production of a LUTI by TF2. Gene C would also be turned on by TF1, but would stay on longer, until shut down by TF3.

Several factors lead us to believe that our annotations are underestimating the total incidence of LUTI-based regulation. First, we identified the set of 380 cases reported here by limiting our search pool to the set of genes that we measured to show a poor mRNA:protein correlation (Figures 4.2A and 4.3D). This requires that we searched for and captured the protein by mass spectrometry, which excludes 2,200 canonical genes and thousands of noncanonical, shorter genes (Brar et al., 2012; Ingolia et al., 2014). Second, our follow-up analysis of the mRNA-seq data and ribosome profiling data for evidence of alternative isoforms and uORF translation require high enough expression levels for such effects to be clear. Third, the 50 extension must be long enough that a shift in transcript boundary is apparent in the mRNA-seq data. Fourth, our ability to see transient isoforms is limited by population synchrony. The case of CTT1 is informative, as the 8 hr time point shows a mixture of the two isoforms which is visible by northern blotting but was not immediately evident from the mRNA-seq data alone (orange, Figures 4.S7C and 4.S7D). Finally, our LUTI prediction pipeline required previous annotation of a translated AUG-initiated uORF, but we are aware that our uORF annotations are incomplete (demonstrated for RAD53, ADH1, and CTT1; Figures 4.6E and 4.S7A–4.S7D) and also because there may be alternate mechanisms by which a longer 5’ leader could repress translation relative to a shorter one.

Why is this mode of regulation so common in meiotic cells? It seems effective at driving up- and downregulation of protein levels without the need for a dedicated trans-factor for transcriptional repression. This process instead allows repurposing of existing transcription factors for a new function, dependent on cis-sequence evolution only. It also appears to be readily reversible and tunable, resulting in ramping up and down of protein levels that may be important to the timing in developmental processes, which involve a series of switches in cell state (Figures 4.2C and 4.7C–7E) (Chen et al., 2017; Chia et al., 2017). Further, the use of a common set of transcription factors to traditional transcriptional upregulation provides an efficient solution for coordination of up- and downregulation of sets of protein targets (Figures 4.2C, 4.3C, and 4.7C–4.7E). This feature is ideal for executing coordinated cell state changes, over biological and evolutionary time.

With the recent ability to quantify gene expression globally at multiple levels, there has been intense interest in ascertaining the relative importance of different stages of gene regulation (Liu et al., 2016). Our work suggests that a focus on relative quantitative contributions may cause us to miss important qualitative changes. A single transcription factor can activate protein expression or repress protein production, a distinction based not on whether an mRNA is induced, but rather on the position of the TSS relative to the ORF start codon and the resultant translatability of the specific isoform induced (Figure 4.2C, 4.3A, 4.3C, and 4.7). A significant implication is that inferring protein production based on mRNA abundances may not just give an incomplete picture; rather such measurements may lead to completely false conclusions about protein levels. Similarly, our data show that identification of alternative transcript isoforms alone is not enough to infer differences in translation. We identify cases in which regulated 5’ transcript extensions are seen, even accompanied by uORF translation, but for which we cannot detect an effect on translation or protein production (example in Figures 4.S7E–4.S7F). The basis for the difference between these cases and LUTI-based regulation remains unclear and suggests that there are important features of this regulation that are yet to be uncovered.

Our ability to systematically identify many cases of a new mode of gene regulation was enabled by the depth of measurements as well as the time-resolved and parallel nature of them. A dataset with few time points or without matched measurements of mRNA and protein may not have allowed sensitive identification of the anti-correlations between mRNA and protein levels. Without matched TE measurements, we would not have been able to determine the basis for these poor correlations. Our analyses were also enabled by the apparently relatively short protein half-lives in meiotic cells relative to our time point spacing (Figure 4.1B). A short protein half-life is a feature that one would expect to generally see during processes involving rapid unidirectional change in cellular state and this feature was important in revealing both the low mRNA:protein correlation among LUTI-regulated genes and the high mRNA:protein correlation for traditionally regulated genes (Figures 4.2A and 4.2E). Given recent evidence of widespread alternative TSSs in mammalian cells and for variant translation efficiencies of alternative mammalian transcripts (examples in Floor and Doudna, 2016; Wang et al., 2016), along with the high degree of conservation of some of the genes for which we observe LUTI-based regulation, it seems likely that this mode of integrated regulation may be used outside of yeast. A recent study that compared mRNA and protein levels over embryonic development in frogs determined that a large set of genes showed a poor mRNA:protein correlation over time (Peshkin et al., 2015). Some of those cases were deemed a result of measurement noise, but it is possible that a LUTI-based mechanism might explain a remaining subset of such cases.

We suggest that thinking of transcription and translation as independent levels of regulation in eukaryotes may obscure important principles in gene regulation. Widespread use of alternative TSSs has been seen by genome-wide approaches (e.g., Aanes et al., 2013; Pelechano et al., 2013). Similarly, it is clear that 5’ leader identity is key in setting translation efficiency (examples in Floor and Doudna, 2016; Hinnebusch et al., 2016; Law et al., 2005; Rojas-Duran and Gilbert, 2012; Wang et al., 2016). The connection between these two concepts—that a regulated toggle in TSS usage driven by the relative activity of two transcription factors can determine whether a protein-decodable or non-decodable transcript is made and that this mechanism is employed pervasively in setting protein levels during cell-fate determination—has not been previously apparent. By this mechanism, timed changes in the transcript pool composition for a large set of genes, rather than their levels, are key in driving the changing composition of the proteome through cellular differentiation. Further, the concept of simultaneous up- and downregulation of distinct sets of genes by a single transcription factor provides a previously unrecognized and elegant solution to the problem of precisely coordinating increases and decreases in protein expression during a developmental program.

4.3 Methods

4.3.1 Yeast material and growth conditions

All experiments were performed using diploid Saccharomyces cerevisiae strains of the SK1 background. All are MATa/alpha except Br-U¨ n5805, an SK1 strain that is wild-type except for two copies of the MATa locus and no MATalpha locus (van Werven et al., 2012). This latter strain will not undergo meiosis, even when stimulated with conditions that should induce it. For major meiotic time courses, Br-U¨ n strain 1362 (equivalent to gb15 in Brar et al., 2012) was inoculated into YEPD overnight, then diluted to OD6000.2 into buffered YTA and grown for 12 hours. Cells were washed in water and resuspended in 250 mL sporulation media supplemented with 0.02% raffinose. Cells were incubated, with shaking at 30C. For vegetative growth, strains were incubated with shaking at 30C.

4.3.2 Sample collection

Meiotic samples for main experiment were collected at the time points presented in Figure 1, as in Brar et al. (2012), using 1 minute cyclohexamide treatment, filtration and flash freezing in liquid Nitrogen in two portions, 90% for ribosome profiling, 10% for total RNA isolation. Vegetative exponential samples were collected after growth of 750 mL in YEPD to OD6000.6 from a dilution to OD6000.05. MATa/a samples were treated as the meiotic, but only one sample was collected, at 4.5 hours. 3 mL flash frozen buffer was added to ribosome profiling aliquot (also to be used for mass spectrometry) of the standard ribosome profiling composition (20mM Tris pH8, 140mM KCl, 1.5mM MgCl2, 100ug/ml cycloheximide, 1% Trition X-100) supplemented with 2ug/ml Aprotinin, 10ug/ml Leupeptin, 1mM PMSF, 1:100 PIC2, 1:100 PIC3 (both Sigma inhibitor cocktails). Samples were lysed by Retsch mixermilling (6x 3 minute rounds at 15 Hz). Resulting powder was thawed, spun once at 4C for 5 min at 3000 RCF, sup was removed and spun at 20,000 RCF at 4C for 10 minutes. Extract was aliquoted in 200ul portions and flash frozen. Identical extract was used for ribosome profiling and mass spectrometry.

4.3.3 Ribosome profiling

Ribosome profiling was performed as described previously in Brar et al. (2012). The detailed protocol is identical to Ingolia et al. (2012) except that no linker ligation was used and instead ribosome footprints were polyA-tailed to mark the 30 ends. In short, samples were treated with RNase I (Ambion) at 15 U per A260 unit of extract for 1 hour at room temperature. Samples were then loaded onto sucrose gradients (10%–50%) and centrifuged for 3 hr. at 35,000 rpm at 4C in a SW41Ti rotor (Beckman). 80S/monosome peaks were collected using a Gradient Station (BioComp). RNA was extracted using the hot acid phenol method, RNA was size selected from a polyacrylamide gel, dephosphorylated, poly-A-tailed, subjected to rRNA subtraction, RT-PCR, circularization, and PCR. The enzymes used were PNK (NEB, lot 0951602), E.coli polyA polymerase (NEB, lot 0101309), Superscript III (Thermo, lot 1752971), Circ Ligase (Epicenter), Phusion polymerase (NEB). Oligos used were oCJ200-oligodT for reverse transcription, oNTI231 and aatgatacggcgaccaccgagatcggaagagcacacgtctgaactccagtcac-barcode-cgacaggttcagagttc index primers for PCR, all also PAGE purified from IDT, with the barcodes of six nucleotides in length. Sequencing was done for both reads with standard Illumina oligos.

4.3.4 mRNA sequencing

The protocol followed was identical to above, except for the following: single round poly-A-selected RNA was alkaline fragmented and size selected to 30-50 nt. Fragments were subjected to an identical library prep pipeline as the footprints, but no selective rRNA subtraction round was used. A parallel set of RNA was sequenced that excluded the poly-A-selection step, but sequencing depth of mRNA was much lower, as expected, and agreement with the polyA-selected data was high (Figure S2B). We thus use the polyA-selected mRNA data for all analyses presented.

4.3.5 Sequencing

All samples were sequenced on an Illumina HiSeq 2500, 50SRR, with multiplexing, at the UC-Berkeley Vincent Coates QB3 Sequencing facility.

4.3.6 Meiotic staging

Progression of cells through meiosis in each time course included here was determined by quantification of nuclear morphology by DAPI staining (Vectashield, Vector) of ethanol-permeabilized cells adhered to a polylysine-treated glass slide. Prior to anaphase I, cells show mononucleate morphology, at and after anaphase I and before anaphase II, cells show binucleate morphology, during and following anaphase II, cells show tetranucleate morphology. All time courses were also assessed at 24 hours after transfer to sporulation media by brightfield microscopy to ensure high efficiency of spore formation, which we typically observe at 90%. The Ndt80 induction experiment (Figures 5C–5I and S5) was also staged using indirect immunofluorescence of alpha-tubulin, using a rat anti-tubulin antibody (Serotec) at a dilution of 1:200 and anti-rat FITC antibody (Jackson ImmunoResearch Laboratories) at 1:100. Fluorescent microscopy was done on a DeltaVision microscope with a 100X objective.

4.3.7 Ndt80 induction

Cells carrying GAL-NDT80 and pGPD1-GAL4(848).ER constructs (as described in Carlile and Amon, 2008) were introduced to sporulation medium and incubated with shaking at 30C for 5.5 hours. At that time, b-estradiol was added to half of the culture at a concentration of 1 mM. The Northern blotting of the Ndt80 release experiment in Figures 5A and 5B was done using mRNA extracted for this manuscript from frozen pellets archived from the experiment published in Brar et al. (2012). Data in Figure 5B is based on analysis of matched translation and mRNA-seq data from Brar et al. (2012).

4.3.8 Strain construction

Reporter strains used for western blotting pictured in Figure 4 were constructed by amplification of promoter regions, including 200 nt upstream of 5’ most mRNA-seq read observed at any time point in our dataset. These regions were cloned upstream of a plasmid encoding eGFP to create (pPOP4-eGFP), pUB1288 (pRAD16-eGFP), and pUB1290 (pSHS1-eGFP). pUB1288 was mutated to remove the 50 nt region containing the proximal promoter to create pUB1324 (pSHS1Dprox-eGFP), using the Q5 Site-directed mutagenesis kit (New England Biolabs). All constructs were integrated into the genome by amplification TRP1 on both sides and integration into this locus in a strain carrying a trp1::hisG allele.

4.3.9 Western blotting

Western blotting was performed using a standard trichloroacetic acid (TCA) protocol, exactly as described in Chen et al. (2017), except using a mouse anti-GFP JL8 antibody (Clontech). In short, 5ml of meiotic cells in culture (or 2ml vegetative) were collected and incubated with 5% TCA for at least 10 minutes at 4C. Cells were centrifuged for 2 min. at 20,000 rcf. and supernatant was aspirated. Cells were washed with acetone and pellets dried for at least 2 hours. Cell extract was made by addition of TE, supplemented with 3 mM DTT and protease inhibitors (Roche), and 1 volume of acid-washed glass beads. Tubes were agitated for 5 minutes, after which 3X SDS sample buffer was added, samples were boiled for 5 minutes, centrifuged for 5 min at 20,000 rcf. 8 mL supernatant was loaded onto Bis-Tris acrylamide gels. Gels were transferred using a Turboblot system (BioRad). Primary anti-GFP antibody dilution was 1:2000, anti-hexokinase was 1:12,000, secondary (Li-Cor) was 1:20,000. Primary antibody incubation was overnight, secondary for 1-2 hours. Blots were visualized using a Li-Cor system.

4.3.10 Northern blotting

8ug of total RNA from time courses (Figure 1A) was loaded onto either 1% or 1.5% Formaldehyde agarose gels, and run at 170V for 2.5 hours. A DNA ladder was also loaded to assess rough sizing. The gel was transferred onto a nylon membrane (Hybond, GE), crosslinked, and methylene blue stained for loading. The blot was blocked with Northern Max Ultrahyb buffer (Ambion) at 68C for 30 minutes. The probe was generated by PCR of wild-type genomic yeast DNA and in vitro transcription (MaxiScript T7 kit, Thermo) using alpha-UTP and all other nucleotides cold. The blot was incubated with the probe overnight at 65C, washed as recommended by NorthernMax kit (Ambion), and visualized using Typhoon phosphor-imaging.

4.3.11 Mass spectrometry

Deep coverage meiotic time course proteomics dataset generated by TMT-labeling and sample fractionation

Proteins were precipitated by adding -20C cold acetone to the lysate (acetone to eluate ratio 10:1) and overnight incubation at -20C. The proteins were pelleted by centrifugation at 20000xg for 15min at 4C. The supernatant was discarded and the pellet was left to dry by evaporation. The protein pellet was reconstituted in 200 mL urea buffer (8M Urea, 75mM NaCl, 50mM Tris/HCl pH 8.0, 1mM EDTA) and protein concentrations were determined by BCA assay (Pierce). 40 mg of total protein per sample were processed further. Disulfide bonds were reduced with 5mM dithiothreitol and cysteines were subsequently alkylated with 10mM iodoacetamide. Samples were diluted 1:4 with 50mM Tris/HCl (pH 8.0) and sequencing grade modified trypsin (Promega) was added in an enzyme-to-substrate ratio of 1:50. After 16h of digestion, samples were acidified with 1% formic acid (final concentration). Tryptic peptides were desalted on C18 StageTips according to Rappsilber et al. (2007) and evaporated to dryness in a vacuum concentrator. Desalted peptides were labeled with the TMT10plex mass tag labeling reagent according to the manufacturer's instructions (Thermo Scientific) with small modifications. Briefly, 0.5 units of TMT10plex reagent was used per 40 mg of sample. Peptides were dissolved in 50 mL of 50mM HEPES pH 8.5 solution and the TMT10plex reagent was added in 20.5 mL of MeCN. After 1h incubation the reaction was stopped with 4 mL 5% Hydroxylamine for 15min at 25C. Differentially labeled peptides were mixed for each replicate (see mixing scheme in Table S8) and subsequently desalted on C18 StageTips (Rappsilber et al., 2007) and evaporated to dryness in a vacuum concentrator.

To reduce peptide complexity and achieve deeper proteome coverage, samples were then separated by basic reversed-phase chromatography as described in Mertins et al. (2013). Briefly desalted peptides were reconstituted in 20mM ammonium formate, pH 10, (900 ml) and centrifuged at 10,000g to clarify the mixture before it was transferred into autosampler tubes. Basic reversedphase chromatography was conducted on a Zorbax 300A˚ Extend-C18 column, using an Agilent 1100 Series HPLC instrument. The separations were performed on a 2.1mm. 150mm column (Agilent, 3.5 mm bead size). Prior to each separation, columns were monitored for efficient separation with standard mixtures containing 6 peptides. Solvent A (2% acetonitrile, 5mM ammonium formate, pH 10), and a nonlinear increasing concentration of solvent B (90% acetonitrile, 5mM ammonium formate, pH 10) were used to separate peptides by their hydrophobicity at a high pH. We used a flow rate of 0.2ml/min and increased the percentage of solvent B in a nonlinear gradient with 4 different slopes (0% for 1min; 0% to 9% in 6min; 9% to 13% in 8min; 13% to 28.5% in 46.5min; 28.5% to 34% in 5.5min; 34% to 60% in 23min; 60% for 26min). Eluted peptides were collected in 96 well plates with 1min (= 0.2 ml) fractions. Early eluting peptides were collected in fraction "A," which is a combined sample of all fractions collected before any major UV-214 signals were detected. The peptide samples were combined into 12 to be used for proteome analysis. Subfractions were achieved in a serpentine, concatenated pattern, combining eluted fractions from the beginning, middle, end of the run to generate subfractions of similar complexities that contain hydrophilic as well as hydrophobic peptides. For high-scale proteome analysis every 12th fraction was combined (1,13,25,37,49,61; 2,14,26,38,50,62…). Subfractions were acidified to a final concentration of 1% formic acid and desalted on C18 StageTips according to Rappsilber et al. (2007). LC-MS/MS analysis on a Q-Exactive HF was performed as previously described (Keshishian et al., 2015).

All mass spectra were analyzed with the Spectrum Mill software package v4.0 beta (Agilent Technologies) according to Mertins et al. (2013) using the yeast Uniprot database (UniProt.Yeast.completeIsoforms.UP000002311.20151220; strain ATCC 204508 / S288c). For identification, we applied a maximum FDR of 1% separately on the protein and peptide level and proteins were grouped in subgroup specific manner. We required at least 1 spectral count from a unique peptide for protein identification and for protein quantification per replicate measurement. 72 proteins were identified and quantified by one spectral count in each replicate, 231 proteins by one count in one replicate and > 1 in the other replicate and 4161 proteins by > 1 spectral count in both replicates. Note that the S288C UniProt dataset was used because we are not aware of an equivalently complete protein dataset for SK1, and due to poorer sequencing depth and annotation of this genome relative to the reference, our attempt to create one excluded many proteins. This presumably caused us to miss capture of some proteins for which the quantifiable peptides are not identical in the two strains, but should not cause artifacts in our correlation measurements, because all measurements are relative among time points.

Finally, we normalized the Spectrum Mill generated intensities the following way. For the "total norm" values in Table S3, we normalized the Spectrum Mill generated intensities such that at each condition/time point the TMT intensity values added up to exactly 1,000,000, therefore each protein group value can be regarded as a normalized microshare (we did this separately for each replicate for all proteins that were present in that replicate TMT mix). For the "MS1 total" values in Table S3, we used these normalized "total norm" values to assign each protein group of a TMT labeled sample its proportional fraction of the Spectrum Mill generated "total MS1" intensities, based on its labeling channel specific "total norm" intensity relative to the sum of the "total norm" intensities of all labeled channels for the corresponding protein group. For the "MS1 mean" values in Table S3, we used these normalized "total norm" values to assign each protein group of a TMT labeled sample its proportional fraction of the Spectrum Mill generated "mean MS1" intensities, based on its labeling channel specific "total norm" intensity relative to the sum of the "total norm" intensities of all labeled channels for the corresponding protein group.

Note: In order to compare protein group specific intensity values between the TMT quantified meiotic time courses and our control label free quantified (LFQ) meiotic time course (replicate 2 only, missing the "25h spores" time point only), we analyzed the above generated data also with MaxQuant (version 1.6.0.16), as that was the program of choice for our LFQ measurements. The same parameters were applied as for the LFQ data analysis (see below). Each protein group of a TMT labeled sample got its proportional fraction of the MS1 based LFQ intensities based on its labeling channel specific TMT MS2 intensity relative to the sum of TMT MS2 intensities of all labeled channels for the corresponding protein group. Afterward we normalized these fractional MS1 LFQ intensities such that at each condition/time point these intensity values added up to exactly 1,000,000, therefore each protein group value can be regarded as a normalized microshare. These microshare values were then compared to the normalized microshare LFQ based intensities from our label free meiotic time course samples (Figure S1D, see below).

Control meiotic time course proteomics data generated by Label Free Quantification

In order to validate the TMT-based quantification results, we performed proteomics-based label free quantification (LFQ), which does the quantification on the MS1 level, instead of the MS2 level and does not allow multiplexing as is the case for TMT labeling. Therefore, different systematic biases are introduced by LFQ based proteomics than by TMT based proteomics and it serves as a quite stringent test to our deep proteome quantification results obtained by our TMT based approach. We quantified 9 matched samples, all coming from the second replicate of the meiotic time course. The only sample missing was the “25 hours spore” sample. Proteins were precipitated by adding -20C cold acetone to the lysate (acetone to eluate ratio 10:1) and overnight incubation at -20C. The proteins were pelleted by centrifugation at 20000xg for 15min at 4C. The supernatant was discarded and the pellet was left to dry by evaporation. The protein pellet was reconstituted in 100 mL urea buffer (8M Urea, 75mM NaCl, 50mM Tris/HCl pH 8.0, 1mM EDTA) and protein concentrations were determined by BCA assay (Pierce). 20 mg of total protein per sample were processed further. Disulfide bonds were reduced with 5mM dithiothreitol and cysteines were subsequently alkylated with 10mM iodoacetamide. Samples were diluted 1:4 with 50mM Tris/HCl (pH 8.0) and sequencing grade modified trypsin (Promega) was added in an enzymeto-substrate ratio of 1:50. After 16h of digestion, samples were acidified with 1% formic acid (final concentration). Tryptic peptides were desalted on C18 StageTips according to Rappsilber et al. (2007) and evaporated to dryness in a vacuum concentrator. Desalted peptides were reconstituted in Buffer A (0.2% Formic acid).

LC-MS/MS analysis was performed on a Q-Exactive HF. Each sample was measured twice (a total of 18 mass spec runs). Around 1 mg of total peptides were analyzed on an Eksigent nanoLC-415 HPLC system (Sciex) coupled via a 25cm C18 column (inner diameter 100 mm packed in-house with 2.4 mm ReproSil-Pur C18-AQ medium, Dr. Maisch GmbH) to a benchtop Orbitrap Q Exactive HF mass spectrometer (Thermo Fisher Scientific). Peptides were separated at a flow rate of 200nL/min with a linear 106min gradient from 2% to 25% solvent B (100% acetonitrile, 0.1% formic acid), followed by a linear 5min gradient from 25 to 85% solvent B. Each sample was run for 170min, including sample loading and column equilibration times. Data was acquired in data dependent mode using Xcalibur 2.8 software. MS1 Spectra were measured with a resolution of 60,000, an AGC target of 3e6 and a mass range from 375 to 2000 m/z. Up to 15 MS2 spectra per duty cycle were triggered at a resolution of 15,000, an AGC target of 2e5, an isolation window of 1.6 m/z and a normalized collision energy of 27.

All raw data were analyzed with MaxQuant software version 1.6.0.16 (Cox and Mann, 2008) using a UniProt yeast database (release 2014_09, strain ATCC 204508 / S288c), and MS/MS searches were performed with the following parameters: The two replicate runs per sample were grouped together. Oxidation of methionine and protein N-terminal acetylation as variable modifications; carbamidomethylation as fixed modification; Trypsin/P as the digestion enzyme; precursor ion mass tolerances of 20 ppm for the first search (used for nonlinear mass re-calibration) and 4.5 ppm for the main search, and a fragment ion mass tolerance of 20 ppm For identification, we applied a maximum FDR of 1% separately on protein and peptide level. “Match between the runs” was activated, as well as the “LFQ” (at least two ratio counts were necessary to get an LFQ value). We required 1 or more unique/razor peptides for protein identification and a ratio count of 2 or more for label free protein quantification in each of the 9 samples. This gave us LFQ values for a total of 1568 protein groups.

Finally, we normalized the MaxQuant generated LFQ intensities such that at each condition/time point the LFQ intensity values added up to exactly 1,000,000, therefore each protein group value can be regarded as a normalized microshare (we did this separately for each sample for all proteins that were present in that sample).

Ndt80 release proteomics measurements

Proteins were precipitated by adding -20C cold acetone to the lysate (acetone to eluate ratio 10:1) and overnight incubation at -20C. The proteins were pelleted by centrifugation at 20000xg for 15min at 4C. The supernatant was discarded and the pellet was left to dry by evaporation. The protein pellet was reconstituted in 100 mL urea buffer (8M Urea, 75mM NaCl, 50mM Tris/HCl pH 8.0, 1mM EDTA) and protein concentrations were determined by BCA assay (Pierce). 15 mg of total protein per sample were processed further. Disulfide bonds were reduced with 5mM dithiothreitol and cysteines were subsequently alkylated with 10mM iodoacetamide. Samples were diluted 1:4 with 50mM Tris/HCl (pH 8.0) and sequencing grade modified trypsin (Promega) was added in an enzyme-to-substrate ratio of 1:50. After 16h of digestion, samples were acidified with 1% formic acid (final concentration). Tryptic peptides were desalted on C18 StageTips according to Rappsilber et al. (2007) and evaporated to dryness in a vacuum concentrator. Desalted peptides were labeled with the TMT10plex mass tag labeling reagent according to the manufacturer's instructions (Thermo Scientific) with small modifications. Briefly, 0.2units of TMT10plex reagent was used per 15 mg of sample. Peptides were dissolved in 30 mL of 50mM HEPES pH 8.5 solution and the TMT10plex reagent was added in 12.3 mL of MeCN. After 1h incubation the reaction was stopped with 2.5 mL 5% Hydroxylamine for 15min at 25C. Differentially labeled peptides were mixed for each replicate (see mixing scheme in Table S8) and subsequently desalted on C18 StageTips (Rappsilber et al., 2007) and evaporated to dryness in a vacuum concentrator.

The peptide mixtures were fractionated by Strong Cation Exchange (SCX) using StageTips as previously described (Rappsilber et al., 2007) with slight modifications. Briefly, one StageTip was prepared per sample by 3 SCX discs (3M, #2251) topped with 2 C18 discs (3M, #2215). The packed StageTips were first washed with 100 mL methanol and then with 100 mL 80% acetonitrile and 0.2% formic acid. Afterward they were equilibrated by 100 mL 0.2% formic acid and the sample was loaded onto the discs. The sample was transeluted from the C18 discs to the SCX discs by applying 100 mL 80% acetonitrile; 0.2% formic acid, which was followed by 3 stepwise elutions and collections of the peptide mix from the SCX discs. The first fraction was eluted with 50 mL 50mM NH4AcO; 20% MeCN (pH 7.2), the second with 50 mL 50mM NH4HCO3; 20% MeCN (pH 8.5) and the sixth with 50 mL 0.1% NH4OH; 20% MeCN (pH 9.5). 200 mL of 0.2% acetic acid was added to each of the 3 fractions and they were subsequently desalted on C18 StageTips as previously described (Rappsilber et al., 2007) and evaporated to dryness in a vacuum concentrator. Peptides were reconstituted in 10 mL 0.2% formic acid. Both the unfractionated samples plus the fractionated, less complex samples were afterward analyzed by LC-MS/MS on a Q-Exactive HF was performed as previously described (Keshishian et al., 2015).

Around 1 mg of total peptides were analyzed on an Eksigent nanoLC-415 HPLC system (Sciex) coupled via a 25cm C18 column (inner diameter of 100 mm, packed in-house with 2.4 mm ReproSil-Pur C18-AQ medium, Dr. Maisch GmbH) to a benchtop Orbitrap Q Exactive HF mass spectrometer (Thermo Fisher Scientific). Peptides were separated at a flow rate of 200nL/min with a linear 106min gradient from 2% to 25% solvent B (100% acetonitrile, 0.1% formic acid), followed by a linear 5min gradient from 25 to 85% solvent B. Each sample was run for 170min, including sample loading and column equilibration times. Data was acquired in data dependent mode using Xcalibur 2.8 software. MS1 Spectra were measured with a resolution of 60,000, an AGC target of 3e6 and a mass range from 375 to 2000 m/z. Up to 15 MS2 spectra per duty cycle were triggered at a resolution of 60,000, an AGC target of 2e5, an isolation window of 1.6 m/z and a normalized collision energy of 36.

All raw data were analyzed with MaxQuant software version 1.6.0.16 (Cox and Mann, 2008) using a UniProt yeast database (release 2014_09, strain ATCC 204508 / S288c), and MS/MS searches were performed with the following parameters: The five mass spec runs were grouped together. TMT11plex labeling on the MS2 level, oxidation of methionine and protein N-terminal acetylation as variable modifications; carbamidomethylation as fixed modification; Trypsin/P as the digestion enzyme; precursor ion mass tolerances of 20 ppm for the first search (used for nonlinear mass re-calibration) and 4.5 ppm for the main search, and a fragment ion mass tolerance of 20 ppm. For identification, we applied a maximum FDR of 1% separately on protein and peptide level. We required 1 or more unique/razor peptides for protein identification and a ratio count for each of the 10 TMT channels. This gave us a total of 2908 quantified protein groups.

Finally, we normalized the MaxQuant generated corrected TMT intensities such that at each condition/time point the corrected TMT intensity values added up to exactly 1,000,000, therefore each protein group value can be regarded as a normalized microshare (we did this separately for each TMT channel for all proteins that were made our filter cutoff in all the TMT channels).

4.3.12 Sequence alignments, data analysis

Sequencing data were analyzed exactly as in Brar et al. (2012) and Ingolia et al. (2012). In short, bowtie2-based alignment (Langmead and Salzberg, 2012) was used and only unique sequences were mapped. Bowtie2-based mapping and subsequent quantification for ribosome profiling data were executed using quality control metrics and scripts written by Nick Ingolia. These quality control metrics include analysis of ribosome footprint length distributions in ribosome profiling samples to confirm periodicity and optimal RNase I digestion. Gene expression quantification involved summing unique reads over annotated ORFs and adjustment for RPKM (reads per kilobase million) values. Only genes and time points with at least 10 raw ribosome footprint or mRNA reads were used for analyses. Mochiview was used for genome browsing and motif analysis, Cluster 3.0 and Treeview were used for cluster analyses and visualization. All correlation measurements used throughout this manuscript are Pearson correlations.

As is true of most genome-wide studies, our measurements are relative, representing the proportional levels of either mRNA, ribosome footprints, or protein in the population. For meiotic time points, including and between 1.5 and 8 hours, these values are expected to be quantitatively comparable, as our previous measurements determined no major shifts in bulk mRNA, translation, or protein levels over this time span. In contrast, major metabolic shifts are expected as cells enter meiosis (from 0 hr to 1.5 hr) and as they complete spore formation, and major metabolic differences are likely to exist between cells in sporulation medium and rich medium. We chose, however, to analyze relative measurements among all time points for two reasons. First, our previous attempts to normalize our measurements relative to doped oligos or exogenous mRNAs introduced an additional source of noise to the data that obscured real biological regulation (Brar et al., 2012). Second, we determined based on examination of the patterns of mRNA, translation, and protein for well studied genes, that our measurements mirrored those from our own and others' published studies and thus seemed reliable despite some expected metabolic shifts. Nonetheless, we generally refrain from making quantitative comparisons between measurements made in rich media and cells in sporulation media, as these comparisons are the most likely to include complicating large bulk effects.

Note that, although full biological replicates were collected and matched extremely well in most instances, the mRNA for the vegetative exponential replicate 2 appeared contaminated. Attempts were made to re-prepare this sample once this was determined, but the issue was not identified and this sample, in particular, looks unlike vegetative exponential samples that our lab has previously prepared. Because the assignment of replicate 1 and 2 for this sample was arbitrary and because the footprint samples collected from the same culture flasks agreed very well (Table S3), we used the replicate 1 data for the vegetative exponential mRNA. This was the only instance in which the samples were not completely matched from identical cells and we believe that it does not affect the results based on comparisons with our previous time course and thorough replicate analyses of the ribosome footprints and protein for this sample.

4.3.13 Genome browsing/motif analysis

We used Mochiview (Homann and Johnson, 2010) for all of our genome browser analyses and motif analyses.

4.3.14 Data clustering and visualization

We used Cluster 3.0 (de Hoon et al., 2004) for our hierarchical clustering, using uncentered correlation clustering with the centered setting. We visualized the results using Java Treeview (Saldanha, 2004).

4.3.15 Translation Efficiency measurements

Translation efficiency measurements were calculated for each gene and time point from the formula FPRPKM/mRNARPKM, in both cases only using values that resulted from 10 raw reads or more and in each case, summing only over the annotated open reading frame (ORF).

4.3.16 LUTI annotation

We isolated the pool of genes for which we quantified protein in this dataset and had previously identified evidence for meiotic translation of an AUG-initiated uORF. This pool included 911 genes. We then filtered on the mRNA to protein Pearson correlation over all time points, choosing a cutoff at 0.4 to represent “poor” correlation, narrowing the pool to 624 genes. We then assayed mRNA-seq data by genome browser, comparing all time points and taking forward only genes that showed evidence for an alternate 50 extended transcript at some point. We also required that these genes show AUG-initiated uORF translation in this dataset by genome browser analysis of ribosome profiling data and that this translation did not mirror translation of the downstream ORF (or was broadly consistent with an inverse relationship between uORF and ORF translation). In cases in which reads for ribosome profiling reads over uORFs were low or noisy, occasionally observed due to the short nature of many of these regions, we alternatively allowed a case to be scored as positive if the TE at the time point when the transcript appeared long by genome browser analysis was lower than the TE when the transcript appeared short by genome browser analysis. This determination did not require any fold change cutoff so that the quantitative confirmation in part Figure 6A would be independent. The results of this approach are summarized in the pie chart. In 59 cases, we could not analyze the locus for evidence of an alternative transcript due to overlap with a neighboring transcript. In 5 cases, we observed regulation that appeared similar to that observed for the SER3/SRG1 locus (see Figure S7G for example and discussion) (Martens et al., 2004), with regulated appearance of an alternate overlapping transcript that does not contain the full canonical ORF; in 3 cases the regulation was difficult to categorize for other reasons; and in 177 cases, there was no clear evidence for an alternative transcript. In the remaining 380 cases, there is moderate to strong evidence for LUTI-based regulation. This includes 78 of the 156 cases that we had annotated as showing alternate 50 leaders in our original mRNA-seq dataset (Brar et al., 2012).

4.3.17 Data and software availability

The accession numbers for the raw sequencing and mass spectrometry data reported in this paper are NCBI GEO: GSE108778 and MassIVE: MSV000081874. Processed data used for analyses in this manuscript are included as Tables S3, S4, S5, and S6.

4.4 Supplemental figures

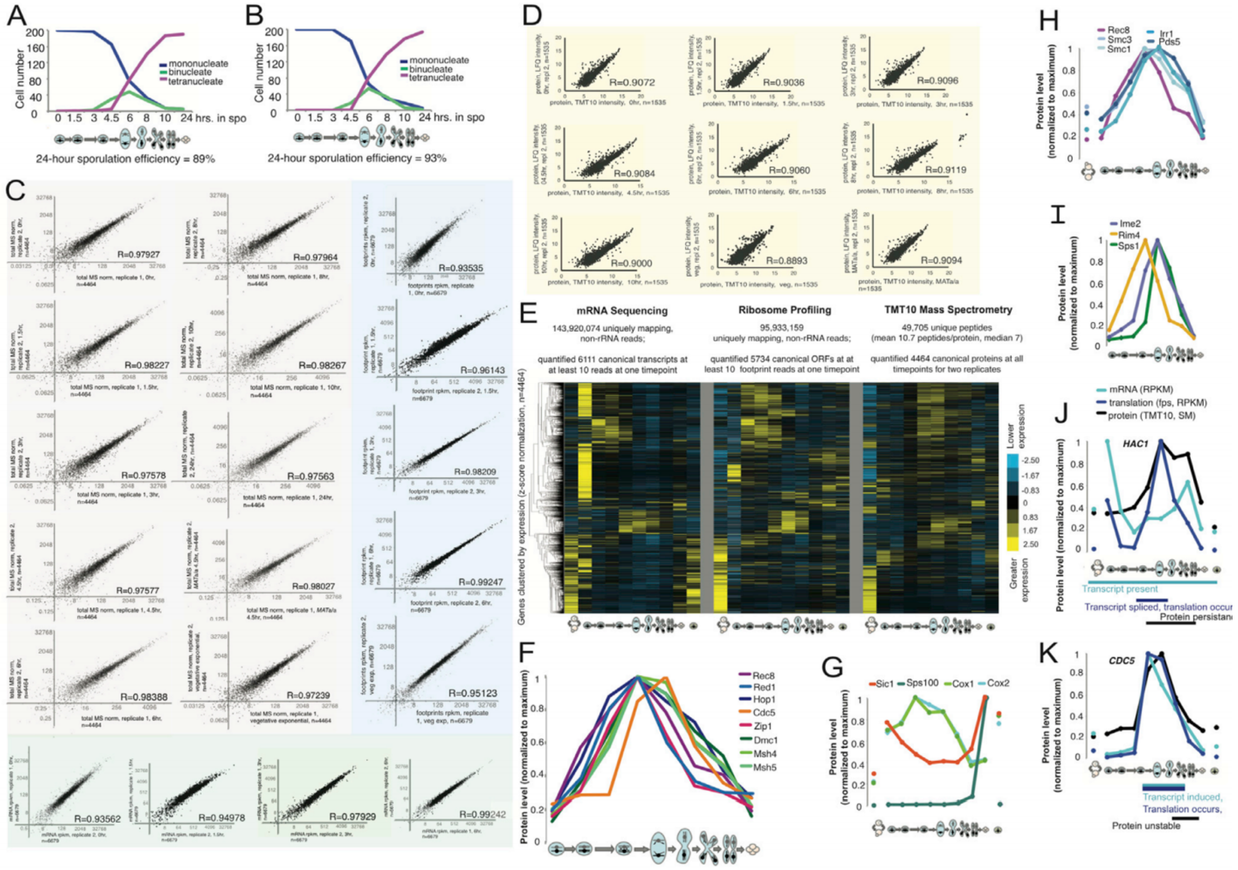

Figure 4.S1. Meiotic Timecourse Data Were Reproducible and Showed Expected Patterns for Well-Studied Genes (A and B) Counts of DAPI-based DNA morphology for timecourse replicate 1 and 2, respectively. 200 cells were counted per strain per timepoint for presence of a single DNA mass (mononucleate), two separated DNA masses (binucleate), or four separated DNA masses (tetranucleate). (C) Full biological replicate measurements agree well for protein, mRNA, and ribosome footprints. In gray, a comparison of TMT10-based protein measurements for timecourse 1 and 2 are shown for each timepoint. In blue are similar plots for ribosome profiling samples, and in green, for mRNA-seq. R-values are to the bottom right of each graph. Each dot represents a single gene, genes are not filtered for any expression threshold. (D) Mass spectrometry measurements made by independent label free quantification show high agreement with our original TMT10 measurements. All timepoints (except spores, for which sufficient material was unavailable) were subjected to mass spectrometry and label free quantification. The values for these measurements compared to TMT10 measurements for all genes that were quantified by both (n=1535) are shown in scatter plots. The TMT10 values represented in these plots are TMT based fractions of the total MS1 signal. (E) An overview of the timecourse, with z-score normalization for the mRNA-seq (left), ribosome profiling (middle), and mass spectrometry (right). Plot includes all samples that were quantified by all three methods (n=4464 annotated genes). 523 proteins change by at least two-fold between 1.5 hours and 8 hours in sporulation media, a timeframe that contains no broad shift in cellular metabolism. When including all timepoints, including transitions between rich and sporulation media, more regulation is observed, with 2087 proteins that show relative changes of at least two-fold. (F) Protein abundance trends for factors involved in homologous recombination and assembly of the synaptonemal complex (SC) confirmed known regulation for proteins that have well characterized regulation (Cahoon and Hawley, 2016; Lynn et al., 2007). SC assembly begins with chromosome axis formation on each new pair of replicated sister chromatids, mediated by Rec8 (as part of the meiotic cohesin complex), Hop1, and Red1. Zip1 next assembles between the axes to stabilize homolog interactions. These assembly steps occur with timing that overlaps the progression of recombination and influences its outcome, with Dmc1 as an important mediator of strand invasion of resected double-strand breaks to allow repair, and MutS

proteins, Msh4 and Msh5, forming a heterodimer that is involved in resolving crossovers. The pattern of accumulation of all of these proteins fits well with the relative timing of these known functions, as does their disappearance. Polo kinase, Cdc5, is induced in late prophase, which results in phosphorylation and degradation of Red1 and Zip1 (Prugar et al., 2017; Sourirajan and Lichten, 2008). The rapid loss of Red1 and Zip1 seen in these data, relative to other factors, like Dmc1, is consistent with single-gene studies. (G) Sps100, a component of the spore wall, is low at all timepoints except the one representing mature spores (Law and Segall, 1988). Sic1 degradation is required for meiotic DNA replication (Sedgwick et al., 2006). Its timing of protein decline matches the timing of meiotic DNA replication. Sporulation media (Spo) does not contain a fermentable carbon source and thus the oxidative phosphorylation machinery is upregulated. Consistently, mitochondrial proteins, including Cox1 and Cox2 of the electron transport chain, are seen to be high early in meiosis. (H) The meiotic cohesin complex consists of Rec8, the heterodimer Smc1/Smc3, and Irr1. It loads onto the chromosomes during meiotic S-phase, and is stabilized by Pds5. We measure all components to have similar patterns of protein accumulation, but Rec8 disappears first, an expected result of protein degradation through the N-end rule pathway and separase-mediated cleavage, to trigger anaphase (Buonomo et al., 2000). (I) Sps1 is known to be translated only after MI, despite high prior levels of mRNA, through a mechanism that involves silencing of SPS1 mRNA by its presence in aggregates of Rim4, which are disassembled as a result of phosphorylation by the meiotic CDK, Ime2 (Berchowitz et al., 2013, 2015). The protein level measurements for these factors match this known regulation remarkably well. (J) We can identify known instances of translational control by comparison of mRNA and translation levels. In the case of HAC1, whose mRNA is high and constitutive but contains a cytoplasmically retained intron that prevents productive translation in the absence of Unfolded Protein Response activation, we observe translation during late MI and early MII, as we previously reported (Brar et al., 2012; Cox and Walter, 1996). (K) Cdc5, or polo kinase, serves as a control, as it is not thought to be regulated translationally, but its transcription is driven by Ndt80 in late prophase. Consistently, we observe overlapping plots for mRNA and translation measurements, suggesting no or minimal translational control and, as also expected, protein measurements come up with similar timing as the other two. Cdc5 protein is known to be actively degraded by Ama1, and consistently, we see the levels decline rapidly after translation ceases (Okaz et al., 2012).

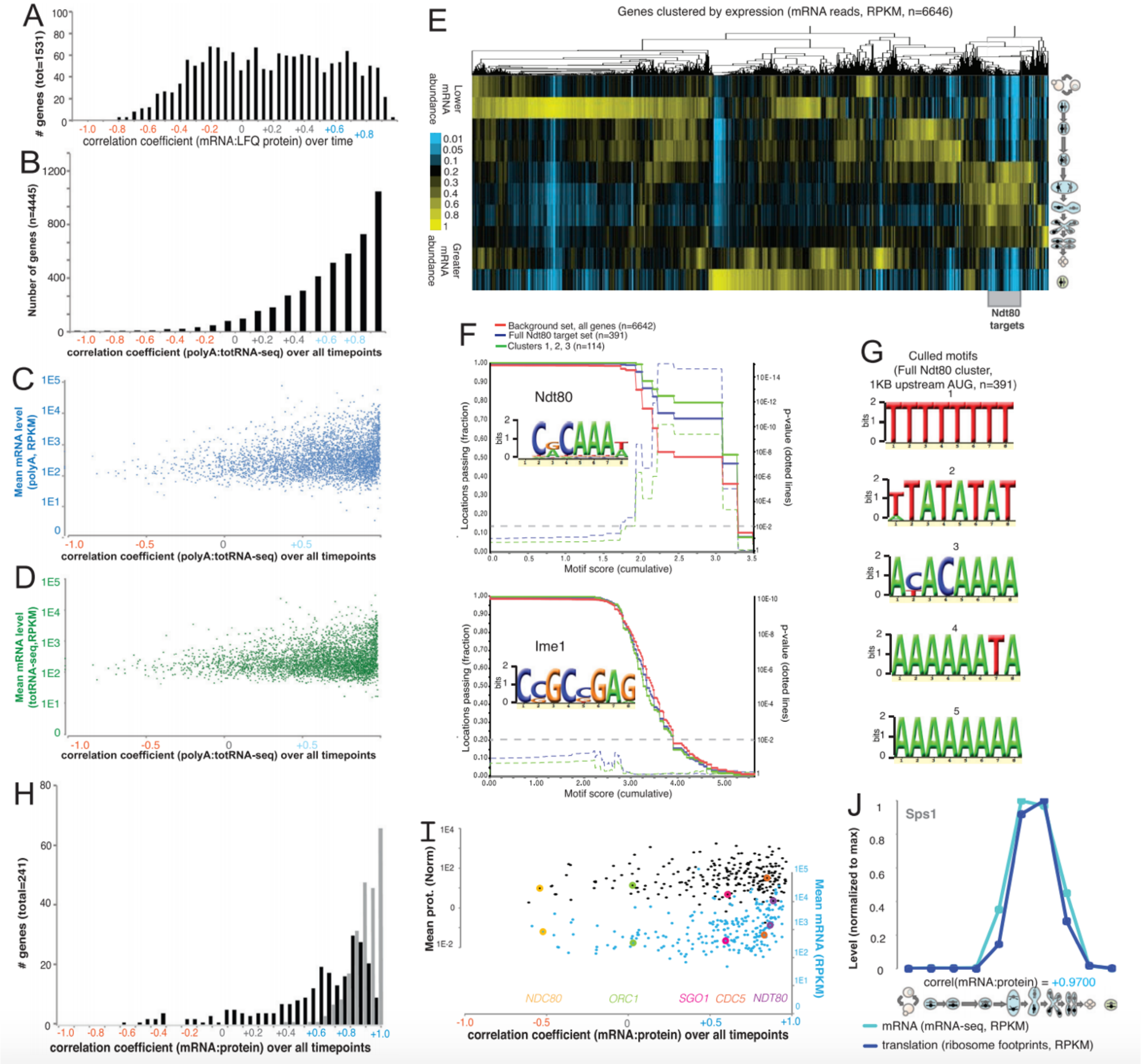

Figure 4.S2. Many Genes Show a Poor mRNA-to-Protein Correlation, both Generally and among the Large Set of Targets of the Transcription Factor Ndt80 (A) Comparison of label-free protein quantification and mRNA-seq reveals a similar large subpopulation of genes showing anti-correlated trends between mRNA and protein over meiosis as seen when TMT10 data are used instead (compare to Figure 2A). (B) A histogram of the Pearson correlations between mRNA-seq for each timepoint from single round poly-A selection and total RNA-seq. Note that the distribution is positive and does not show subpopulations. (C) Average expression of mRNA from single round poly-A selection versus correlation values from B). (D) Average expression of mRNA from total RNA-seq versus correlation values from B). (E) A global view of transcript abundance in meiotic differentiation. Shown is the result of centroid hierarchical clustering of the ribosome profiling data for all genes (rows) quantified for mRNA abundance at all timepoints (columns). The total signal in each row is normalized to allow comparisons. The discrete cluster of genes that are thought to be Ndt80 targets are highlighted by a gray box at right. (F and G) Promoters of genes identified as being Ndt80 targets based on mRNA abundance patterns are enriched for the Ndt80 binding site, or Middle Sporulation Element (MSE), regardless of protein concordance. F) Mochiview quantification of Ndt80 binding site cumulative enrichment upstream of Ndt80 targets identified from mRNA abundance patterns. Genes in the aberrant clusters (noted in Figure 2A), all Ndt80 targets, and a background set are shown. Note no enrichment in the aberrant clusters for the binding motif for an unrelated meiotic transcription factor, Ime1. In both plots, p-values for difference of each query set from the background set are shown as dotted lines that depend on the motif score cutoff chosen. G) An unbiased motif search using Mochiview motif finder for upstreamregions of Ndt80 targets (Figure S2E; Figure 2C) identified from mRNA abundance patterns revealed degenerate AT rich motifs, characteristic of intergenic regions, but only one other, specific motif, which closely matched the MSE. (H) A histogram of Pearson correlation coefficients are plotted over all timepoints for the set of genes shown in Figure 2C and 2D. Black bars represent the correlation coefficients for protein and mRNA for a given gene. Gray bars represent the correlation coefficients for mRNA of a given gene compared to mRNA for NDT80. (I) The mean protein and mRNA levels over all timepoints are plotted for each gene, versus correlation coefficients (mRNA:protein) as shown in H.

Colored dots represent known, well characterized targets of Ndt80. (J) Known, robust translational regulation of SPS1 is subtle with the resolution of our timepoints. mRNA and ribosome profiling measurements are plotted relative to max values to allow comparison. SPS1 message is known to be translationally repressed for at least 1 hour after accumulation and a delay in the translation peak relative to the mRNA peak can be seen, but because timepoints are 1.5 hr-2hr apart, this effect appears subtler than in previous studies with higher resolution timepoints.

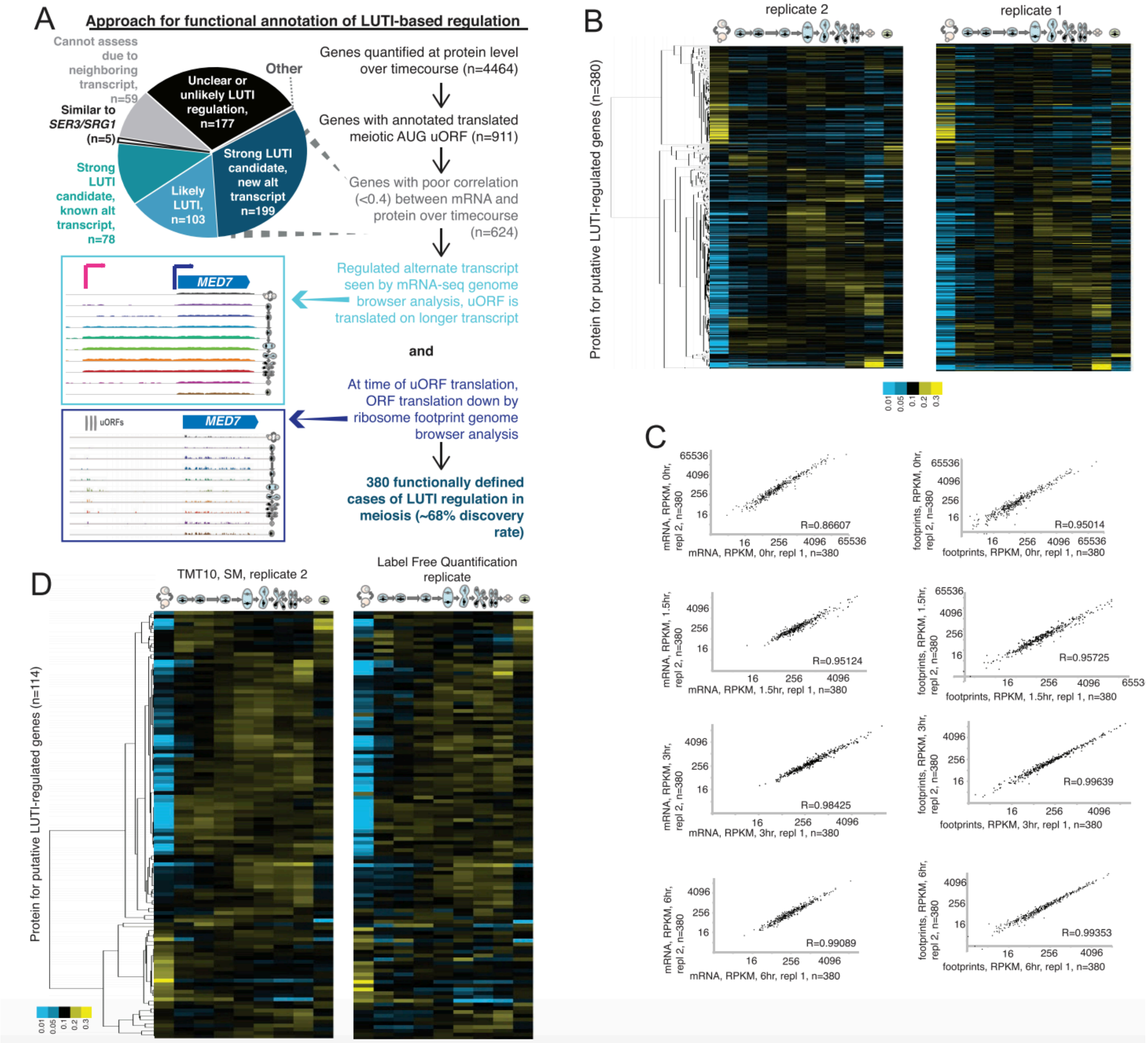

Figure 4.S3. Pipeline for Identification of LUTI-based Regulation Reveals 380 Robust Cases (A) A more detailed outline of approach in Figure 3D. See STAR Methods for detailed description. (B) TMT10 protein measurements for the 380 genes identified in the approach outlined in Figure 3D as showing protein levels that are regulated by transcript toggling are shown, with hierarchical clustering performed on timecourse replicate 2 (left) and values from timecourse replicate 1 shown with rows matched at right. (C) mRNA-seq and ribosome profiling from the two timecourse replicates for four meiotic timepoints each were performed and comparison of these values in scatter plots is shown for each case for the 380 LUTI candidates. (D) LUTI candidates show protein measurements with similar trends whether measurements are done by TMT10 or label free quantification. At left, the TMT10 values for timecourse replicate 2 are shown following hierarchical clustering of the 114/380 LUTI candidates that were quantified by both TMT10 and label free quantification over timecourse. At the right are values as measured by label free quantification.

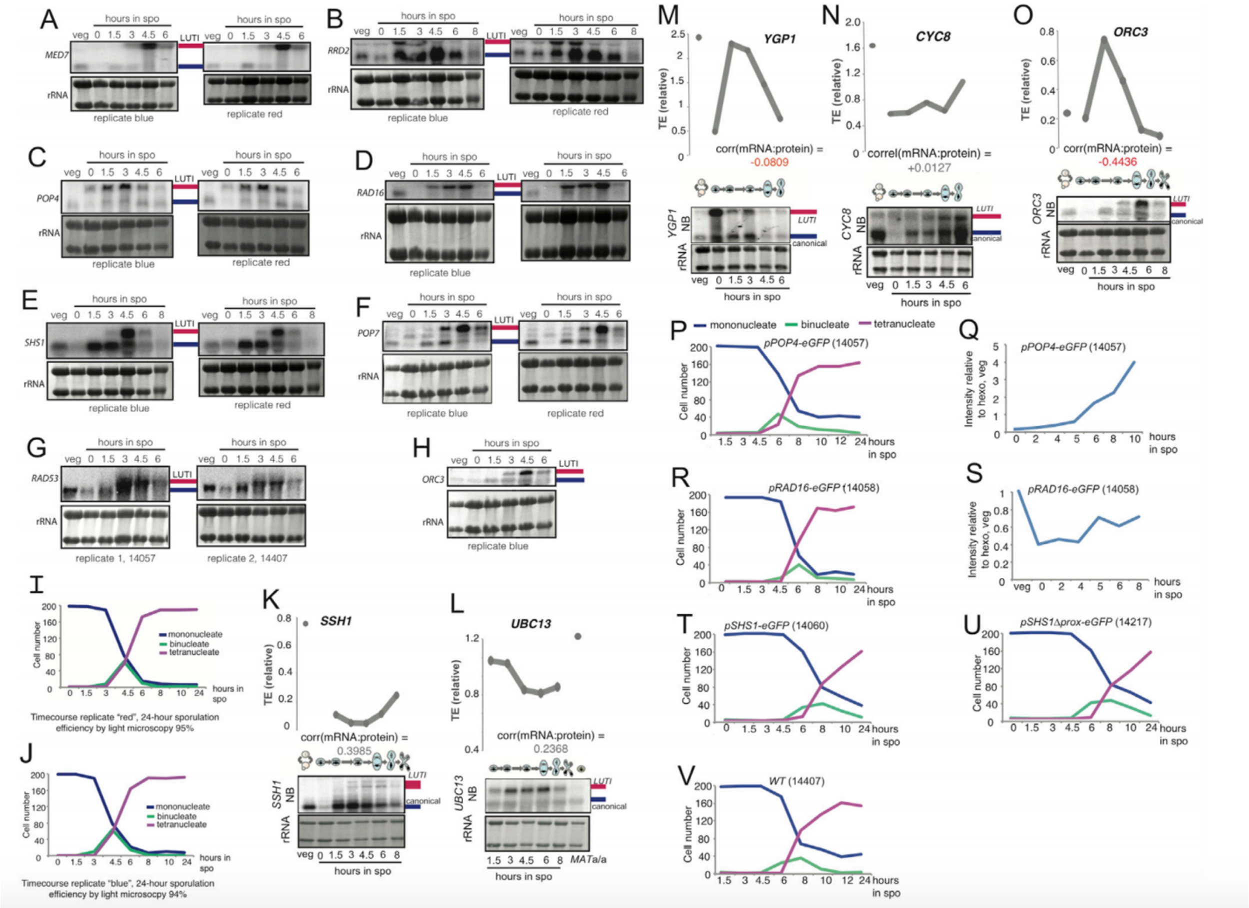

Figure 4.S4. New LUTI Cases Can Be Confirmed by Robust Alternate Approaches (A–H) Shown are independent meiotic timcourse replicates showing similar patterns for short and long transcripts detected in main Figures 4.4 and 4.6. ORFs probed are: A) MED7 B) RRD2 C) POP4 D) RAD16 E) SHS1 F) POP7 G) RAD53 H) ORC3. Only one replicate is shown for ORC3, as the other is in Figure 4.S4O. ORC3 and POP7 replicates were run on the same gel and therefore the methylene blue stained image showing the rRNA control is identical and is shown in both panels F and H. Note that RAD53 replicate blots are from a different set of timecourses, using strains 14057 and 14407 and RNA from the experiment staged in P) and V). (I and J) Staging of additional replicate timecourses for Northern blotting. Categorization of DAPI morphology into either mononucleate, binucleate, or tetranucleate was performed for 200 cells at each timepoint. I) DAPI counting reflecting synchronous meiotic progression is shown for timecourse ‘‘red’’ and J) ‘‘blue’’, used for blotting in Figure 4.S2A-F, H. K-O) Northern blot confirmation of additional LUTI candidates highlighted in Figure 4.4C. (K–O) Comparison of levels and timing between Northern blots for the translocon component-encoding SSH1 ORF and the TE in matched samples shows evidence for a poorly translated long transcript as predicted by the mechanism in Figure 4.7. A similar analysis for L) UBC13, encoding an E2 ubiquitin-conjugating enzyme, M) YGP1, encoding a cell wall glycoprotein, N) CYC8, a general transcriptional repressor. O) ORC3, a component of the origin recognition complex. Note that due to limiting extract from the original timecourse, the ORC3 Northern blot was performed on extract from replicate ‘‘timecourse red’’, staged in Figure 4.S2I. Meiotic progression, as judged by DAPI mass morphology, is shown for experiments presented in Figure 4.4G, 4.4I, 4.4K, 4.4L, 4.S4G. (P, R, and T–V) pPOP4-eGFP cells (14057) R) pRAD16-eGFP (14058) T) pSHS1-eGFP (14060) U) pSHS1Dprox-eGFP (14217) V) WT (14407). (Q) Quantification of pPOP4-eGFP Western blot in Figure 4.4G. (S) Quantification of pRAD16-eGFP Western blot in Figure 4.4I.

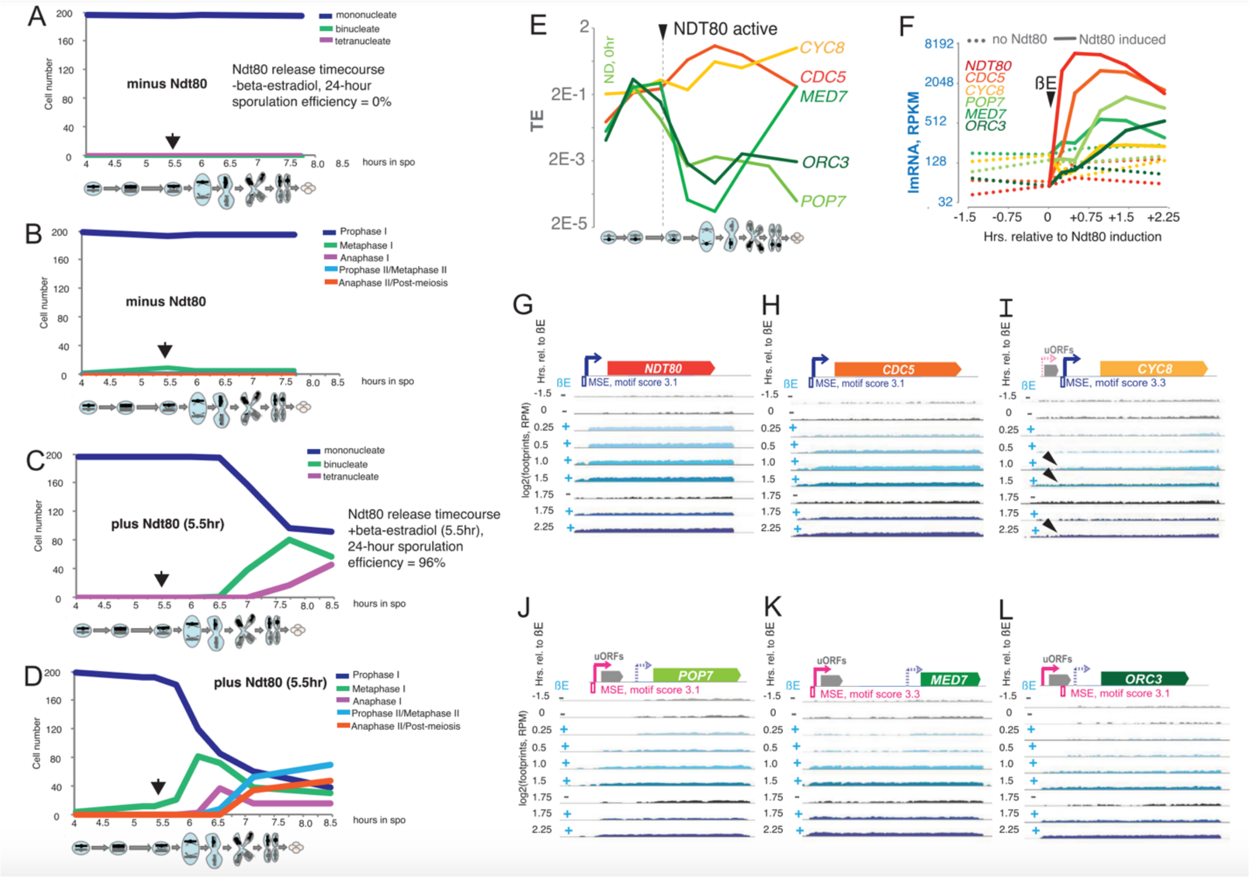

Figure 4.S5. Ndt80 Induces Long, Translationally Inactive Isoforms of POP7, MED7, and ORC3 and Canonical Transcript Isoforms of CDC5, HRR25, and CYC8. (A–D) Staging for experiment shown in Figure 5C-I by DAPI morphology without and with Ndt80 induction in A) and C), respectively and for spindle morphology by tubulin immunofluorescence in B) and D), respectively. Arrow indicates time of Ndt80 induction by addition of b-estradiol. (E) Plots of TE for transcripts induced by Ndt80 in original timecourse data. Approximate time of Ndt80 activation is indicated by arrow. Note that canonical transcripts show stable or increased TE, while long undecodable isoforms show a drop in TE despite an increase in overall transcript level. (F) This figure is the same as Figure 5D, but with only the genes shown in G-L to allow direct comparison. Induction of Ndt80 results in increased mRNA abundance for canonical and non- canonical targets. Arrow indicates time of Ndt80 induction by addition of b-estradiol. Note that, although levels of transcript accumulation vary, both positive (canonical) and negative (LUTI) targets are induced with similar timing. Note that accumulation is dependent on Ndt80. (G) Rapid induction of NDT80 mRNA can be seen within 15 minutes of addition of b-estradiol. (H) CDC5, a canonical target is induced in an Ndt80-dependent manner within 30 minutes of addition of b-estradiol. (I) A short (canonical) version of CYC8 is induced in an Ndt80-dependent manner. Note Ndt80-dependent TSS is at arrowhead and masked somewhat by longer transcript. Compare to Northern blot in Figures 5A and 5C. (J–L) Long uORF containing transcripts defined as LUTI-regulated by approach in Figure 3D are induced between 30 minutes and 1 hour after addition of b-estradiol in an Ndt80 dependent manner. Compare to Northern blots in Figures 5A and 5C.

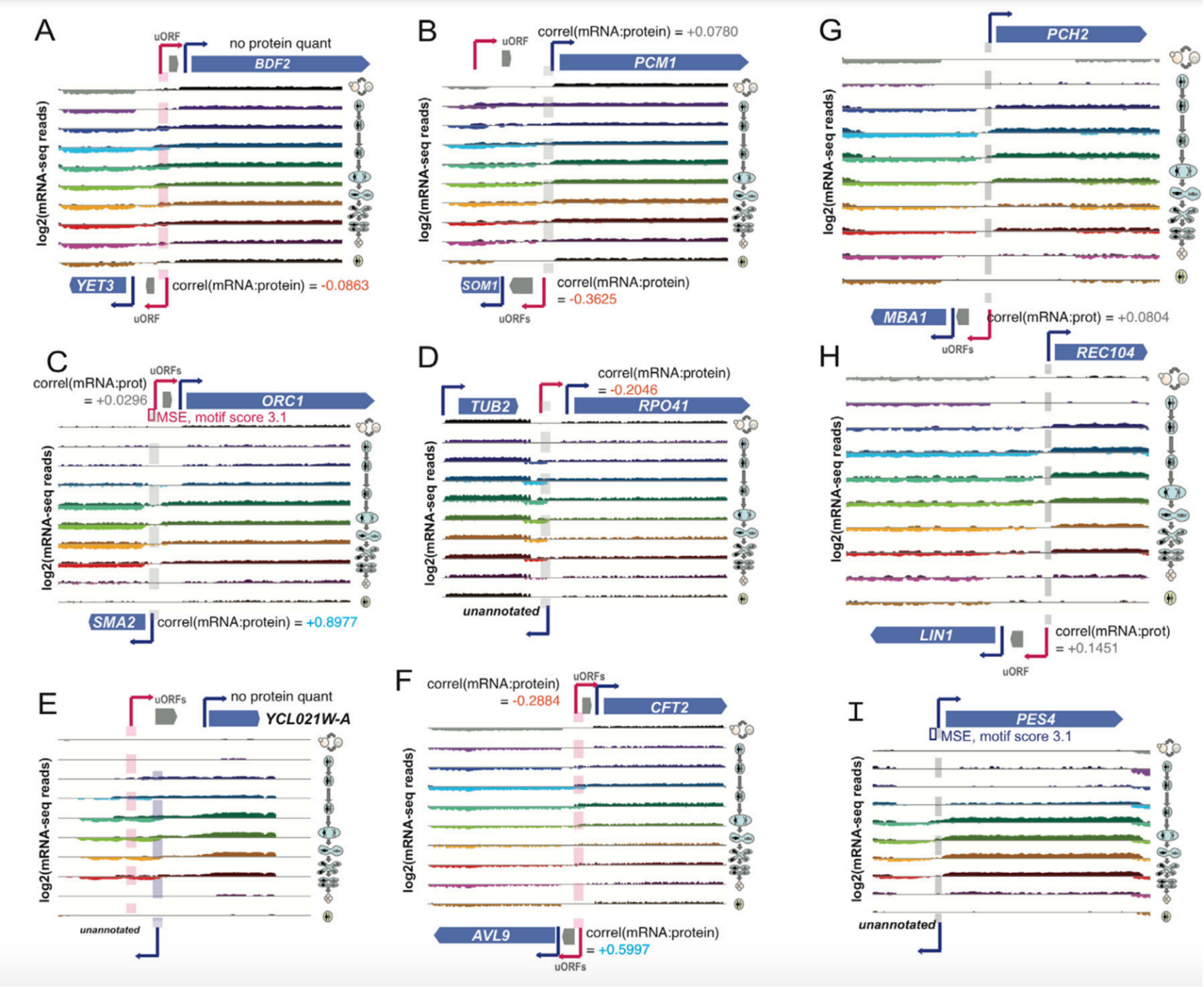

Figure 4.S6. Categorizing A Variety of Neighboring Transcript Associations with LUTIs (A) mRNA-seq data is shown for the BDF2/YET3 locus, revealing apparently coordinated divergent adjacent LUTIs. (B) mRNA-seq data is shown for the PCM1/SOM1 locus, revealing apparently divergent adjacent LUTIs that show mutually exclusive LUTI transcription timing. (C) mRNA-seq data is shown for the ORC1/SMA2 locus, highlighting LUTI regulation that is coordinated with transcription of a neighboring canonical transcript. (D) mRNA-seq data is shown for the RPO41 locus, revealing apparently coordinated transcription of a divergent unannotated transcript. (E) mRNA-seq data is shown for the YCL021W-A locus, revealing apparently coordinated transcription of a divergent unannotated transcript. (F) mRNA-seq data is shown for the CFT2/AVL9 locus, revealing apparently coordinated divergent adjacent long transcripts. CFT2 shows hallmarks of LUTI-based regulation, including a poor correlation between protein and mRNA, while AVL9 shows an alternative transcript but no clear evidence that this affects translation of the AVL9 ORF. (G–I) Transcription of meiosis-specific genes with spatiotemporal association with neighbors. G) Associated transcription between the MBA1 LUTI and canonical PCH2 transcript can be seen by mRNA-seq. H) Associated transcription between the LIN1 LUTI and canonical REC104 transcript can be seen by mRNA-seq. I) The Ndt80-induced PES4 transcript increases with timing and TSS position closely mirroring an unannotated transcript on the minus strand. An MSE is positioned at the point at which the two transcript 5′ ends meet.

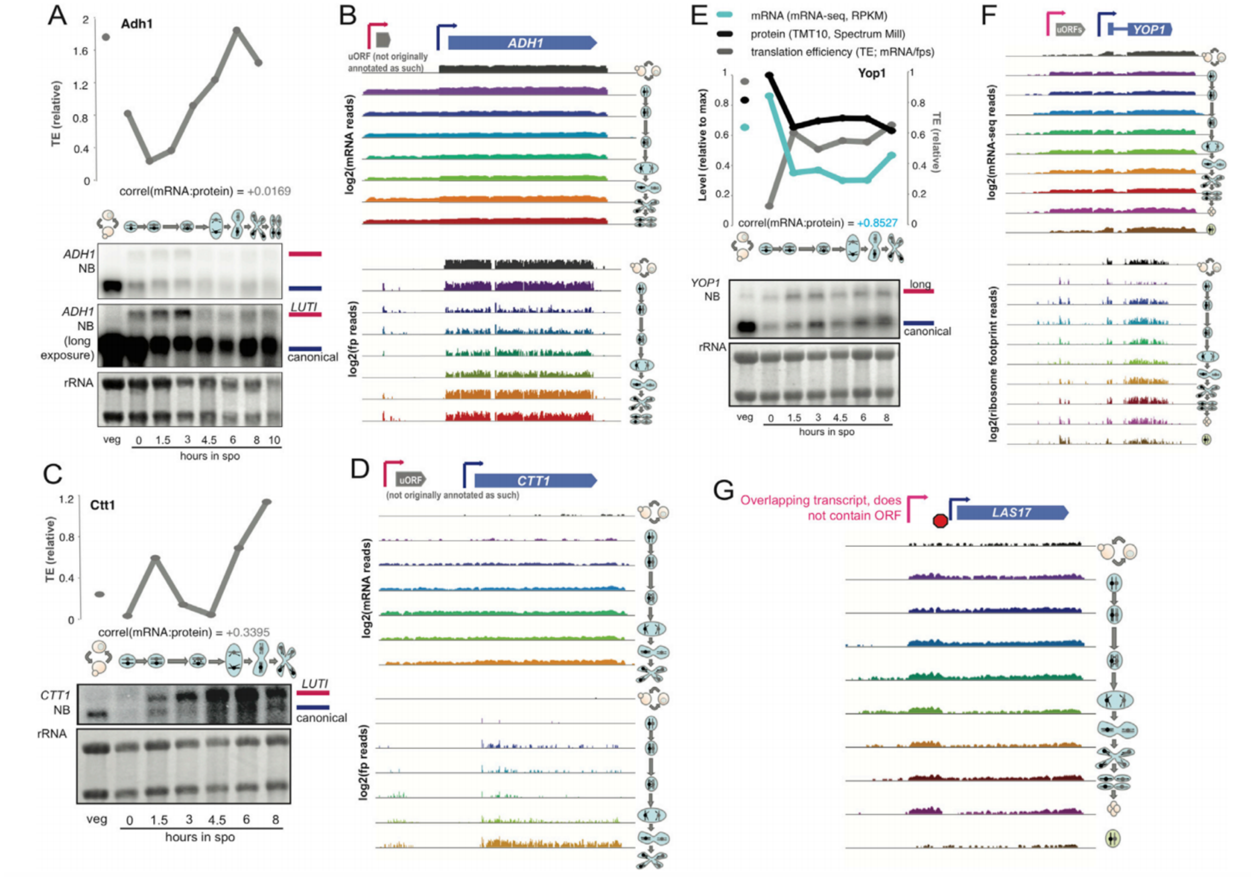

Figure 4.S7. Additional LUTIs Are Likely to Exist that Were Missed in Our Annotations due to Poorly Annotated AUG-Initiated uORFs (A) ADH1 shows a poor protein:mRNA correlation and Northern blotting reveals two transcripts, the longer of which is associated with a lower TE. (B) An inverse correlation between upstream translation of a misannotated AUG-initiated uORF and ADH1 ORF translation can be seen from ribosome footprint data at this locus. Matching mRNA-seq data are above. (C) CTT1 shows a poor protein:mRNA correlation and Northern blotting reveals two transcripts, the longer of which is associated with a lower TE. (D) mRNA-seq data at the CTT1 locus is ambiguous due to low expression levels and imperfect synchrony. It would be difficult from mRNA-seq alone to have predicted the short vegetative transcript or the mixed transcript pool at 8 hours. Matching ribosome profiling data are below. (E) YOP1 shows a long alternative transcript with translated AUG uORFs, but it is not a LUTI. Northern blotting of YOP1 confirms a longer alternative transcript at this locus of the size predicted from mRNA-seq data, but we do not find a clear association between the relative ratios of the two YOP1 transcripts and the TE at this locus (above). Consistently, the correlation between mRNA and protein for YOP1 is strongly positive (below graph). (F) mRNA-seq and ribosome footprint data at this locus suggest no negative association between translation of the AUG uORFs on the log transcript and the translation of the YOP1 ORF. (G) Putative new cases of the type of regulation reported for SER3/SRG1. Positive strand mRNA-seq data for the LAS17 locus are shown. Here it appears that the transcript that is initiated distally terminates and therefore does not contain the LAS17 ORF. This type of regulation has been shown to result in decreased transcription from the one canonical TSS (Martens et al., 2004), but would not produce a LUTI transcript.

Chapter 5: Seq-ing answers – uncovering the unexpected in global gene regulation

This chapter is an adaptation of the following publication:

Otto, G.M. and Brar, G.A., 2018. Seq-ing answers: uncovering the unexpected in global gene regulation. *Current Genetics*, 64, 1183–1188.

5.1 Introduction

The canonical model for gene expression, whereby information in genomic DNA sequences is decoded to produce protein through an mRNA intermediate, was defined based on painstaking studies by many labs using single-gene manipulations and biochemical approaches. Subsequent studies over decades identified additional complexity—including specificity factors and mRNA processing steps—that have added to our understanding of how gene expression is more-or-less universally regulated in eukaryotes. The development of techniques for global gene expression measurement within the last two decades was invaluable in enabling broad interrogation of these pre-existing "rules" for how gene regulation works. Now, with the widespread use of such methods, we can precisely measure every step in gene expression genome-wide. Employing these measurements has accelerated discovery in gene expression, in some cases confirming existing models, and sometimes revealing surprisingly common types of "non-canonical" regulation.

Genome-scale experiments provide immense amounts of data that can be analyzed to identify trends at individual levels of gene regulation and to highlight exceptional cases. Here, we discuss our recent study (Cheng et al. 2018), which used parallel global gene expression measurements to identify poor correlation between mRNA and protein levels over time for hundreds of genes controlled by an unconventional mode of gene regulation. For many genes regulated by this mechanism, an apparent increase in transcription corresponded with a switch to a poorly translated transcript, ultimately leading to a decrease in protein produced from the encoded locus. We will highlight important features of our experimental approach that enabled this surprising finding and discuss other studies that have been similarly successful in leveraging complex datasets to reveal specific mechanistic insight into a range of cellular gene regulatory strategies.

5.2 Our experiment: an overview

Our study (Figure 5.1) sought to define gene expression patterns comprehensively through budding yeast meiosis, a natural and conserved developmental process. Towards this end, we performed RNA-seq, ribosome profiling, and quantitative mass spectrometry on matched samples from ten conditions: eight timepoints spanning meiotic differentiation, one exponentially growing mitotic sample, and one media-matched non-meiotic sample. We restricted our analyses to cases that we were able to quantify at every timepoint, and by every method, which represented over 70% of annotated genes. Based on depth and time resolution, we believe that this is the most comprehensive gene expression atlas for a developmental program to date (Cheng et al. 2018).

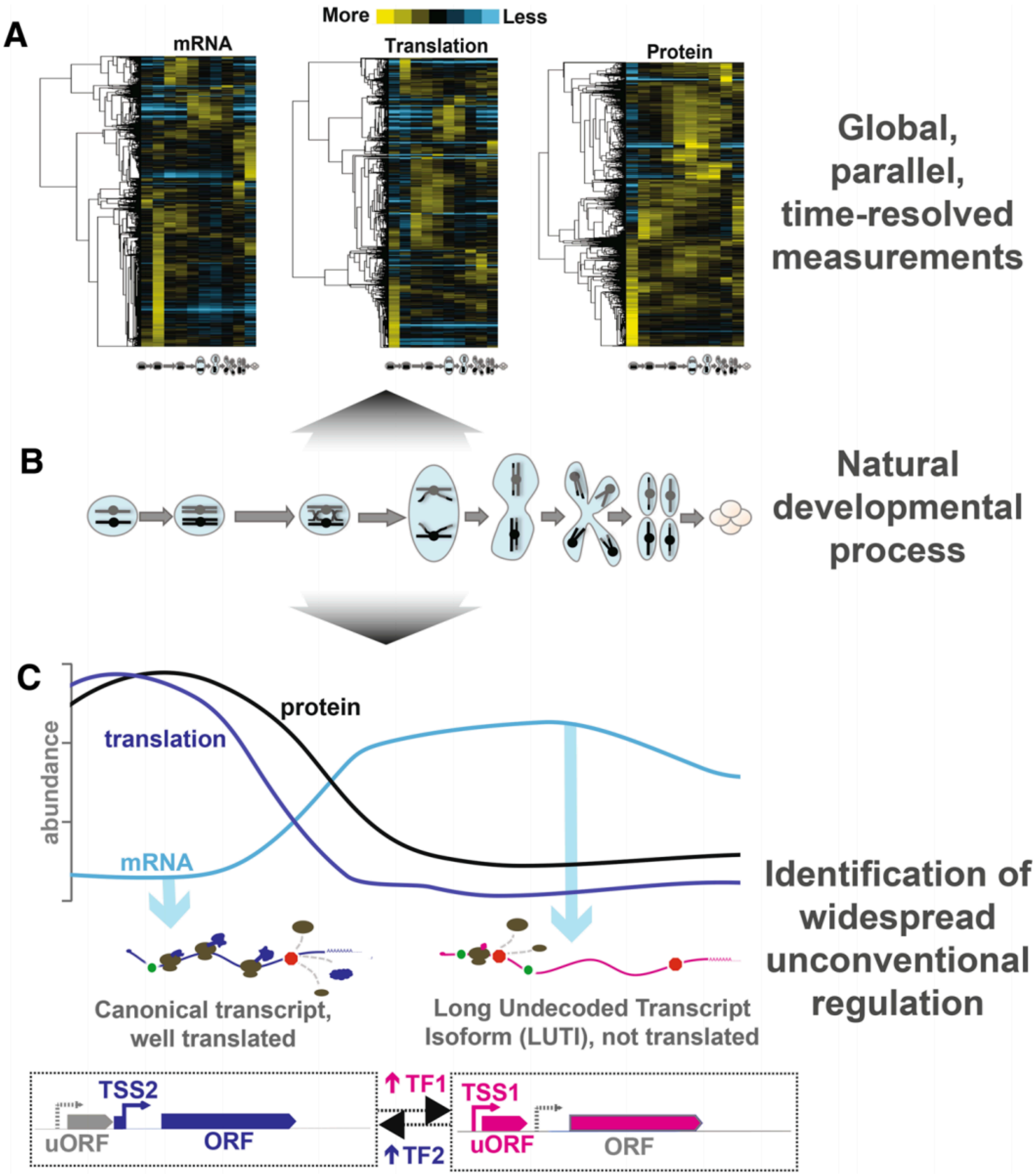

Figure 5.1 Integrated analysis of parallel, genome-wide measurements through meiotic development reveals pervasive non-canonical regulation of gene expression. (A) We performed RNA sequencing (mRNA), ribosome profiling (translation) and quantitative mass spectrometry (protein) on matched lysate from a timecourse spanning meiosis in budding yeast. Hierarchical clustering is displayed with rows representing individual genes (n=4464) that were quantified across all measurements and timepoints. Columns represent timepoints through meiotic differentiation depicted in (B). (B) Meiosis is a conserved cellular differentiation program comprised of a coordinated series of unidirectional transitions in cell state, ultimately producing haploid gamete cells from a diploid precursor. (C) Above, measurements of mRNA, translation and protein abundance are depicted for a model locus regulated by transcript isoform toggling. Below, a diagram for this model gene locus is shown. Transcription from an ORF-proximal transcription start site (TSS2) mediated by a developmentally regulated transcription factor (TF2) leads to the production of a canonical, well-translated transcript and the ORF-encoded protein is abundant. A decrease in TF2 and an increase in another transcription factor (TF1) results in a switch to transcription from an ORF-distal transcription start site (TSS1), producing a long undecoded transcript isoform (LUTI) mRNA that is poorly translated. ORF-encoded protein is reduced, despite increased transcription from this locus. As a consequence, ORF-encoding transcript abundance and ORF-encoded protein abundance show poor correlation over time. Using integrated parallel measurements outlined in (A), we identified widespread use of this unconventional regulatory mechanism for hundreds of genes.

Analysis of our dataset confirmed known regulation and revealed evidence of much more regulation at the level of protein abundance than was previously appreciated. Our most exciting finding, however, was the existence of a large class of genes for which mRNA levels were poorly predictive of protein levels. While this class is difficult to explain by traditional gene regulatory models, it included one gene that provided a hint to the regulation of other members of the group. This gene, NDC80, encodes a kinetochore component that is crucial for the success of meiosis (Kim et al. 2013; Meyer et al. 2015; Miller et al. 2012). NDC80 was recently found to be regulated by an unconventional strategy involving two transcript isoforms differing only in their transcription start sites—and, therefore, the length of their 5′ leaders (Chen et al. 2017; Chia et al. 2017). The longer transcript isoform contains several upstream open reading frames (uORFs) that are efficiently translated, resulting in reduced translation of the canonical ORF. The extended transcript isoform was named "LUTI" for long undecoded transcript isoform, and its transcription also resulted in reduced transcription of the canonical isoform at this locus (Chen et al. 2017; Chia et al. 2017). We queried our dataset for genes with features common to the LUTI-based regulation determined for NDC80 and found 380 genes to be regulated by this mechanism, representing nearly 8% of all yeast genes for which we collected measurements (Cheng et al. 2018).

We further found that a single meiotic transcription factor could coordinately drive transcription of two distinct classes of targets—canonical transcripts at some loci and LUTIs at others—resulting in protein level increases or decreases, respectively (Cheng et al. 2018). This has interesting consequences for how we think about gene regulatory logic. A mechanism for coordinated protein up- and down-regulation may be particularly important in developmental contexts, in which protein function is often stage-specific and progression to the next stage may require not just new protein synthesis, but also attenuated production of proteins that are no longer required. Using a single transcription factor to both up- and down-regulate protein production from distinct sets of target genes seems an efficient way of achieving rapid and efficient transitions in cell state.

Key features of our experimental design enabled our findings. First, we required genome-scale measurements to identify classes of genes that were similarly regulated by this mechanism. Furthermore, our analysis was built on the ability to confidently measure correlation (and anti-correlation) between mRNA and protein, which in turn relied on genome-wide measurements taken in parallel and across many timepoints. Finally, our choice of experimental system, a natural process of cellular differentiation, allowed us to identify a mechanism that is ideal for rapid and coordinated temporal changes. Below we discuss in greater detail how we and others have leveraged these experimental features to gain important and perhaps surprising insight into gene regulatory processes genome wide.

5.3 Genomics provides a wealth of information with emergent properties

The emergence of techniques for measuring global gene expression—beginning with microarrays in the 1990s—was revolutionary for the study of gene regulation (Brown and Botstein 1999). An unprecedented wealth of data allowed researchers to define near-complete transcriptional profiles for cells in any condition of interest [examples in Cho et al. (1998), Chu et al. (1998), DeRisi et al. (1997), Spellman et al. (1998)]. Researchers quickly realized that these datasets also possessed unforeseen emergent properties that enabled analyses beyond simply quantifying gene expression globally (Eisen et al. 1998; Zaslaver et al. 2004). For example, genes with shared function often cluster together based on expression patterns, enabling successful prediction of function for unstudied genes [reviewed in Brown and Botstein (1999)]. RNA sequencing later provided these same advantages while also allowing more detailed definitions of qualitative features, such as transcript boundaries and unbiased identification of transcription outside of predicted genes [reviewed in Berretta and Morillon (2009), Ozsolak and Milos (2011), Wang et al. (2009)]. Our study depended on an integrated analysis of both qualitative and quantitative aspects of genomic datasets. Without information about transcript boundaries together with abundance, for example, we could not have determined that the hundreds of new cases of unconventional protein regulation were based on transcript isoform toggling (Cheng et al. 2018).

Genome-wide measurements are powerful in that they inherently replicate every single-gene study ever performed in the condition of interest. By testing new datasets against the previous findings, researchers gain a straightforward quality control measure. If the data behave as predicted for cases in which regulation is known, it builds confidence in the dataset's ability to identify novel phenomena. Studying thousands of genes in parallel allows researchers to identify trends and outliers, both of which are important for a full understanding of the biological process in question. Moreover, rather than requiring researchers to guess a suitable control gene for comparison to their query, genomic datasets have thousands of built-in controls. Our study, for example, relied on detection of many cases of canonical regulation (which showed high mRNA-to-protein correlations) to provide the contrast needed to reveal a large class of non-canonical cases (Cheng et al. 2018).

5.4 Parallel measurements can capture the interplay between gene regulatory levels

It would be easy to dismiss disagreement between mRNA and protein levels as noise or measurement artifacts. We were nevertheless confident that there was biological meaning to the many cases of poor mRNA-to-protein correlation in our dataset, in part because our experimental design (Cheng et al. 2018) allowed direct comparison of mRNA and protein measurements from the same lysate, thus eliminating experiment-to-experiment variability. This type of preparation was also key to the first ribosome profiling studies, which enabled straightforward comparison of mRNA and translation levels (Brar et al. 2012; Ingolia et al. 2009, 2011). These experiments identified wider ranges in translation efficiencies (ribosome footprints/mRNA; TEs), than previously thought, suggesting unexpected translational specificity. Initial attempts to determine the relationship between mRNA and protein abundance relied on datasets from different labs and reported low apparent correlation between the two measurements. Selbach and colleagues (Schwanhäusser et al. 2011) were among the first to globally measure mRNA and protein abundance from the same sample, and found a much stronger mRNA-to-protein agreement (R2=0.41) than had been observed previously. However, single-sample comparisons—even among parallel samples—are largely driven by very highly and very lowly expressed genes. It is perhaps not surprising that the most highly abundant mRNAs also correspond to the most highly abundant proteins and does not necessarily preclude important post-transcriptional regulation. To illuminate additional regulation requires comparison, not only between different levels of gene regulation, but over time during conditions of cellular change.

5.5 Regulatory dynamics are captured by time-resolved series measurements

Our identification of protein-level regulation by widespread transcript toggling through meiotic differentiation depended on our ability to observe a poor or negative correlation between mRNA and protein over time (Cheng et al. 2018). We compared measurements from ten samples, giving us a high degree of confidence in our correlation values. It is impossible to make such determinations with a sample from a single condition. Comparing expression trends over time also overcomes bias in different measurement methods that may result in misinterpretation of data from a single timepoint. For example, a protein may have lower measured levels than expected relative to its mRNA levels, either due to post-transcriptional regulation or difficulties in extraction or detection due to specific properties of the protein. It may be difficult to distinguish between these possibilities with single-sample comparison, but following mRNA and protein trends over many samples might be informative in defining the regulation for this gene, independent of any protein-specific measurement biases.

Moreover, regulatory mechanisms can be employed with precise timing that may be obscured in experiments in which only start- and end-points are measured. This is illustrated by an elegant study from Giraldez and colleagues (Bazzini et al. 2012), who measured the effects of the microRNA miR-430 on target translation and degradation. Prior to this study, it was unclear whether miRNA-mediated gene repression during vertebrate embryogenesis was primarily due to translational repression or mRNA degradation [reviewed in Djuranovic et al. (2011), Fabian et al. (2010)]. The authors performed RNA-seq and ribosome profiling at 2, 4, and 6 h post-fertilization (hpf) in zebrafish embryos. Strikingly, they found that miR-430 targets showed reduced translation at 4 hpf despite constant mRNA levels. By 6 hpf, both mRNA abundance and translation were reduced. The authors concluded that miR-430 first acts to prevent the translation of its targets before directing them for degradation. In this case, parallel, time-resolved, and genome-wide measurements were essential to determining causality that would have been masked by more distantly spaced timepoints. The authors were also aided by their choice of model system, which enabled study of miRNA-mediated repression in a natural context, rather than relying on mis-expression experiments, which might not always simulate physiological states.

5.6 Observing natural dynamic processes unmasks diverse regulatory mechanisms

Developmental processes, including cell differentiation and embryogenesis, allow researchers to study gene regulatory mechanisms in the context in which they evolved. In contrast, commonly studied lab conditions tend to be unnaturally rich or harsh, which may be valuable in revealing strong regulation, but may not accurately represent any real physiological state. Meiosis and other developmental processes involve sequential unidirectional cell state changes, often driven by “waves” of gene regulatory changes (Chu et al. 1998; Jin and Neiman 2016). We leveraged this feature of meiotic differentiation to reveal distinct modules of temporal gene expression control.

Another valuable developmental program for the study of gene regulation is oogenesis, in which eggs mature in the absence of new transcription and thus rely heavily on posttranscriptional regulatory mechanisms [reviewed in Johnstone and Lasko (2001), Tadros and Lipshitz (2009), Vardy and Orr-Weaver (2007)]. Using RNA-seq and ribosome profiling, Orr-Weaver, Bartel, and colleagues (Kronja et al. 2014) identified broad changes in translational regulation during the transition from mature oocyte to activated egg in Drosophila. To further assess the mechanisms underlying this translational regulation, the same groups coupled poly(A) tail length profiling to parallel ribosome profiling and RNA-seq and found a strong correlation between poly(A) tail length and TE during oogenesis (Eichhorn et al. 2016). This correlation persisted into the first few embryonic cell divisions, but disappeared during gastrulation, suggesting that the use of this mechanism is confined to a precise time in development.

A recent study described gene regulatory processes over a timecourse of induced neuronal development using RNA-seq, ribosome profiling, and polysome profiling (to measure differential translation of intact transcript isoforms) (Blair et al. 2017). The authors found some regulatory features that were employed only at certain stages of development. For example, long 3′ UTRs strongly repressed translation in differentiated neurons but had no effect in embryonic stem cells. Neuronally repressed transcripts were associated with the addition of putative structured elements and brain-specific miRNA binding sites in extended 3′ UTRs. While the developmental context and specific mechanisms differ, this finding is similar in concept to the LUTI-based mechanism in that transcripts with identical coding regions are differentially translated based on the inclusion or omission of cis-regulatory sequences (Chen et al. 2017; Cheng et al. 2018; Chia et al. 2017; Tresenrider and Ünal 2017).

These examples highlight an interesting feature of developmental gene regulation—different developmental processes may rely on different mechanisms to execute gene regulatory programs. Why is poly(A) length so important during oogenesis? Why do neurons encode extensive regulatory information in their 3′ UTRs when stem cells do not? Why are LUTI mRNAs abundant in meiotic differentiation? These questions emphasize the importance of studying diverse developmental processes if we are to uncover the full repertoire of gene regulatory strategies employed across biological systems.

5.7 Conclusions

Here we argue for the value of gene regulatory studies that (1) measure expression globally, (2) compare multiple outputs measured in parallel, (3) span several timepoints, and (4) explore natural developmental processes. These four features are often interconnected—for example, it is possible to take many informative timepoints during developmental processes because they are inherently dynamic, comprised of a progressive series of cell state changes. We were guided in our study by a model from one well-defined instance of LUTI-based regulation. However, with the current computational power available, a pre-existing model may not be necessary for the future identification of common non-canonical regulatory mechanisms. Instead, such discoveries may simply involve an integrated and unbiased analysis of parallel features detected and measured in a single, well-constructed dataset.

Our understanding of molecular biology is built on hypothesis-driven research. Hypotheses provide a framework for experimental design and data interpretation. The growing use of genome-scale datasets for measurement of gene expression, however, has shifted the rules for designing informative experiments. Parallel global gene expression measurements produce massive datasets that can be analyzed productively without the need for a specific hypothesis. This is analogous to the type of experiments done following the development of the microscope, when simple observation of life led scientists to base future research directions on unusual features that they came across and wished to understand better. Then and now, technological advances allowed visualization of much more information than could be thoroughly analyzed by hypothesis-based approaches alone—an experiment could simply serve to generate questions that one did not previously know to ask. Our current age of genomic measurements offers the opportunity for us to develop new models based on what we observe, rather than requiring us to fit our data to existing models. While certainly not the first, our study, identifying widespread use of an unconventional mode of gene regulation during natural cellular development, provides a strong argument for seeking out apparent anomalies in large-scale datasets. These cases may not actually represent exceptions, and may instead reflect gaps in prior canonical models, which were necessarily built from analysis of a few examples rather than distilled from integrated genome-wide analyses.

References

Aanes, H., Østrup, O., Andersen, I.S., Moen, L.F., Mathavan, S., Collas, P., and Alestrom, P. (2013). Differential transcript isoform usage pre- and post-zygotic genome activation in zebrafish. BMC Genomics 14, 331.

Aguilaniu, H., Gustafsson, L., Rigoulet, M., and Nyström, T. (2003). Asymmetric inheritance of oxidatively damaged proteins during cytokinesis. Science .

AhYoung, A.P., Jiang, J., Zhang, J., Dang, X.K., Loo, J.A., Zhou, Z.H., and Egea, P.F. (2015). Conserved SMP domains of the ERMES complex bind phospholipids and mediate tether assembly. Proc. Natl. Acad. Sci. U. S. A. *112*, E3179–E3188.

Ali, M.M.U., Bagratuni, T., Davenport, E.L., Nowak, P.R., Silva-Santisteban, M.C., Hardcastle, A., McAndrews, C., Rowlands, M.G., Morgan, G.J., Aherne, W., et al. (2011). Structure of the Ire1 autophosphorylation complex and implications for the unfolded protein response. EMBO J.

An, H., Ordureau, A., Paulo, J.A., Shoemaker, C.J., Denic, V., and Harper, J.W. (2019). TEX264 Is an Endoplasmic Reticulum-Resident ATG8-Interacting Protein Critical for ER Remodeling during Nutrient Stress. Mol. Cell.

Anding, A.L., and Baehrecke, E.H. (2017). Cleaning House: Selective Autophagy of Organelles. Dev. Cell.

van Anken, E., Pincus, D., Coyle, S., Aragón, T., Osman, C., Lari, F., Gómez Puerta, S., Korennykh, A. V., and Walter, P. (2014). Specificity in endoplasmic reticulum-stress signaling in yeast entails a step-wise engagement of HAC1 mRNA to clusters of the stress sensor Ire1. Elife.

Van Anken, E., Romijn, E.P., Maggioni, C., Mezghrani, A., Sitia, R., Braakman, I., and Heck, A.J.R. (2003). Sequential waves of functionally related proteins are expressed when B cells prepare for antibody secretion. Immunity.

Anwar, K., Klemm, R.W., Condon, A., Severin, K.N., Zhang, M., Ghirlando, R., Hu, J., Rapoport, T.A., and Prinz, W.A. (2012). The dynamin-like GTPase Sey1p mediates homotypic ER fusion in S. cerevisiae. J. Cell Biol. *197*, 209–217.

Aragón, T., Van Anken, E., Pincus, D., Serafimova, I.M., Korennykh, A. V., Rubio, C.A., and Walter, P. (2009). Messenger RNA targeting to endoplasmic reticulum stress signalling sites. Nature.

Audhya, A., Desai, A., and Oegema, K. (2007). A role for Rab5 in structuring the endoplasmic reticulum. J. Cell Biol.

Aviram, N., and Schuldiner, M. (2017). Targeting and translocation of proteins to the endoplasmic reticulum at a glance. J. Cell Sci. *130*, 4079–4085.

Aviram, N., Ast, T., Costa, E.A., Arakel, E.C., Chuartzman, S.G., Jan, C.H., Haßdenteufel, S., Dudek, J., Jung, M., Schorr, S., et al. (2016). The SND proteins constitute an alternative targeting route to the endoplasmic reticulum. Nature.

Babour, A., Bicknell, A.A., Tourtellotte, J., and Niwa, M. (2010). A Surveillance Pathway Monitors the Fitness of the Endoplasmic Reticulum to Control Its Inheritance. Cell.

Baldi, S., Bolognesi, A., Meinema, A.C., and Barral, Y. (2017). Heat stress promotes longevity in budding yeast by relaxing the confinement of age-promoting factors in the mother cell. Elife.

Benjamin, K.R., Zhang, C., Shokat, K.M., and Herskowitz, I. (2003). Control of landmark events in meiosis by the CDK Cdc28 and the meiosis-specific kinase Ime2. Genes Dev.

Berchowitz, L.E., Gajadhar, A.S., Werven, F.J. Van, Rosa, A. a De, Weissman, J.S., White, F.M., Amon, A., van Werven, F.J., De Rosa, A.A., Samoylova, M.L., et al. (2013). A developmentally regulated translational control pathway establishes the meiotic chromosome segregation pattern. Genes Dev. 2147–2163.

Berchowitz, L.E., Kabachinski, G., Walker, M.R., Carlile, T.M., Gilbert, W. V., Schwartz, T.U., and Amon, A. (2015). Regulated Formation of an Amyloid-like Translational Repressor Governs Gametogenesis. Cell *163*, 406–418.

Bhaskara, R.M., Grumati, P., Garcia-Pardo, J., Kalayil, S., Covarrubias-Pinto, A., Chen, W., Kudryashev, M., Dikic, I., and Hummer, G. (2019). Curvature induction and membrane remodeling by FAM134B reticulon homology domain assist selective ER-phagy. Nat. Commun.

Bian, X., Klemm, R.W., Liu, T.Y., Zhang, M., Sun, S., Sui, X., Liu, X., Rapoport, T.A., and Hu, J. (2011). Structures of the atlastin GTPase provide insight into homotypic fusion of endoplasmic reticulum membranes. Proc. Natl. Acad. Sci. U. S. A. *108*, 3976–3981.

Bircham, P., Papagiannidis, D., Lüchtenborg, C., Ruffini, G., Brügger, B., and Schuck, S. (2020). Control of endoplasmic reticulum membrane biogenesis by regulators of lipid metabolism. BioRxiv 2020.02.23.961722.

Bodnar, N.O., and Rapoport, T.A. (2017). Molecular Mechanism of Substrate Processing by the Cdc48 ATPase Complex. Cell.

Branon, T.C., Bosch, J.A., Sanchez, A.D., Udeshi, N.D., Svinkina, T., Carr, S.A., Feldman, J.L., Perrimon, N., and Ting, A.Y. (2018). Efficient proximity labeling in living cells and organisms with TurboID. Nat. Biotechnol.

Brar, G. a., Yassour, M., Friedman, N., Regev, A., Ingolia, N.T., Weissman, J.S., a. Brar, G., Yassour, M., Friedman, N., Regev, A., et al. (2012). High-Resolution View of the Yeast Meiotic Program Revealed by Ribosome Profiling. Science . *335*, 552–557.

Byrnes, L.J., and Sondermann, H. (2011). Structural basis for the nucleotide-dependent dimerization of the large G protein atlastin-1/SPG3A. Proc. Natl. Acad. Sci. U. S. A. *108*, 2216–2221.

Byrnes, L.J., Singh, A., Szeto, K., Benvin, N.M., O'Donnell, J.P., Zipfel, W.R., and Sondermann, H. (2013). Structural basis for conformational switching and GTP loading of the large G protein atlastin. EMBO J.

Carlile, T.M., and Amon, A. (2008). Meiosis I Is Established through Division-Specific Translational Control of a Cyclin. Cell *133*, 280–291.

Casey, A.K., Chen, S., Novick, P., Ferro-Novick, S., and Wente, S.R. (2015). Nuclear pore complex integrity requires Lnp1, a regulator of cortical endoplasmic reticulum. Mol. Biol. Cell *26*, 2833–2844.

Chadwick, S.R., Fazio, E.N., Etedali-Zadeh, P., Genereaux, J., Duennwald, M.L., and Lajoie, P. (2020). A functional unfolded protein response is required for chronological aging in Saccharomyces cerevisiae. Curr. Genet.

Chang, B.J., Meza, V.D.P., and Stelzer, E.H.K. (2017). csiLSFM combines light-sheet fluorescence microscopy and coherent Structured illumination for a lateral resolution below 100 nm. Proc. Natl. Acad. Sci. U. S. A.

Chao, J.T., Wong, A.K.O., Tavassoli, S., Young, B.P., Chruscicki, A., Fang, N.N., Howe, L.J., Mayor, T., Foster, L.J., and Loewen, C.J.R. (2014). Polarization of the endoplasmic reticulum by ER-septin tethering. Cell *158*, 620–632.

Chen, J., Tresenrider, A., Chia, M., McSwiggen, D.T., Spedale, G., Jorgensen, V., Liao, H., Van Werven, F.J., and Ünal, E. (2017). Kinetochore inactivation by expression of a repressive mRNA. Elife.

Chen, Q., Xiao, Y., Chai, P., Zheng, P., Teng, J., and Chen, J. (2019). ATL3 Is a Tubular ER-Phagy Receptor for GABARAP-Mediated Selective Autophagy. Curr. Biol.

Chen, S., Novick, P., and Ferro-Novick, S. (2012). ER network formation requires a balance of the dynamin-like GTPase Sey1p and the Lunapark family member Lnp1p. Nat. Cell Biol. *14*, 707–716.

Chen, S., Desai, T., McNew, J.A., Gerard, P., Novick, P.J., and Ferro-Novick, S. (2015). Lunapark stabilizes nascent three-way junctions in the endoplasmic reticulum. Proc. Natl. Acad. Sci. U. S. A.

Chen, S., Cui, Y., Parashar, S., Novick, P.J., and Ferro-Novick, S. (2018). ER-phagy requires Lnp1, a protein that stabilizes rearrangements of the ER network. Proc. Natl. Acad. Sci. U. S. A.

Cheng, Z., Otto, G.M., Powers, E.N., Keskin, A., Mertins, P., Carr, S.A., Jovanovic, M., and Brar, G.A. (2018). Pervasive, Coordinated Protein-Level Changes Driven by Transcript Isoform Switching during Meiosis. Cell *172*.

Chia, M., Tresenrider, A., Chen, J., Spedale, G., Jorgensen, V., Ünal, E., and van Werven, F.J. (2017). Transcription of a 5' extended mRNA isoform directs dynamic chromatin changes and interference of a downstream promoter. Elife.

Chino, H., and Mizushima, N. (2020). ER-Phagy: Quality Control and Turnover of Endoplasmic Reticulum. Trends Cell Biol.

Chino, H., Hatta, T., Natsume, T., and Mizushima, N. (2019). Intrinsically Disordered Protein TEX264 Mediates ER-phagy. Mol. Cell.

Cho, K.F., Branon, T.C., Udeshi, N.D., Myers, S.A., Carr, S.A., and Ting, A.Y. (2020). Proximity labeling in mammalian cells with TurboID and split-TurboID. Nat. Protoc.

Chu, S., and Herskowitz, I. (1998). Gametogenesis in yeast is regulated by a transcriptional cascade dependent on Ndt80. Mol. Cell.

Clay, L., Caudron, F., Denoth-Lippuner, A., Boettcher, B., Frei, S.B., Snapp, E.L., and Barral, Y. (2014). A sphingolipid-dependent diffusion barrier confines ER stress to the yeast mother cell. Elife.

Collado, J., Kalemanov, M., Campelo, F., Bourgoint, C., Thomas, F., Loewith, R., Martínez-Sánchez, A., Baumeister, W., Stefan, C.J., and Fernández-Busnadiego, R. (2019). Tricalbin-Mediated Contact Sites Control ER Curvature to Maintain Plasma Membrane Integrity. Dev. Cell *51*, 476-487.e7.

COPELAND, D.E., and DALTON, A.J. (1959). An association between mitochondria and the endoplasmic reticulum in cells of the pseudobranch gland of a teleost. J. Biophys. Biochem. Cytol. *5*, 393–396.

Cox, J.S., and Walter, P. (1996). A novel mechanism for regulating activity of a transcription factor that controls the unfolded protein response. Cell.

Creutz, C.E., Snyder, S.L., and Schulz, T.A. (2004). Characterization of the yeast tricalbins: Membrane-bound multi-C2-domain proteins that form complexes involved in membrane trafficking. Cell. Mol. Life Sci.

Cui, Y., Parashar, S., Zahoor, M., Needham, P.G., Mari, M., Zhu, M., Chen, S., Ho, H.C., Reggiori, F., Farhan, H., et al. (2019). A COPII subunit acts with an autophagy receptor to target endoplasmic reticulum for degradation. Science .

Cunningham, C.N., Williams, J.M., Knupp, J., Arunagiri, A., Arvan, P., and Tsai, B. (2019). Cells Deploy a Two-Pronged Strategy to Rectify Misfolded Proinsulin Aggregates. Mol. Cell.

Van Dalfsen, K.M., Hodapp, S., Keskin, A., Otto, G.M., Berdan, C.A., Higdon, A., Cheunkarndee, T., Nomura, D.K., Jovanovic, M., and Brar, G.A. (2018). Global Proteome Remodeling during ER Stress Involves Hac1-Driven Expression of Long Undecoded Transcript Isoforms. Dev. Cell.

Davidowitz, J., Philips, G.H., Pachter, B.R., and Breinin, G.M. (1975). Particle free and glycogen bearing double membrane arrays in extraocular muscle of rabbit. Am. J. Pathol. *78*, 191–198.

Denic, V., Quan, E.M., and Weissman, J.S. (2006). A Luminal Surveillance Complex that Selects Misfolded Glycoproteins for ER-Associated Degradation. Cell.

Du, Y., Pypaert, M., Novick, P., and Ferro-Novick, S. (2001). Aux1p/Swa2p Is Required for Cortical Endoplasmic Reticulum Inheritance in *Saccharomyces cerevisiae*. Mol. Biol. Cell *12*, 2614–2628.

Eastwood, M.D., Cheung, S.W.T., Lee, K.Y., Moffat, J., and Meneghini, M.D. (2012). Developmentally Programmed Nuclear Destruction during Yeast Gametogenesis. Dev. Cell.
Eisenberg, A.R., Higdon, A., Keskin, A., Hodapp, S., Jovanovic, M., and Brar, G.A. (2018). Precise Post-translational Tuning Occurs for Most Protein Complex Components during Meiosis. Cell Rep.

Espadas, J., Pendin, D., Bocanegra, R., Escalada, A., Misticoni, G., Trevisan, T., Velasco del Olmo, A., Montagna, A., Bova, S., Ibarra, B., et al. (2019). Dynamic constriction and fission of endoplasmic reticulum membranes by reticulon. Nat. Commun.

Estrada, P., Kim, J., Coleman, J., Walker, L., Dunn, B., Takizawa, P., Novick, P., and Ferro-Novick, S. (2003). Myo4p and She3p are required for cortical ER inheritance in Saccharomyces cerevisiae. J. Cell Biol. *163*, 1255–1266.

Fehrenbacher, K.L., Davis, D., Wu, M., Boldogh, I., and Pon, L.A. (2002). Endoplasmic reticulum dynamics, inheritance, and cytoskeletal interactions in budding yeast. Mol. Biol. Cell *13*, 854–865.

Forrester, A., De Leonibus, C., Grumati, P., Fasana, E., Piemontese, M., Staiano, L., Fregno, I., Raimondi, A., Marazza, A., Bruno, G., et al. (2019). A selective ER -phagy exerts procollagen quality control via a Calnexin- FAM 134B complex . EMBO J.

Friedman, J.R., Lackner, L.L., West, M., DiBenedetto, J.R., Nunnari, J., and Voeltz, G.K. (2011). ER tubules mark sites of mitochondrial division. Science *334*, 358–362.

Fumagalli, F., Noack, J., Bergmann, T.J., Presmanes, E.C., Pisoni, G.B., Fasana, E., Fregno, I., Galli, C., Loi, M., Soldà, T., et al. (2016). Translocon component Sec62 acts in endoplasmic reticulum turnover during stress recovery. Nat. Cell Biol. *18*, 1173–1184.

Gauss, R., Jarosch, E., Sommer, T., and Hirsch, C. (2006). A complex of Yos9p and the HRD ligase integrates endoplasmic reticulum quality control into the degradation machinery. Nat. Cell Biol.
Gibson, D.G., Young, L., Chuang, R.Y., Venter, J.C., Hutchison, C.A., and Smith, H.O. (2009). Enzymatic assembly of DNA molecules up to several hundred kilobases. Nat. Methods.

Gilmore, R., Walter, P., and Blobel, G. (1982a). Protein translocation across the endoplasmic reticulum. II. Isolation and characterization of the signal recognition particle receptor. J. Cell Biol.

Gilmore, R., Blobel, G., and Walter, P. (1982b). Protein translocation across the endoplasmic reticulum. I. Detection in the microsomal membrane of a receptor for the signal recognition particle. J. Cell Biol.

Giordano, F., Saheki, Y., Idevall-Hagren, O., Colombo, S.F., Pirruccello, M., Milosevic, I., Gracheva, E.O., Bagriantsev, S.N., Borgese, N., and De Camilli, P. (2013). XPI(4,5)P2-Dependent and Ca2+-Regulated ER-PM interactions mediated by the extended synaptotagmins. Cell.

Gogala, M., Becker, T., Beatrix, B., Armache, J.P., Barrio-Garcia, C., Berninghausen, O., and Beckmann, R. (2014). Structures of the Sec61 complex engaged in nascent peptide translocation or membrane insertion. Nature *506*, 107–110.

Goodman, J.S., King, G.A., and Ünal, E. (2020). Cellular quality control during gametogenesis. Exp. Cell Res.

Graef, M., Friedman, J.R., Graham, C., Babu, M., and Nunnari, J. (2013). ER exit sites are physical and functional core autophagosome biogenesis components. Mol. Biol. Cell.

Grumati, P., Morozzi, G., Hölper, S., Mari, M., Harwardt, M.L.I.E., Yan, R., Müller, S., Reggiori, F., Heilemann, M., and Dikic, I. (2017). Full length RTN3 regulates turnover of tubular endoplasmic reticulum via selective autophagy. Elife.

Guo, Y., Li, D.D., Zhang, S., Yang, Y., Liu, J.J., Wang, X., Liu, C., Milkie, D.E., Moore, R.P., Tulu, U.S., et al. (2018). Visualizing Intracellular Organelle and Cytoskeletal Interactions at Nanoscale Resolution on Millisecond Timescales. Cell *175*, 1430-1442.e17.

Halbleib, K., Pesek, K., Covino, R., Hofbauer, H.F., Wunnicke, D., Hänelt, I., Hummer, G., and Ernst, R. (2017). Activation of the Unfolded Protein Response by Lipid Bilayer Stress. Mol. Cell.

Ho, N., Yap, W.S., Xu, J., Wu, H., Koh, J.H., Goh, W.W. Bin, George, B., Chong, S.C., Taubert, S., and Thibault, G. (2020). Stress sensor Ire1 deploys a divergent transcriptional program in response to lipid bilayer stress. J. Cell Biol.

Hoffmann, P.C., Bharat, T.A.M.M., Wozny, M.R., Boulanger, J., Miller, E.A., and Kukulski, W. (2019). Tricalbins Contribute to Cellular Lipid Flux and Form Curved ER-PM Contacts that Are Bridged by Rod-Shaped Structures. Dev. Cell *51*, 488-502.e8.

Hu, C.C.A., Dougan, S.K., McGehee, A.M., Love, J.C., and Ploegh, H.L. (2009a). XBP-1 regulates signal transduction, transcription factors and bone marrow colonization in B cells. EMBO J.

Hu, J., Shibata, Y., Voss, C., Shemesh, T., Li, Z., Coughlin, M., Kozlov, M.M., Rapoport, T.A., and Prinz, W.A. (2008). Membrane proteins of the endoplasmic reticulum induce high-curvature tubules. Science .

Hu, J., Shibata, Y., Zhu, P.P., Voss, C., Rismanchi, N., Prinz, W.A., Rapoport, T.A., and Blackstone, C. (2009b). A Class of Dynamin-like GTPases Involved in the Generation of the Tubular ER Network. Cell *138*, 549–561.

Hu, X., Shi, Q., Zhou, X., He, W., Yi, H., Yin, X., Gearing, M., Levey, A., and Yan, R. (2007). Transgenic mice overexpressing reticulon 3 develop neuritic abnormalities. EMBO J.

Jamieson, J.D., and Palade, G.E. (1967a). Intracellular transport of secretory proteins in the pancreatic exocrine cell. II. Transport to condensing vacuoles and zymogen granules. J. Cell Biol.

Jamieson, J.D., and Palade, G.E. (1967b). Intracellular transport of secretory proteins in the pancreatic exocrine cell. I. Role of the peripheral elements of the Golgi complex. J. Cell Biol. *34*, 577–596.

Janke, C., Magiera, M.M., Rathfelder, N., Taxis, C., Reber, S., Maekawa, H., Moreno-Borchart, A., Doenges, G., Schwob, E., Schiebel, E., et al. (2004). A versatile toolbox for PCR-based tagging of yeast genes: New fluorescent proteins, more markers and promoter substitution cassettes. Yeast.

Jeong, H., Park, J., Jun, Y., and Lee, C. (2017). Crystal structures of Mmm1 and Mdm12–Mmm1 reveal mechanistic insight into phospholipid trafficking at ER-mitochondria contact sites. Proc. Natl. Acad. Sci. U. S. A. *114*, E9502–E9511.

Jiang, X., Wang, X., Ding, X., Du, M., Li, B., Weng, X., Zhang, J., Li, L., Tian, R., Zhu, Q., et al. (2020). FAM 134B oligomerization drives endoplasmic reticulum membrane scission for ER - phagy . EMBO J. *39*.

Kamber, R.A., Shoemaker, C.J., and Denic, V. (2015). Receptor-Bound Targets of Selective Autophagy Use a Scaffold Protein to Activate the Atg1 Kinase. Mol. Cell.

Keenan, R.J., Freymann, D.M., Walter, P., and Stroud, R.M. (1998). Crystal structure of the signal sequence binding subunit of the signal recognition particle. Cell *94*, 181–191.

Khaminets, A., Heinrich, T., Mari, M., Grumati, P., Huebner, A.K., Akutsu, M., Liebmann, L., Stolz, A., Nietzsche, S., Koch, N., et al. (2015). Regulation of endoplasmic reticulum turnover by selective autophagy. Nature.

King, G.A., Goodman, J.S., Schick, J.G., Chetlapalli, K., Jorgens, D.M., McDonald, K.L., and Ünal, E. (2019). Meiotic cellular rejuvenation is coupled to nuclear remodeling in budding yeast. Elife.

Klopfenstein, D.R., Klumperman, J., Lustig, A., Kammerer, R.A., Oorschot, V., and Hauri, H.P. (2001). Subdomain-specific localization of CLIMP-63 (p63) in the endoplasmic reticulum is mediated by its luminal α-helical segment. J. Cell Biol. *153*, 1287–1299.

Korennykh, A. V., Egea, P.F., Korostelev, A.A., Finer-Moore, J., Zhang, C., Shokat, K.M., Stroud, R.M., and Walter, P. (2009). The unfolded protein response signals through high-order assembly of Ire1. Nature.

Kornmann, B., Currie, E., Collins, S.R., Schuldiner, M., Nunnari, J., Weissman, J.S., and Walter, P. (2009). An ER-mitochondria tethering complex revealed by a synthetic biology screen. Science . *325*, 477–481.

Kornmann, B., Osman, C., and Walter, P. (2011). The conserved GTPase Gem1 regulates endoplasmic reticulum-mitochondria connections. Proc. Natl. Acad. Sci. U. S. A. *108*, 14151–14156.

Lee, B.H., and Amon, A. (2003). Role of Polo-like kinase CDC5 in programming meiosis I chromosome segregation. Science .

Lee, K.P.K., Dey, M., Neculai, D., Cao, C., Dever, T.E., and Sicheri, F. (2008). Structure of the Dual Enzyme Ire1 Reveals the Basis for Catalysis and Regulation in Nonconventional RNA Splicing. Cell.

Lewis, S.C., Uchiyama, L.F., and Nunnari, J. (2016). ER-mitochondria contacts couple mtDNA synthesis with Mitochondrial division in human cells. Science .

Li, X., Du, Y., Siegel, S., Ferro-Novick, S., and Novick, P. (2010). Activation of the mitogen-activated protein kinase, Slt2p, at bud tips blocks a late stage of endoplasmic reticulum inheritance in Saccharomyces cerevisiae. Mol. Biol. Cell *21*, 1772–1782.

Li, X., Ferro-Novick, S., and Novick, P. (2013). Different polarisome components play distinct roles in Slt2p-regulated cortical ER inheritance in Saccharomyces cerevisiae. Mol. Biol. Cell *24*, 3145–3154.

Loewen, C.J.R., Young, B.P., Tavassoli, S., and Levine, T.P. (2007). Inheritance of cortical ER in yeast is required for normal septin organization. J. Cell Biol. *179*, 467–483.

Loi, M., Raimondi, A., Morone, D., and Molinari, M. (2019). ESCRT-III-driven piecemeal micro-ER-phagy remodels the ER during recovery from ER stress. Nat. Commun.

Longtine, M.S., McKenzie, A., Demarini, D.J., Shah, N.G., Wach, A., Brachat, A., Philippsen, P., and Pringle, J.R. (1998). Additional modules for versatile and economical PCR-based gene deletion and modification in Saccharomyces cerevisiae. Yeast.

Luedeke, C., Frei, S.B., Sbalzarini, I., Schwarz, H., Spang, A., and Barral, Y. (2005). Septin-dependent compartmentalization of the endoplasmic reticulum during yeast polarized growth. J. Cell Biol. *169*, 897–908.

Maco, B., Holtmaat, A., Cantoni, M., Kreshuk, A., Straehle, C.N., Hamprecht, F.A., and Knott, G.W. (2013). Correlative In Vivo 2 Photon and Focused Ion Beam Scanning Electron Microscopy of Cortical Neurons. PLoS One *8*, e57405.

Manford, A.G., Stefan, C.J., Yuan, H.L., MacGurn, J.A., and Emr, S.D. (2012). ER-to-Plasma Membrane Tethering Proteins Regulate Cell Signaling and ER Morphology. Dev. Cell *23*.

Marston, A.L., and Amon, A. (2004). Meiosis: cell-cycle controls shuffle and deal. Nat. Rev. Mol. Cell Biol. *5*, 983–997.

Mateja, A., and Keenan, R.J. (2018). A structural perspective on tail-anchored protein biogenesis by the GET pathway. Curr. Opin. Struct. Biol.

Mateja, A., Paduch, M., Chang, H.Y., Szydlowska, A., Kossiakoff, A.A., Hegde, R.S., and Keenan, R.J. (2015). Structure of the Get3 targeting factor in complex with its membrane protein cargo. Science . *347*, 1152–1155.

Matos, J., Lipp, J.J., Bogdanova, A., Guillot, S., Okaz, E., Junqueira, M., Shevchenko, A., and Zachariae, W. (2008). Dbf4-Dependent Cdc7 Kinase Links DNA Replication to the Segregation of Homologous Chromosomes in Meiosis I. Cell.

McDowell, M.A., Heimes, M., Fiorentino, F., Mehmood, S., Farkas, Á., Coy-Vergara, J., Wu, D., Bolla, J.R., Schmid, V., Heinze, R., et al. (2020). Structural Basis of Tail-Anchored Membrane Protein Biogenesis by the GET Insertase Complex. Mol. Cell.

Mizuno, T., Muroi, K., and Irie, K. (2020). Snf1 AMPK positively regulates ER-phagy via expression control of Atg39 autophagy receptor in yeast ER stress response. PLoS Genet.

Mochida, K., Oikawa, Y., Kimura, Y., Kirisako, H., Hirano, H., Ohsumi, Y., and Nakatogawa, H.

(2015). Receptor-mediated selective autophagy degrades the endoplasmic reticulum and the nucleus. Nature.

Mochida, K., Yamasaki, A., Matoba, K., Kirisako, H., Noda, N.N., and Nakatogawa, H. (2020). Super-assembly of ER-phagy receptor Atg40 induces local ER remodeling at contacts with forming autophagosomal membranes. Nat. Commun.

Moreno-Borchart, A.C., and Knop, M. (2003). Prospore membrane formation: How budding yeast gets shaped in meiosis. Microbiol. Res.

Morishita, H., and Mizushima, N. (2019). Diverse cellular roles of autophagy. Annu. Rev. Cell Dev. Biol.

Moss, T.J., Andreazza, C., Verma, A., Daga, A., and McNew, J.A. (2011). Membrane fusion by the GTPase atlastin requires a conserved C-terminal cytoplasmic tail and dimerization through the middle domain. Proc. Natl. Acad. Sci. U. S. A. *108*, 11133–11138.

Murley, A., Lackner, L.L., Osman, C., West, M., Voeltz, G.K., Walter, P., and Nunnari, J. (2013). ER-associated mitochondrial division links the distribution of mitochondria and mitochondrial DNA in yeast. Elife *2013*, 1–16.

Nakanishi, H., De Los Santos, P., and Neiman, A.M. (2004). Positive and Negative Regulation of a SNARE Protein by Control of Intracellular Localization. Mol. Biol. Cell.

Neal, S., Jaeger, P.A., Duttke, S.H., Benner, C.K., Glass, C., Ideker, T., and Hampton, R. (2018). The Dfm1 Derlin Is Required for ERAD Retrotranslocation of Integral Membrane Proteins. Mol. Cell.

Neiman, A.M. (2011). Sporulation in the budding yeast Saccharomyces cerevisiae. Genetics *189*, 737–765.

Neller, J., Dünkler, A., Rösler, R., and Johnsson, N. (2015). A protein complex containing Epo1p anchors the cortical endoplasmic reticulum to the yeast bud tip. J. Cell Biol. *208*, 71–87.

Nishimura, K., Fukagawa, T., Takisawa, H., Kakimoto, T., and Kanemaki, M. (2009). An auxin-based degron system for the rapid depletion of proteins in nonplant cells. Nat. Methods.

Nixon-Abell, J., Obara, C.J., Weigel, A. V., Li, D., Legant, W.R., Xu, C.S., Pasolli, H.A., Harvey, K., Hess, H.F., Betzig, E., et al. (2016). Increased spatiotemporal resolution reveals highly dynamic dense tubular matrices in the peripheral ER. Science . *354*.

Ogata, T., and Yamasaki, Y. (1997). Ultra-high-resolution scanning electron microscopy of mitochondria and sarcoplasmic reticulum arrangement in human red, white, and intermediate muscle fibers. Anat. Rec.

Okada, M., Kusunoki, S., Ishibashi, Y., and Kito, K. (2017). Proteomics analysis for asymmetric inheritance of preexisting proteins between mother and daughter cells in budding yeast. Genes to Cells.

Orso, G., Pendin, D., Liu, S., Tosetto, J., Moss, T.J., Faust, J.E., Micaroni, M., Egorova, A., Martinuzzi, A., a McNew, J., et al. (2009). Homotypic fusion of ER membranes requires the dynamin-like GTPase Atlastin. Nature *460*, 978–983.

Otto, G.M., and Brar, G.A. (2018). Seq-ing answers: uncovering the unexpected in global gene regulation. Curr. Genet.

Öztürk, Z., O’Kane, C.J., and Pérez-Moreno, J.J. (2020). Axonal Endoplasmic Reticulum Dynamics and Its Roles in Neurodegeneration. Front. Neurosci.

Parlakgül, G., Arruda, A.P., Cagampan, E., Pang, S., Güney, E., Lee, Y., Hess, H.F., Xu, S., and Hotamışlıgil, G.S. (2020). High resolution 3D imaging of liver reveals a central role for subcellular architectural organization in metabolism. BioRxiv.

Pendin, D., Tosetto, J., Moss, T.J., Andreazza, C., Moro, S., McNew, J.A., and Daga, A. (2011). GTP-dependent packing of a three-helix bundle is required for atlastin-mediated fusion. Proc. Natl. Acad. Sci. U. S. A. *108*, 16283–16288.

Petkovic, M., Jemaiel, A., Daste, F., Specht, C.G., Izeddin, I., Vorkel, D., Verbavatz, J.M., Darzacq, X., Triller, A., Pfenninger, K.H., et al. (2014). The SNARE Sec22b has a non-fusogenic function in plasma membrane expansion. Nat. Cell Biol.

Piña, F.J., and Niwa, M. (2015). The ER Stress Surveillance (ERSU) pathway regulates daughter cell ER protein aggregate inheritance. Elife.

Powers, R.E., Wang, S., Liu, T.Y., and Rapoport, T.A. (2017). Reconstitution of the tubular endoplasmic reticulum network with purified components. Nature.

Rapoport, T.A. (2007). Protein translocation across the eukaryotic endoplasmic reticulum and bacterial plasma membranes. Nature *450*, 663–669.

Renvoisé, B., and Blackstone, C. (2010). Emerging themes of ER organization in the development and maintenance of axons. Curr. Opin. Neurobiol. *20*, 531–537.

Rossanese, O.W., Reinke, C.A., Bevis, B.J., Hammond, A.T., Sears, I.B., O’Connor, J., and Glick, B.S. (2001). A role for actin, Cdc1p, and Myo2p in the inheritance of late Golgi elements in Saccharomyces cerevisiae. J. Cell Biol.

Rouskin, S., Zubradt, M., Washietl, S., Kellis, M., and Weissman, J.S. (2014). Genome-wide probing of RNA structure reveals active unfolding of mRNA structures in vivo. Nature.

Saheki, Y., Bian, X., Schauder, C.M., Sawaki, Y., Surma, M.A., Klose, C., Pincet, F., Reinisch, K.M., Camilli, P. De, and De Camilli, P. (2016). Control of plasma membrane lipid homeostasis by the extended synaptotagmins. Nat. Cell Biol. *18*, 504–515.

Sawyer, E.M., Joshi, P.R., Jorgensen, V., Yunus, J., Berchowitz, L.E., and Ünal, E. (2019). Developmental regulation of an organelle tether coordinates mitochondrial remodeling in meiosis. J. Cell Biol.

Schauder, C.M., Wu, X., Saheki, Y., Narayanaswamy, P., Torta, F., Wenk, M.R., Camilli, P. De, Reinisch, K.M., De Camilli, P., and Reinisch, K.M. (2014). Structure of a lipid-bound extended synaptotagmin indicates a role in lipid transfer. Nature *510*, 552–555.

Schmidt, C.C., Vasic, V., and Stein, A. (2020). Doa10 is a membrane protein retrotranslocase in er-associated protein degradation. Elife.

Schoebel, S., Mi, W., Stein, A., Ovchinnikov, S., Pavlovicz, R., DImaio, F., Baker, D., Chambers, M.G., Su, H., Li, D., et al. (2017). Cryo-EM structure of the protein-conducting ERAD channel Hrd1 in complex with Hrd3. Nature.

Schuck, S., Prinz, W.A., Thorn, K.S., Voss, C., and Walter, P. (2009). Membrane expansion alleviates endoplasmic reticulum stress independently of the unfolded protein response. J. Cell Biol. *187*, 525–536.

Schuck, S., Gallagher, C.M., and Walter, P. (2014). ER-phagy mediates selective degradation of endoplasmic reticulum independently of the core autophagy machinery. J. Cell Sci. *127*, 4078–4088.

Schuldiner, M., Metz, J., Schmid, V., Denic, V., Rakwalska, M., Schmitt, H.D., Schwappach, B., and Weissman, J.S. (2008). The GET Complex Mediates Insertion of Tail-Anchored Proteins into the ER Membrane. Cell.

Schwarz, D.S., and Blower, M.D. (2016). The endoplasmic reticulum: Structure, function and response to cellular signaling. Cell. Mol. Life Sci. *73*, 79–94.

Shcheprova, Z., Baldi, S., Frei, S.B., Gonnet, G., and Barral, Y. (2008). A mechanism for asymmetric segregation of age during yeast budding. Nature.

Shi, Q., Ge, Y., He, W., Hu, X., and Yan, R. (2017). RTN1 and RTN3 protein are differentially associated with senile plaques in Alzheimer’s brains. Sci. Rep.

Shibata, Y., Voeltz, G.K., and Rapoport, T.A. (2006). Rough Sheets and Smooth Tubules. Cell *126*, 435–439.

Shibata, Y., Voss, C., Rist, J.M., Hu, J., Rapoport, T.A., Prinz, W.A., and Voeltz, G.K. (2008). The reticulon and Dp1/Yop1p proteins form immobile oligomers in the tubular endoplasmic reticulum. J. Biol. Chem. *283*, 18892–18904.

Shibata, Y., Shemesh, T., Prinz, W.A., Palazzo, A.F., Kozlov, M.M., and Rapoport, T.A. (2010). Mechanisms determining the morphology of the peripheral ER. Cell *143*, 774–788.

Sparkes, I., Tolley, N., Aller, I., Svozil, J., Osterrieder, A., Botchway, S., Mueller, C., Frigerio, L., and Hawes, C. (2010). Five Arabidopsis reticulon isoforms share endoplasmic reticulum location, topology, and membrane-shaping properties. Plant Cell *22*, 1333–1343.

Suda, Y., Nakanishi, H., Mathieson, E.M., and Neiman, A.M. (2007). Alternative modes of organellar segregation during sporulation in Saccharomyces cerevisiae. Eukaryot. Cell *6*, 2009–2017.

Sugiyama, S., and Tanaka, M. (2019). Distinct segregation patterns of yeast cell-peripheral proteins uncovered by a method for protein segregatome analysis. Proc. Natl. Acad. Sci. U. S. A.

Takizawa, P.A., DeRisi, J.L., Wilhelm, J.E., and Vale, R.D. (2000). Plasma membrane compartmentalization in yeast by messenger RNA transport and a septin diffusion barrier. Science .

Terasaki, M., Shemesh, T., Kasthuri, N., Klemm, R.W., Schalek, R., Hayworth, K.J., Hand, A.R., Yankova, M., Huber, G., Lichtman, J.W., et al. (2013). XStacked endoplasmic reticulum sheets are connected by helicoidal membrane motifs. Cell.

Tolley, N., Sparkes, I.A., Hunter, P.R., Craddock, C.P., Nuttall, J., Roberts, L.M., Hawes, C., Pedrazzini, E., and Frigerio, L. (2008). Overexpression of a plant reticulon remodels the lumen of the cortical endoplasmic reticulum but does not perturb protein transport. Traffic.

Tolley, N., Sparkes, I., Craddock, C.P., Eastmond, P.J., Runions, J., Hawes, C., and Frigerio, L. (2010). Transmembrane domain length is responsible for the ability of a plant reticulon to shape endoplasmic reticulum tubules in vivo. Plant J.

Topolska, M., Roelants, F.M., Si, E.P., and Thorner, J. (2020). TORC2-Dependent Ypk1-Mediated Phosphorylation of Lam2/Ltc4 Disrupts Its Association with the β-Propeller Protein Laf1 at Endoplasmic Reticulum-Plasma Membrane Contact Sites in the Yeast Saccharomyces cerevisiae. Biomolecules.

Torggler, R., Papinski, D., and Kraft, C. (2017). Assays to Monitor Autophagy in Saccharomyces cerevisiae. Cells *6*, 23.

Travers, K.J., Patil, C.K., Wodicka, L., Lockhart, D.J., Weissman, J.S., and Walter, P. (2000).

Functional and genomic analyses reveal an essential coordination between the unfolded protein response and ER-associated degradation. Cell.

Ünal, E., Kinde, B., and Amon, A. (2011). Gametogenesis eliminates age-induced cellular damage and resets life span in yeast. Science .

Vance, J.E. (1990). Phospholipid synthesis in a membrane fraction associated with mitochondria. J. Biol. Chem.

Voeltz, G.K., Prinz, W.A., Shibata, Y., Rist, J.M., and Rapoport, T.A. (2006). A class of membrane proteins shaping the tubular endoplasmic reticulum. Cell *124*, 573–586.

Walter, P., and Ron, D. (2011). The unfolded protein response: From stress pathway to homeostatic regulation. Science .

Wang, S., Romano, F.B., Field, C.M., Mitchison, T.J., and Rapoport, T.A. (2013). Multiple mechanisms determine ER network morphology during the cell cycle in Xenopus egg extracts. J. Cell Biol.

Wang, S., Tukachinsky, H., Romano, F.B., and Rapoport, T.A. (2016). Cooperation of the ER-shaping proteins atlastin, lunapark, and reticulons to generate a tubular membrane network. Elife *5*.

West, M., Zurek, N., Hoenger, A., and Voeltz, G.K. (2011). A 3D analysis of yeast ER structure reveals how ER domains are organized by membrane curvature. J. Cell Biol. *193*, 333–346.

Westrate, L.M.M., Lee, J.E.E., Prinz, W.A.A., and Voeltz, G.K.K. (2015). Form Follows Function: The Importance of Endoplasmic Reticulum Shape. Annu. Rev. Biochem. *84*, 791–811.

Wiest, D.L., Burkhardt, J.K., Hester, S., Hortsch, M., Meyer, D.I., and Argon, Y. (1990). Membrane biogenesis during B cell differentiation: Most endoplasmic reticulum proteins are expressed coordinately. J. Cell Biol.

Wittebolle, L., Marzorati, M., Clement, L., Balloi, A., Daffonchio, D., Heylen, K., De Vos, P., Verstraete, W., and Boon, N. (2009). Initial community evenness favours functionality under selective stress. Nature.

Wu, X., and Rapoport, T.A. (2018). Mechanistic insights into ER-associated protein degradation. Curr. Opin. Cell Biol.

Xu, L., Ajimura, M., Padmore, R., Klein, C., and Kleckner, N. (1995). NDT80, a meiosis-specific gene required for exit from pachytene in Saccharomyces cerevisiae. Mol. Cell. Biol.

Yu, H., Liu, Y., Gulbranson, D.R., Paine, A., Rathore, S.S., and Shen, J. (2016). Extended synaptotagmins are Ca2+-dependent lipid transfer proteins at membrane contact sites. Proc. Natl. Acad. Sci. U. S. A. *113*, 4362–4367.

Zachs, T., Schertel, A., Medeiros, J., Weiss, G.L., Hugener, J., Matos, J., and Pilhofer, M. (2020). Fully automated, sequential focused ion beam milling for cryo-electron tomography. Elife.

Zhang, X., Ding, X., Marshall, R.S., Paez-Valencia, J., Lacey, P., Vierstra, R.D., and Otegui, M.S. (2020). Reticulon proteins modulate autophagy of the endoplasmic reticulum in maize endosperm. Elife.

Zhao, D., Zou, C.X., Liu, X.M., Jiang, Z. Di, Yu, Z.Q., Suo, F., Du, T.Y., Dong, M.Q., He, W., and Du, L.L. (2020). A UPR-Induced Soluble ER-Phagy Receptor Acts with VAPs to Confer ER Stress Resistance. Mol. Cell.

Zurek, N., Sparks, L., and Voeltz, G. (2011). Reticulon short hairpin transmembrane domains are used to shape ER tubules. Traffic *12*, 28–41.